PHOTOELECTRON SPECTROSCOPY STUDIES

ON NOVEL DOPED CLUSTERS

By

LEIMING WANG

A dissertation submitted in partial fulfillment of
the requirements for the degree of

DOCTOR OF PHILOSOPHY

WASHINGTON STATE UNIVERSITY
Department of Physics and Astronomy

DECEMBER 2009

To the Faculty of Washington State University:

The members of the Committee appointed to examine the dissertation of LEIMING WANG find it satisfactory and recommend that it be accepted.

_____

Lai-Sheng Wang, Ph.D., Chair

_____

Gary S. Collins, Ph.D.

_____

Matthew D. McCluskey, Ph.D.

ACKNOWLEDGMENT

Firstly, I would like to acknowledge my thesis advisor Prof. Lai-Sheng Wang, who provided me with the opportunity and resources for accomplishing my graduate work. It is his hearty encouragement and inspiring instructions that have given me the most confidence in my scientific research and have guided me progressing along a forward path.

I acknowledge all the Wang group members I have encountered for their individual helps to my graduate work. Dr. Hua-Jin Zhai, Dr. Lifeng Cui and Dr. Xuebin Wang generously provided instrumental helps in the early stage of my work. I thank Dr. Wei Huang for being my collaborator in many of the experimental works described in this dissertation. I am grateful to our theoretical collaborators, Prof. Xiao Cheng Zeng, Prof. Alexander I. Boldyrev, and their group members who performed the calculations presented in this dissertation. The collaboration with Prof. Manfred M. Kappes' group on the electron diffraction experiment is also acknowledged. I also would like to acknowledge my thesis committee members, Prof. Gary S. Collins and Prof. Matthew D. McCluskey, for their instructional questions and advices during my thesis work. Thanks to the Chemical & Materials Sciences Division within the W. R. Wiley Environmental Molecular Sciences Laboratory (EMSL) at the Pacific Northwest National Laboratory, where all the experiments were preformed.

Finally, I am indebted to my parents, and my wife Rui He, for their hearty support and encouragement.

PHOTOELECTRON SPECTROSCOPY STUDIES

ON NOVEL DOPED CLUSTERS

Abstract

by Leiming Wang, Ph.D.
Washington State University
December 2009

Chair: Lai-Sheng Wang

Atomic clusters consisting of a few to few hundred atoms exhibit dramatically size-dependent chemical and physical properties, forming the foundation for nano-science and nano-technology. Doping clusters with a foreign atom offers an additional dimensionality to fine tune their structures and properties. This dissertation describes photoelectron spectroscopic investigations on three series of single-atom-doped clusters, with a focus on their size-dependent geometric and electronic structures. In doping the small planar gold clusters (<= Au_{12}^-), as presented in chapter three, we found that Ag- and Cu- doping have little influence on the overall structures of the parent gold clusters, except for MAu_{10}^- where an earlier 2D-3D structural transition was observed for the doped species as compared to the pure gold clusters; whereas the group-14 atoms (Si, Ge, Sn) form strong covalent bond with gold, whose doping significantly distort the planar geometries of the small gold clusters.

In chapter four, we focus on doping the golden buckyball Au_{16}^- with different atoms. We concluded that the nature of dopant-Au interactions is the key factor in determining the structures of the doped golden cage clusters. We have shown that Cu, Ag, Zn, and In atom can be doped inside the golden buckyball with little structural

distortion, while Si-, Ge- and Sn-doping lead to exohedral structures due to the strong dopant-Au local interactions. Transition metal atoms Fe, Co and Ni can also be doped inside Au_{16}^- to form magnetic golden cages. These doped clusters form a new class of endohedral golden buckyballs with tailored properties, analogous to the endohedral fullerenes.

Chapter five presents the studies on a series of carbon-boron clusters: CB_7^-, CB_6^{2-}, CB_6^-, $C_2B_5^-$, and CB_8. These clusters were previously predicted to be novel species containing hypercoordinate carbon atom in planar geometries. However, our studies show that all these clusters adopt low symmetry structures and carbon avoids hypercoordination sites in these species. Thus, in contrast to the theoretical predictions, we conclude that none of these clusters is viable for designing hypercoordinate planar carbon.

TABLE OF CONTENTS

Page

LIST OF TABLES

Page

LIST OF FIGURES

Page

CHAPTER ONE

GENERAL INTRODUCTION

In this era of continuing miniaturization of electronic devices, there is an increasing need to understand and control the properties of materials at nanometer and sub-nanometer scale, with atomic and molecular level precision. Nano-structures with controlled size and dimension constitute the potential building blocks for an entirely new class of materials with tailored properties. Atomic clusters containing a few to few hundred atoms exhibit dramatically size-dependent chemical and physical properties, forming the foundation for nano-science and nano-technology. The research described in this dissertation concerns the investigation of size-selected atomic clusters in the gas phase with a focus on their size-dependent electronic and geometric structures. This section presents a general introduction about clusters and the different techniques used to study clusters.

1.1. Clusters

In dictionary, cluster is defined as "a number of things of the same kind, growing or held together". The clusters in the context of this thesis are particles composed of countable number of atoms, intermediate in size between the individual atom and the bulk. Cluster is a new state of matter, which differs from the bulk material: the quantum states of bulk matter occur in continuous band structures and usually have smoothly varying behavior, while the electronic structures of clusters feature discrete molecular-like energy levels and exhibit strong size dependence. Clusters are also different from

conventional molecules. Molecules are characterized as having fixed compositions and definite structures, whereas clusters can exist in diverse stoichiometries and multiple morphologies (or isomers). Clusters can be neutral or charged. They may be homogeneous, that is, composed of only one type of atoms, or heterogeneous, i.e. made of more than one kind of components. They may be held together by very different kinds of forces, e.g. metallic bonds (as in alkali and coinage metal clusters), ionic forces (as in NaCl clusters), covalent chemical bonds (as in carbon and silicon clusters), or van der Waals attraction (as in He and Ar clusters). Thus, a cluster is simply a group of atoms bound together by forces whose strength and character define its properties.[1-2]

Clusters have peculiar properties because of their nature as intermediate form of matter.[1-4] First of all, being small objects, nearly all the properties of clusters (for example, geometric and electronic structure, melting temperature, magnetic moment) are strongly characterized by quantum size effects. Clusters consisting of a few to few hundred atoms cover a critical size range, in which the finite-sized system evolves from molecular-like to nano-particles to bulk-like. This size range is also known as the non-scaling regime where properties of the system are strongly size-dependent and every atom can make a difference. Study of clusters as a function of size enables one to track the manner in which size dependent properties change from molecular-like to the bulk limit. For instance, a smooth band-gap-shrinking and nonmetal-metal transition has been observed for mercury clusters as the size increases from Hg_3^- to Hg_{250}^-.[5] Second, clusters have large surface-to-volume ratio, i.e. most atoms of a cluster are on its "surface". The Au_{20} cluster may be a good example, it has been shown to have a beautiful pyramidal structure in which all the gold atoms are on the four surfaces of a tetrahedron, each of

which resembling that of Au (111) surface.[6] Thus clusters provide valuable models for surface chemistry and catalysis. In addition, the small size of cluster limits the possible reaction sites. Investigating chemical reactions that occur on or within clusters may provide profound insight into site-specific chemistry on surfaces. Last but not the least, for finite particles, the constraint of translational invariance on a lattice does not apply. So clusters may present more diverse and interesting shapes than the corresponding crystalline structures, providing opportunities to discover new molecules with novel structures and bonding. One can refer to the soccer ball shaped C_{60} cluster as the discovery of a third form of carbon after diamond and graphite.[7] The C_{60} cluster, named Buckminsterfullerene (nickname "buckyball"), probably represents the best fruit yet born out of cluster science, whose discoverers have been awarded the 1996 Nobel Prize in chemistry.[8-10] More recently studied planar tetra-coordinated carbon clusters,[11-12] planar gold clusters,[13-15] planar boron clusters,[16] superhalogen-like Al_{13}^- cluster,[17] Stannaspherene,[18] and all-metal aromatic molecules[19] can all be viewed as novel species with exotic properties that are not found in conventional molecules, whose discoveries substantially enriched and extended our concepts of molecular structures and chemical bonding.

Besides the novel properties interesting for fundamental research, clusters are also promising for several applications. First, there has been intense interest in using supported nanoclusters as model catalysts.[20-21] Since most catalysts are dispersed metal particles,[22] the well-controlled size and composition make clusters ideal systems to elucidate the correlation between the size/composition/shape of a catalyst and its function, which is instrumental to the design of new classes of catalytic materials. Catalysis by

size-selected deposited clusters in fact has become an emerging research field (see, for example, a recent review article[23] and references therein), and recently in-situ characterization of catalytic properties of supported clusters under real working conditions has been realized.[24-25] Another possible application of clusters is to synthesize cluster-assembled materials. Particularly, stable or passivated clusters (sometimes also called "magic clusters" or "superatoms") can be used as building blocks to construct nanostructured materials which may have novel properties. Moreover, cluster-assembled materials offer the flexibility to tailor the material properties through careful selecting and tuning (e.g. via doping) the building blocks and the lattice parameters. Ever since Huffman and co-workers first successfully isolated fullerenes in bulk quantities,[26] only a few years after the discovery of C_{60} in the gas phase,[7] the fullerene-based nano materials have been extensively explored, and have already found applications in nano devices and nano technology.[27] Solution synthesis of tetrahedral Au_{20} cluster[28] and stannaspherenes[29] are two more promising examples along this line. Recently, cluster-assembled materials based on Al_{13} and K_3As_7 clusters have also been proposed.[27] It is conceivable that those novel materials constructed from networks of clusters may eventually find applications in, for example, photovoltaics, tunable band gap materials, and electronic devices at molecular scale.

1.2. Experimental Techniques for Gas-Phase Cluster Production and Detection

Understanding the properties of isolated clusters of well-defined size in the gas phase is an essential first step towards designing cluster-assembled nano-materials. In

order to investigate the properties of clusters, the first question is how to generate clusters in gas phase and how to detect them.

The formation of clusters in the gas phase involves condensation and aggregation of the vapor of the constituents. Clusters will form and grow under supersaturation conditions, that is, if the local vapor pressure is higher than the equilibrium pressure of a given material at a given temperature in the gas phase. So the critical thing to make clusters is to produce the atomic vapor. Generally this can be done by either thermal vaporization, or non-thermal approaches like sputtering, discharge and ablation. In this subsection, a brief summary and comparison of a few most commonly used cluster sources are presented.

Thermal evaporation sources. Thermal evaporation is mostly used to produce intense cluster beams of low-melting point materials.[30-31] In this technique, a bulk target is simply heated in an oven to produce the atomic vapor. The vapor is then entrained in a low-pressure gas flow where nucleation and cluster growth take place. Clusters of alkali elements with more than 10000 atoms have been made with this source.[32] A high-pressure carrier gas can also be used with the thermal evaporation source, in which the vapor/gas mixture is ejected into vacuum via a small orifice to produce a supersonic cluster beam.[33] Such adiabatic expansion into the vacuum can cool the gas mixture to very low temperatures. Thermal sources are suitable for low-melting point materials and produce continuous cluster beam.

Laser ablation supersonic cluster source. Laser vaporization is one of the most popular and powerful techniques to produce clusters, particularly from refractory materials, which was first developed by Smalley and co-workers.[34] In this source, a

strong pulsed laser beam is focused onto a target surface which ablates small amount of materials from the target into plasma with both neutral and charged atomic species. A pulsed high pressure carrier gas (usually helium) is delivered simultaneously with the laser pulse. The rapid cooling due to collisions with the carrier gas initiates the cluster formation. The nascent clusters are entrained in the carrier gas and undergo a supersonic expansion through a small orifice to be further cooled. The laser vaporization technique is very versatile and it can produce clusters from nearly any element (solid form) in the periodic table. Clusters of mixed elements can also be produced with laser ablation source by either using an alloy target or introducing a reactive gas into the carrier gas. For the work presented in this thesis, we use a laser ablation source for cluster production. The details about the apparatus will be described in the next chapter.

Pulsed arc discharge ion source (PACIS). PACIS uses an intense electric discharge instead of a laser pulse to produce clusters. In a PACIS source, an electric arc is ignited between an anode and a grounded, metallic sample cathode as helium gas from a pulsed valve flows through the discharge region.[35] Materials are eroded only from the sample cathode, which generates atomic vapor that is entrained and carried out by the helium gas. This source has some advantages, e.g. the beam produced can be very intense; furthermore, this source is much less expensive than the laser ablation equipment because it does not require a laser. However, the cluster generated in the PACIS is usually of higher temperature than that produced by laser ablation.

Magnetron sputtering source. Magnetron sputtering has long been used in industry, for example, in vacuum coating process. It was introduced by Haberland and co-workers into cluster science to produce very intense continuous cluster beams.[36]

Briefly, in this source, ions are produced by bombarding a target surface with high energy ions (usually Ar^+), and a magnetic field is used to trap secondary electrons close to the target which then undergo more ionizing collisions with neutral gases near the target than would otherwise occur. This enhances the ionization of the plasma near the target and leads to high sputtering rate and thus very intense beam. Similar to laser ablation, there is almost no restriction on target material for the magnetron sputtering source.

Electrospray ionization source. Electrospray was originally invented as a soft ionization technique for biological mass spectrometry.[37] In electrospray, a liquid solution containing the target molecule is sprayed through a syringe needle under high voltage. Charged droplets produced in this way are then fragmented and desolvated to produce the ions of interest. Electrospray is a relatively new technique and has been recently introduced by physical chemists to produce novel gas phase clusters and complexes.[38-39]

After clusters are generated, the first information one wants to know is probably "what clusters are there?" To detect clusters in gas phase, mass spectrometry is the most useful and widely used tool, which measures the clusters' mass and size distribution. In fact all gas-phase investigations of clusters rely on mass spectrometry one way or the other.[1] There are several mass spectrometric techniques that are widely used in cluster research, such as time-of-flight mass spectrometry, quadrupole mass analyzer, ion cyclotron resonance mass spectrometry. Though with different working principles, all these techniques are performed on charged clusters by measuring the mass-to-charge ratios of the clusters. Mass separation of neutral clusters is still an experimental challenge.[1] Here only the time-of-flight method used in the current study will be discussed in the next chapter.

1.3. Structural Studies of Size-Selected Atomic Clusters

Cluster research is a highly interdisciplinary science. Concepts and techniques from many other fields, such as condensed matter physics, chemistry, surface science and even nuclear physics, have been borrowed to study clusters. As discussed above, mass spectrometry has served as a major tool in the investigation of gas phase clusters. Since more stable clusters would be more abundant, the mass distribution of clusters, particularly if combined with photofragmentation or collision-induced dissociation experiment,[40-41] can offer valuable information about the stabilities of the clusters, revealing the so-called "magic clusters" — clusters with significantly enhanced stability relative to their neighbors. Some of the most important discoveries of cluster science, including the buckyball[7] and the electronic shell structure of metal clusters,[42] were indeed borne out from mass spectrometric studies of clusters.

With new and continuously improved experimental techniques, more and more physical and chemical properties of gas phase clusters have been probed. For example, calorimetric studies have been performed to explore the melting temperatures and phase transitions of clusters. Such experiments were mainly carried out by Haberland's group[43] and Jarrold's group;[44] Size-dependent magnetic properties of gas phase clusters have been measured using the traditional Stern-Gerlach experiment, mainly by Cox and co-workers,[45] and by Bloomfield's group[46] and de Heer's group;[47] A variety of spectroscopic methods have been applied to free atomic clusters to study their electronic and vibrational properties.[48-53]

The starting point towards the understanding of cluster properties and to elucidate their structure-property relationships is to determine the structures of the clusters. With

this goal in mind, the first question to ask is: for a cluster of given size and composition, what is its most stable structure? Because of the small size, clusters usually cannot be probed by traditional microscopic and diffraction techniques. In the earlier years, the structural information of clusters was mostly derived from theoretical calculations, which was very limited (by the computing capability) and sometimes quite uncertain. Nowadays, several structure-sensitive experimental techniques have been developed and applied to gas phase clusters. Also with the significantly improved computing capabilities by modern supercomputers, combination of structure-sensitive experiments with the advanced quantum calculations makes it possible to routinely determine the structures of a wide range of clusters with substantial level of credence. In this section, I briefly summarize the working principles and applications of, by no means all, but a few such techniques that are being popularly used currently, with an emphasis on photoelectron spectroscopy — the major method used in my study.

1.3.1. Ion Mobility Experiment

Ion mobility is a spectrometry technique capable of detecting and identifying gas phase species based upon the differential migration of the ions through a homogeneous electric field. Simply put, the ion mobility experiment measures how fast a charged cluster moves in a drifting cell filled with buffer gas at a given pressure, under the influence of a weak electric field. The drifting time of a specific cluster is related to its collision cross section with the buffer gas, which depends on the structure of the cluster. Thus, by comparing the cross sections measured in ion mobility experiments with the theoretical values of calculated candidate structures, one can gain structural information

of the clusters. The ion mobility method was first developed by Mason and McDaniel,[54] and its combination with modern mass spectrometry has been pioneered by Bowers' group.[55] In recent years, high resolution drifting cells have been developed by Jarrold's group[56-57] and Kappes' group[13,58-59], who have applied this technique to structural determination for a wide range of clusters.

1.3.2. Trapped Ion Electron Diffraction

The invention of ion trap[60] has made it possible to store and accumulate clusters for diffraction studies. This experimental technique was first developed by Parks and co-workers, and called trapped ion electron diffraction (TIED).[61] In TIED experiment, usually continuous cluster sources are used to produce a very strong intensity of clusters. Size-selected clusters are stored and thermalized in an ion trap, and then irradiated by an electron beam. Electron diffraction patterns from the clusters are recorded, background corrected and converted into a modified molecular scattering intensity as a function of momentum transfer. This function is structure-dependent and can be theoretically calculated for some trial structures. Thus structures of clusters can be obtained through a "best fit" protocol between experiment and calculation. TIED has been used by Parks' group to study the structures of C_{60}^+, Ag_n^+ and Au_n^- clusters[61-63], and more recently by Schooss and Kappes in the investigations of small gold, silver and tin clusters.[64-66] One part of the work presented in this thesis also involves a collaboration with the latter group using TIED, which will be discussed in chapter four.

1.3.3. Far-Infrared Multiple Photon Dissociation Spectroscopy

Infrared spectroscopy was first used to probe gas phase clusters by Gough *et al.* about two decades ago.[67] Fundamentally, far-infrared multiple photon dissociation spectroscopy (FIR-MPD) is just IR absorption spectroscopy. Due to the small number of clusters (usually $10^2 \sim 10^4$) that can be produced in the cluster beam (relative to the incident IR photons), direct measurement of IR absorption by clusters is not feasible. FIR-MPD does this in a kind of indirect way: it measures the absorption spectrum of a cluster by monitoring the mass depletion of its inert gas complex. Briefly, in a FIR-MPD experiment, clusters are prepared in the form of weakly bonded cluster-inert gas complexes. The beam of the complex of a given cluster is irradiated with a pulsed FIR beam. Resonance of the FIR light with an IR-active vibrational mode of the cluster may lead to absorption of multiple photons which results in heating of the complex and subsequent evaporation of the loosely bonded inert gas ligand, thus a depletion of the corresponding mass signal will be observed. Recording the mass signal of the complex while scanning the IR wavelength gives the absorption spectrum of the cluster. Similar to other techniques, FIR-MPD itself does not directly yield the structure of a cluster. The structural information is obtained through comparison with IR-spectra calculations of trial structures. Such technique has been mainly carried out by Meijer's group, [68-69] and Johnson's group.[70-71] Two related techniques are matrix-isolated IR spectroscopy and infrared resonance enhanced multiphoton ionization (IR-REMPI). In the former, clusters are trapped and accumulated in low temperature matrices, e.g. solid argon, for IR absorption measurements (see e.g. Lindsay[72], Andrew[73]); In the later, IR absorption is

measured as ion yield through multiphoton ionization (see e.g. Meijer[52]). The advantage of those IR techniques is that they are not restricted to charged clusters.

1.3.4. Photoelectron Spectroscopy

Finally, let me come to photoelectron spectroscopy, the major approach of my study. Photoelectron spectroscopy (PES), also known as photoemission spectroscopy, refers to energy measurements of electrons emitted from solids, liquids, or gases upon absorption of electromagnetic radiations. The physics behind photoelectron spectroscopy is the application of Einstein's photoelectric effect, and it provides information of binding energies of electrons in a substance. There have been different terms and applications for PES techniques, depending on what is the ionization energy source. X-ray photoelectron spectroscopy (XPS) was first developed in the 1960's by a group led by Siegbahn[74], who was awarded the 1981 Nobel prize in physics for this contribution. XPS is usually used to probe the atomic core level electrons, primarily in solid state materials, which sensitively depend on the chemical environment around the atom that being ionized, allowing the chemical structure to be determined. With a UV laser, the ultra-violet photoelectron spectroscopy (UPS) has been used to study valence energy levels and chemical bonding, especially of molecular species. This method was first applied by Turner to electronic structure investigation of gas phase molecules.[75] UPS is also the major PES technique that is widely used in research of atomic clusters.

For clusters, PES investigation is usually performed on negatively charged ions (anion), since charged particles are easily size-selected and anions usually have low valence electron binding energies which are accessible for most of the commercial lasers.

In addition, PES on anion clusters yield spectroscopic information about the corresponding neutral species, which are often of interest. Photoelectron spectroscopy studies of anion clusters were pioneered by Lineberger,[53] Smalley,[76] and Meiwesbroer,[77] *et al*. The groups headed by Cheshnovsky,[78] Bowen,[79] Newmark,[80] Wang,[81] Kaya,[82] Haberland and Issendorff,[83] and Ganteför[84] have also made substantial contributions to this field. PES of size-selected anions has now become one of the most important techniques to probe the electronic structures for a broad range of clusters. A related technique is Zero Electron Kinetic Energy Spectroscopy (ZEKE).[48,85] More recently, time-resolved PES[49] and angle-resolved PES (photoelectron imaging)[86] have also been applied to probe the dynamics and photoelectron angular distribution of clusters.

Figure 1.1 shows a schematic view of photodetachment process in an anion cluster photoelectron spectroscopy. We start from a size-selected anion cluster M_n^-, which is, in most cases, in its electronic and vibrational ground state at the experimental temperature. This anion is photodetached by a fixed wavelength photon, resulting in the electronic ground state (M_n), as well as a series of excited states (M_n*) of the neutral cluster (Figure 1.1). The photo-ejected electrons are separated and recorded according to their kinetic energies by an electron energy analyzer. The photoelectron kinetic energy spectrum is a plot of electron signal intensities as a function of its kinetic energy, and it is converted to electron binding energy spectrum by subtracting it from the photon energy used. So the exact quantum mechanical description assigns each feature in the photoelectron spectrum to a transition from the electronic ground state of the anion to different electronic states of the neutral, directly providing the spectroscopic information of the electronic excitation energies of the neutral clusters. Since the time scale of the

Photodetachment Transitions in Anion Photoelectron Spectroscopy

$$M_n^- + h\nu \longrightarrow M_n + e^-$$

$$E_b = h\nu - E_k$$

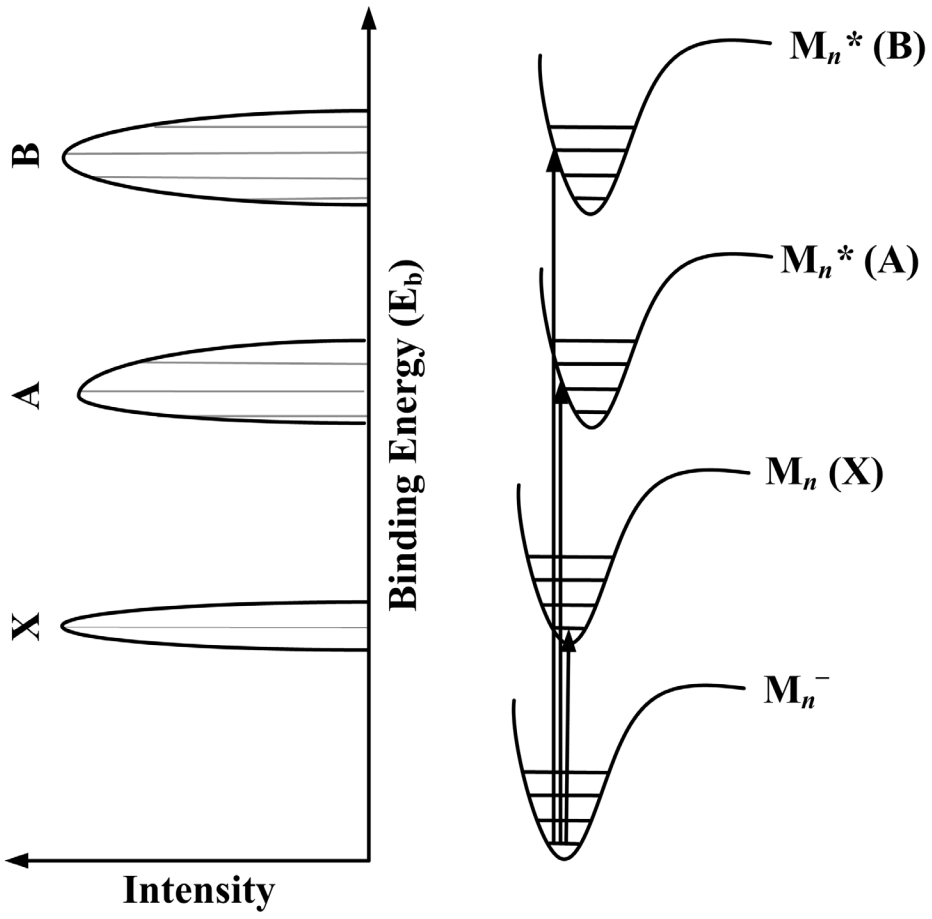

Figure 1.1 A schematic view of photodetachment transitions from the ground state of an anion (M_n^-) to the ground state (M_n) and excited states (M_n*) of the corresponding neutral cluster. The right side schematically shows the potential energy surfaces of each state, and the left is a schematic drawing of the corresponding PES spectrum. E_b and E_k represent binding energy and kinetic energy, respectively, and hν is the photon energy.

Single Particle Picture or MO View of Photodetachment from an Anion

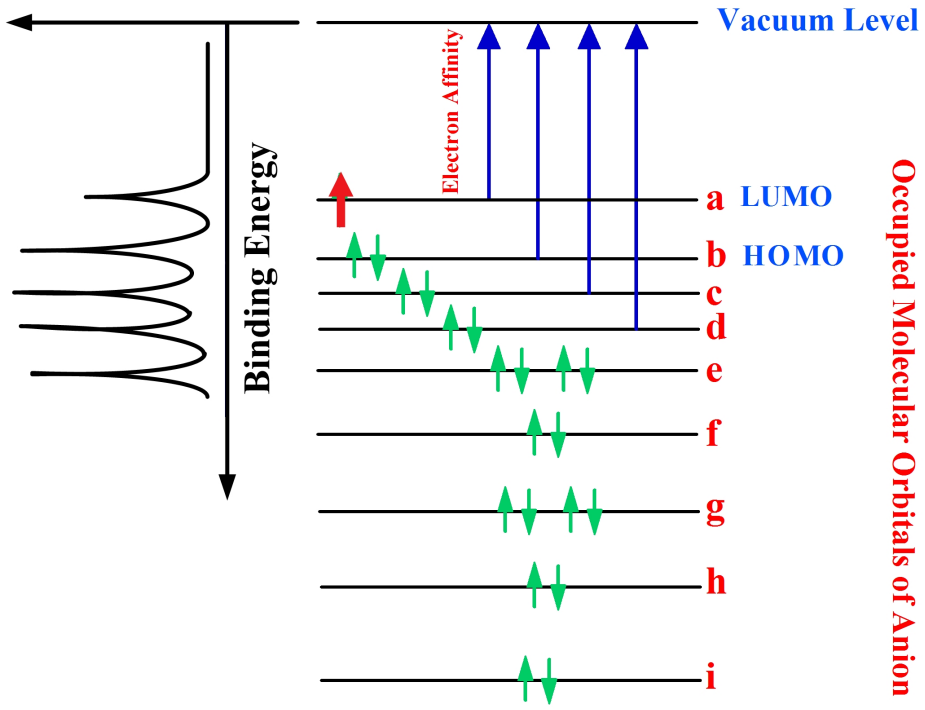

Figure 1.2 Single particle picture or MO view of photoemission process of an anion.

photodetachment process is much faster (~ 10^{-15} s) than the movements of the nuclei (~10^{-12} s), the observed features correspond to the electronic states of the neutral having the ground state geometry of the anion. On the other hand, within each electronic state, the resulting neutral cluster can reside in any number of vibrational energy levels. So the line shape of each transition would be governed by the Franck-Condon progressions,[87] in which the maximum intensity of a transition peak occurs at the vibrational level whose wave function has the largest overlap with that of the parent anion. Peak maximum usually occurs at the vertical transition position (Figure 1.1), and the corresponding transition energy is referred as vertical detachment energy (VDE); while the onset of a PES peak corresponds to the transition to the lowest vibrational level, and is referred as adiabatic detachment energy (ADE). The first ADE also represents the electron affinity, a very important electronic parameter, of the neutral species. In some cases, those vibrational fine structures can also be resolved in the PES spectra.

Alternatively, a simplified way to interpret the PES spectrum is using the molecular orbital theory (MO) (single particle approximation), as schematically shown in Figure 1.2. In the single particle picture, the cluster is viewed as having fixed molecular orbital levels (or density of electronic states) for both the neutral and the anion, and photoelectrons can be viewed qualitatively as being photo-detached from each of the occupied molecular orbitals of the cluster to the vacuum level. Within this approximation, photoelectron spectroscopy directly probes the molecular orbitals (or density of states) of the cluster, and the number of levels can be reached depends on the photon energy used. The simplicity of using this approach to discuss PES spectrum is that, the density of

states can easily be obtained from ground state theoretical calculations and no excited state needs to be considered.

When talking about single particle picture, the electron shell model[42] can sometimes be useful, from which the information about orbital occupations can be qualitatively derived, particularly for metal clusters. In this model, the valence electrons of metal clusters are regarded as free electrons moving in a jellium potential within a spherical volume imposed by the cluster ion core. The energy levels thus derived will adopt similar shell structures as that of the hydrogen atom but without the constraint that the principal quantum number must be larger than the angular momentum term, i.e. 1S 1P 1D 2S·····. Clusters with the number of electrons that corresponds to a major electron shell closure (complete occupation of a shell) are particularly stable, and usually referred as "magic clusters".[3,42]

The single particle picture works reasonably well for simple metal clusters where the electron correlation effect is not strong. However, this approach can only be used for a qualitative interpretation while the following effects must be considered. First, the emission of an electron results in a change of the charge state of the cluster. The remaining electrons will adjust to the changed potential and lead to a set of slightly relaxed energy levels. Second, if the anion is open shell with an unpaired electron, photodetachment from one of the doubly occupied orbitals will result in a neutral final state having two unpaired electrons. These two electrons can couple to either parallel (triplet) or anti-parallel (singlet) spin arrangements which have different energies. Therefore, photodetachment from one single particle orbital can yield more than one features in the spectrum. Usually such multiplicity splitting can be easily identified in the

spectrum since it is associated with each of the doubly occupied orbitals in a similar pattern, and it has a characteristic intensity ratio equal to the degree of spin degeneracy (e.g. triplet/singlet = 3/1). Third, multi-electron processes can further complicate the experimental spectrum than being described by the single particle picture. Multi-electron processes usually have much smaller cross section than the direct photoemission.

In summary, anion photoelectron spectroscopy provides direct measurements of electron affinity, density of states, and electronic excitation energies of clusters. These properties are all structure dependent and make up the electronic fingerprint for a specific cluster. Toward a complete interpretation of PES spectrum and to get structure information of clusters, comparison with high level quantum calculations is often required. In this thesis, close collaborations with theoretical groups have been carried out, by whom various computational programs and theoretical methods at different levels have been employed to calculate the energetics, geometric, and electronic structures of the clusters investigated. Physical and chemical properties of several cluster systems are discussed and understood based on joint photoelectron spectroscopy and quantum calculation studies.

CHAPTER TWO

EXPERIMENTAL SETUP

Our experiments are performed using a magnetic-bottle PES apparatus equipped with a laser vaporization clusters source.[81] Briefly, the gas-phase atomic clusters are produced by a laser vaporization supersonic clusters source. Anion clusters are extracted and their mass distributions are analyzed using a modified Wiley-Mclaren time-of-flight mass spectrometer. The cluster of interest is size-selected by a mass gate, and decelerated before being photodetached by a detachment laser beam. Photoelectrons are collected and measured using a magnetic-bottle time-of-flight electron energy analyzer. A schematic diagram of the experimental setup is displayed in Figure 2.1. The major parts will be described in detail as follows.

2.1. Laser Vaporization Supersonic Cluster Source

For the studies described in this thesis, we used the laser vaporization supersonic cluster source for cluster generation. As discussed in chapter one, this technique was first invented by Smalley's group at Rice University.[34] The source chamber corresponds to the left part in Figure 2.1. The target and nozzle assembly (part 1 in Figure 2.1), which has been modified by the Wang group with a large waiting room,[81] is schematically depicted in more detail in Figure 2.2. As seen in Figure 2.2, an intense pulsed laser beam, which is typically 10-20 mJ/pulse at 10 Hz from the second harmonic of a Nd:YAG laser (532 nm) with 10 nanosecond pulse width, is focused down to ~1 mm in diameter onto a target surface. The target is a 13 mm diameter solid disk adhered to a target holder, which is

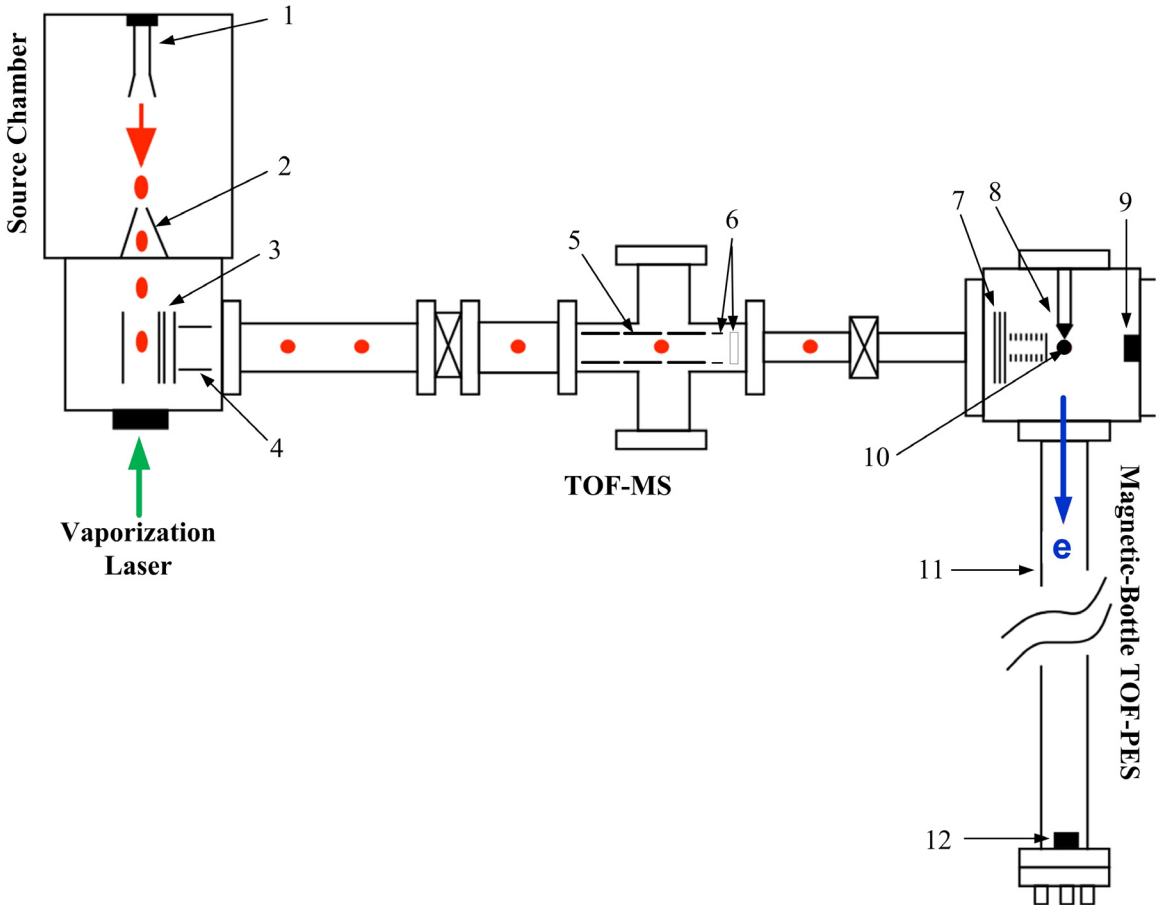

Figure 2.1 The schematic view of the assembly of the laser vaporization, magnetic-bottle photoelectron spectrometer: 1. Target and nozzle; 2. Skimmer; 3. Pulsed ion extraction stack; 4. Ion deflector; 5. Einzel lens; 6. Horizontal and vertical deflector; 7. Mass gate and decelerator; 8. Magnet; 9. Ion detector; 10. Detachment laser beam; 11. 3.5 m electron flight tube; 12. Electron detector. The red dots represent clouds of clusters.

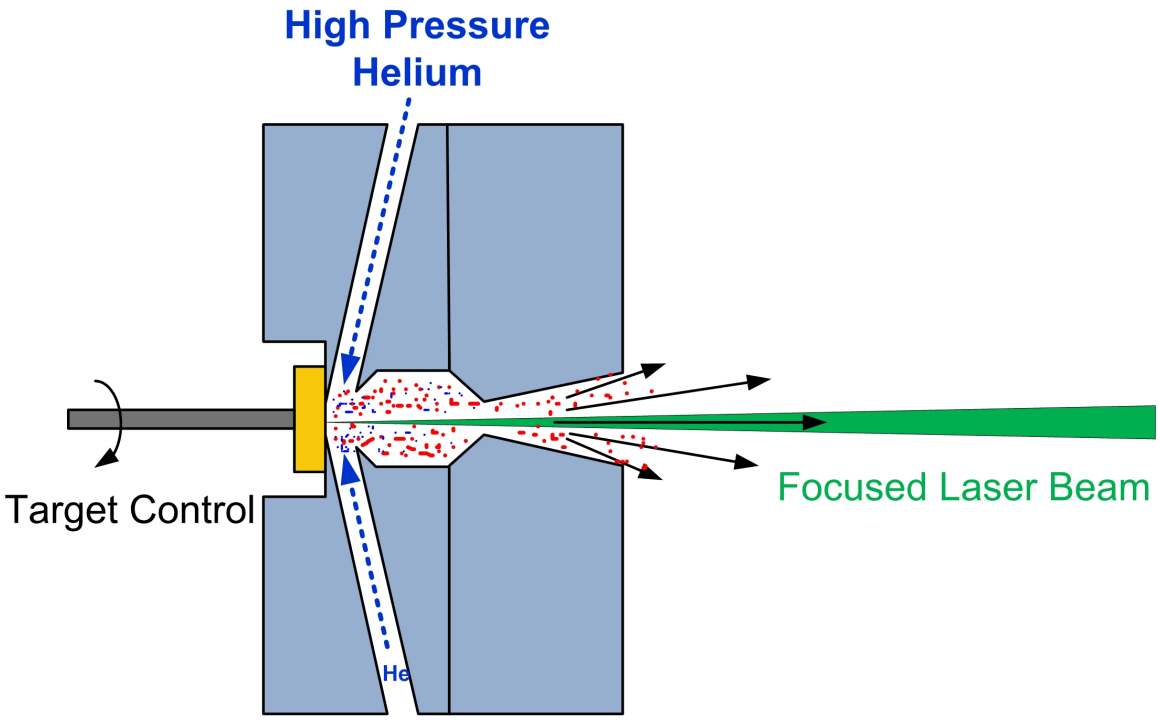

Figure 2.2 The schematic drawing of the target and nozzle assembly (part 1 in Figure 2.1).

controlled by two stepping motors controlling both its rotation and up-and-down translation movements, so that the target surface can be ablated uniformly. The focused laser beam rapidly heats the radiated spot to up to ~10000 K, producing a plume of plasma with both neutral and charged particles. To facilitate clustering, a pulsed high pressure carrier gas (usually helium) is delivered through two symmetrically mounted high-pressure Jordan valves (Jordan Co., CA) (see Figure 2.2) simultaneously with the laser pulse. The stagnation pressure of the carrier gas is 10 atm at each valve. A nozzle with a clustering chamber (waiting room) and a small outlet orifice is used in the source (Figure 2.2).[81] The rapid cooling due to collisions with the carrier gas within the clustering chamber initiates the nucleation process. The initial cluster formation is primarily via three body collisions. When two atoms collide, they form a temporarily bound dimer. This dimer carries all the energy of formation, thus is very hot and highly activated. If it lives long enough to experience a collision with a He atom, it can release its heat of formation to the carrier gas and be stabilized. Once the dimers are formed, the process repeats for trimers and larger cluster formation. Larger clusters usually can live longer before needing a thermalization collision, because they have more internal degrees of freedom which can carry large amount of energy. The nascent clusters formed in the waiting room are then entrained and carried out by the carrier gas through the small outlet orifice and undergo a supersonic expansion into vacuum. This adiabatic expansion process is called supersonic expansion, because the speed of forward mass flow becomes greater than the local speed of sound, which is known to be proportional to the square root of temperature.[88] The supersonic expansion further cools the clusters to very low internal temperatures. Then the carries gas/clusters mixtures pass through a 6 mm

diameter skimmer (part 2, Figure 2.1) to form a collimated cluster beam into the ion extraction zone (part 3, Figure 2.1) where negative ions are extracted perpendicularly.

A sufficiently intense and cold cluster beam is essential for high resolution photoelectron spectroscopy experiment. In practice, we found that the number density and temperature of the clusters produced can be affected by many factors. First, the power of the vaporization laser — Generally larger power can generate more clusters per laser shot, but deposit more energy into them, hence the clusters produced tend to be hotter. In our experiments, the vaporization laser power is usually adjusted to a minimum that suffices to produce a stable and reasonably intense cluster beam; Second, the backup pressure of the carrier gas — The carrier gas pressure determines how efficient the supersonic expansion is: If the carrier gas pressure is too low to provide sufficient cooling or if the plasma is too dilute, only atoms or small clusters can be produced; Third, the length and shape of the nozzle — The length and shape of the nozzle affect the residence time, hence the number of collisions, of the clusters. We found that using a large waiting room nozzle produces relatively colder clusters;[81,89] Fourth, the time delay between the helium pulse and the firing of the vaporization laser — This is a very important parameter (we refer it F1 in our system) governing the cluster formation and its temperature. To obtain stable and cold clusters, the optimal timing to fire the vaporization laser is at the leading edge of the delivered carrier gas pulse, typically 400 ~ 440 μs (F1) after the triggering of the Jordan valves. Firing the laser too early usually produces hot clusters since there is not enough gas to quench the plasma, while firing the laser too late often results in unstable cluster formation. Finally, the residence time of the clusters in the nozzle — We found that the time delay between the firing of the vaporization laser

and the arrival time of the clusters to the extraction stack (F3 time in our system) is another important parameter affecting the cluster temperature.[89] The clusters arrive later spend more time in the nozzle and experience more thermalization collisions with the carrier gas, therefore they are colder. The F3 timing provides an important parameter to control the temperatures of the clusters, which is vital for high quality PES spectra.

Clustering condition is usually different for different target materials and different cluster size range. The appropriate conditions for optimal signals can be obtained through a computer-controlled scan of the F1 and F3 timing parameters.

2.2. Time-of-Flight Mass Spectrometer

When the clusters generated reach the ion extraction (repeller) zone, a negative high voltage pulse is applied to the repeller (3, Figure 2.1). So the negatively charged clusters are extracted perpendicularly from the beam and are subjected to a time-of-flight (TOF) mass analysis. The mass analyzer used in our experiments is a modified Wiley-Mclaren type time-of-flight mass spectrometer, which was first invented by Wiley and Mclaren[90], and later de Heer and co-workers introduced the modified version for large volume ion extraction and simultaneous high resolution.[91] Time-of-flight method is one of the most popular mass spectrometric techniques, and it is particularly suitable for pulsed experiments. Basically, in the TOF mass spectrometry, all ions are accelerated to the same amount of kinetic energy, so the resulted velocities will be different for ions with different mass. Hence the mass distributions can be obtained by measuring the flight time of the ion beam in a given distance. Figure 2.3 shows a schematic drawing of the extraction stack assembly and its voltage supply. The major modification is an addition of

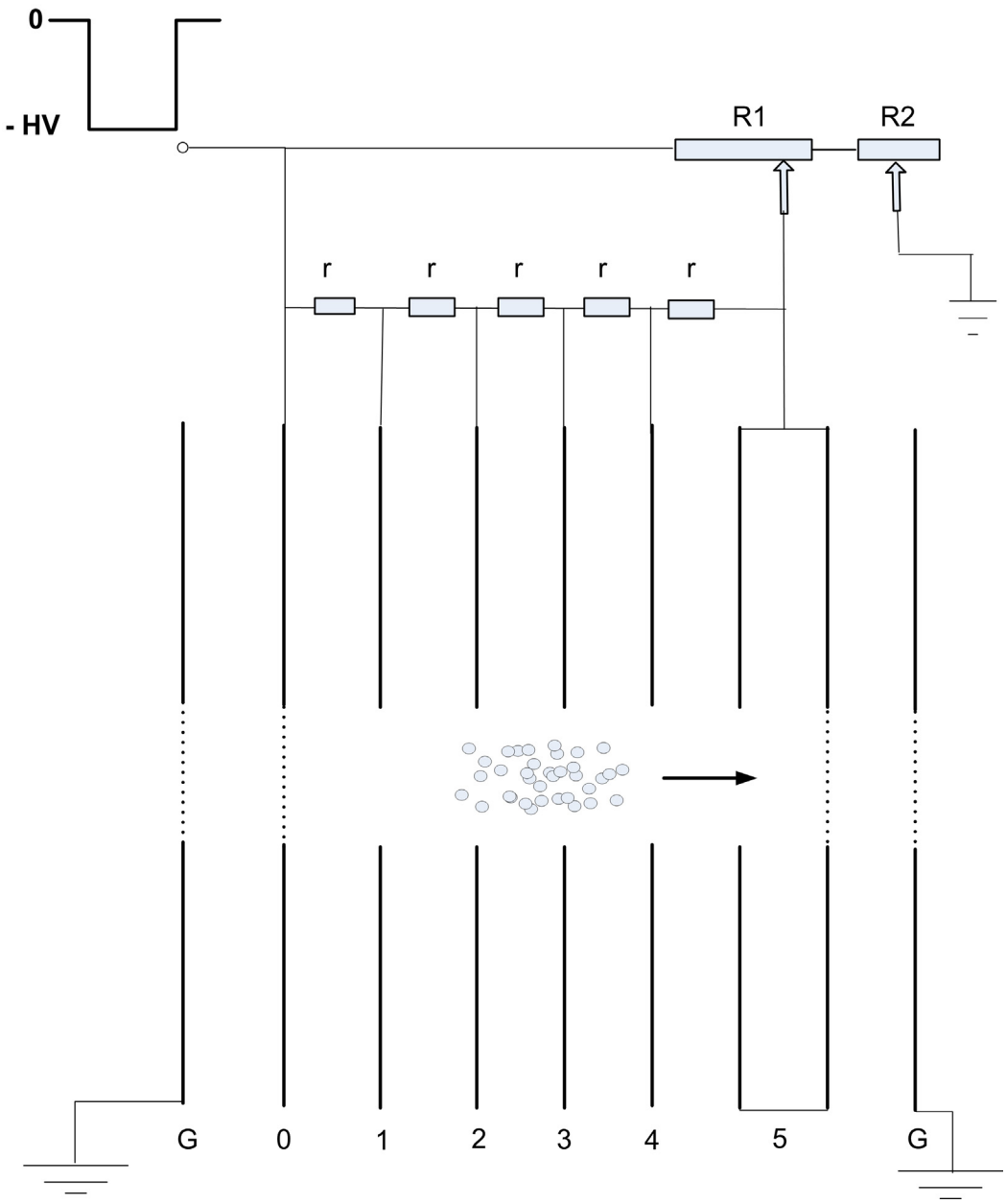

Figure 2.3 The assembly of the ion repeller (part 3 in Figure 2.1) and its voltage supply.

a short free-flight zone (5, Figure 2.3) in between the two acceleration stages of the original Wiley-Mclaren design. Such modification allows us to achieve a moderate mass resolution of $M/\Delta M \sim 300$. Higher resolution can be achieved using a reflectron,[92] which is readily coupled to our system. Right after the extraction stack, there is a horizontal ion deflector (4, Figure 2.1) to compensate for the initial beam velocity. The deflector is an electrostatic stainless steel stack similar to the repeller, and the voltage applied to it can be scanned and adjusted through a computer controlled DA converter so that a certain range of clusters can be directed to the ion detector. In the TOF tube, an einzel lens is used for spatial focus of the ions (5, Figure 2.1). It consists of three isolated copper cylinders. The two end cylinders are grounded while the middle one is floated at - 400 V (typically if -1kV is used for the repeller). Another horizontal and one vertical deflectors are located next to the einzel lens (6, Figure 2.1), which can be used to further adjust the beam direction.

During the experiments, several practical parameters need to be tuned to achieve optimal working conditions. First, the orientation of the repeller with respect to the fight tube can be rotated. The angle of the repeller and the voltage on the deflector together determines the favorable conditions for a specific size range of clusters that can be detected. The high voltage and its pulse width applied to the repeller can be increased for heavier clusters. To achieve best mass resolution, the relative ratio of the high voltage divided among the two stages of the extraction stack needs to be carefully tuned (through the two variable resistors R1 and R2 in Figure 2.3). The voltage on the focusing einzel lens also needs to be tuned accordingly.

2.3. Mass Selection and Momentum Deceleration

During PES experiments, only the clusters of interest are selected to enter the photodetachment zone for photoelectron measurements. The cluster to be investigated is mass selected by a mass gate and decelerated by a momentum decelerator before being photodetached. A schematic drawing of the mass gate and decelerator is shown in Figure 2.4. The mass gate consists of three grids. The first and third grids are grounded, and the middle one is held at a negative high voltage (usually slightly higher than the repeller voltage), so that no anion cluster is able to pass. Once the desired cluster arrives at the first grid, the high voltage on the mass gate is pulsed to ground for a short period of time, allowing this cluster to pass unaffected. After the selected cluster passes the mass gate, the high voltage is restored to block other ions. A fast transistor switch is used to deliver the high voltage pulse for the mass gate. The pulse width, thus the open time of the mass gate, can be adjusted from a few hundred nanoseconds to microseconds, depending on the peak width of the mass signal for the desired cluster.

Following the mass gate, the selected cluster clouds enter a momentum deceleration zone, as shown in Figure 2.4. After the cluster packet passes the last grid of the mass gate, a positive square high voltage pulse is applied to this grid to decelerate the ions. The high voltage is pulsed back to ground before the ion packet leaves the deceleration stack, which consists of ten guarded rings to ensure a uniform deceleration field. Both the amplitude and width of the deceleration pulse can be varied to achieve the best deceleration effect. During the deceleration, all ions experience the same decelerating force within the same period of time, i.e. same impulse, thus will be decelerated by the same amount of linear momentum. In contrast to the conventional

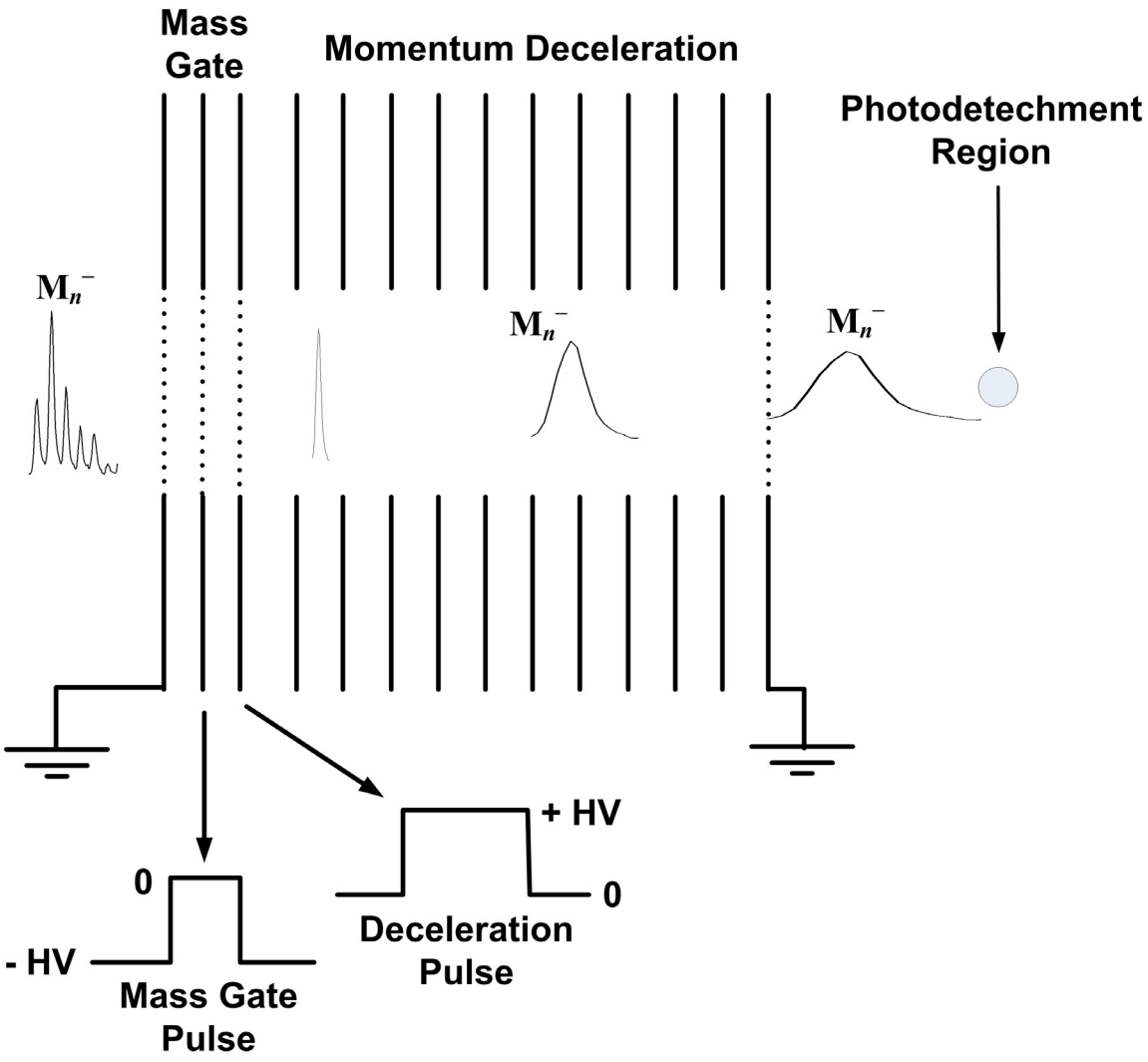

Figure 2.4 Schematic drawing of the mass gate and momentum decelerator.

retarding field deceleration in which all ions pass through a constant electric field, the advantage of momentum deceleration is that after the deceleration the energy spread among the initial ion packet is decreased.[81] The deceleration of ions before carrying out the photodetachment is crucial to the photoelectron energy resolution, because it minimizes the Doppler effect caused by the ion velocity. However, the deceleration causes a temporal spread of the ion packet and decreases the ion density, as schematically shown in Figure 2.4, which will lead to less electron signals. In practice, the given cluster anion is usually decelerated down to such low velocity that the Doppler broadening is no longer a dominant factor for the electron energy resolution.

2.4. Magnetic-Bottle Time-of-Flight Photoelectron Energy Analyzer

The mass selected and decelerated cluster beam is now entering the detachment zone (10, Figure 2.1) for photodetachment. A pulsed light beam from the detachment laser is fired to intersect the cluster beam, and the energy distribution of the photo-emitted electrons is measured by a magnetic-bottle time-of-flight electron energy analyzer. The TOF method is most commonly used for experiments operated at pulsed mode. It measures the kinetic energies of electrons by measuring its flight time in a given length flight tube. The magnetic-bottle type TOF photoelectron spectrometer (MTOF) first introduced by Kruit and Read is ideal for cluster studies because of its high electron collecting efficiency (2π solid angle),[93] which can compensate for the usually low ion intensity. In our experiment, a modified version of the MTOF apparatus is used, which can collect all the electrons emitted in 4π solid angle.[76]

As shown in Figure 2.1, the MTOF is located at the end of the TOF mass spectrometer. A strong magnetic field is generated by a permanent magnet with a V-shape of 75 degree (8, Figure 2.1), which is machined from a magnetic rod with 3/4 inch in both diameter and length. It produces a magnetic field of about 5000 Gauss at the tip position, which rapidly drops to about 400 - 800 Gauss at the photodetachment zone. To minimize residual electric field, the magnet tip is covered by a V-shaped stainless steel cap. An electric solenoid is wound around the 3.5 m electron flight tube to produce a uniform weak field throughout the tube. To avoid the influence of the earth magnetic field, the flight tube is covered by μ-metal shielding. The photoemitted electrons at the detachment zone are reflected by the high magnetic field and guided by the magnetic line toward the electron detector mounted at the end of the flight tube (12, Figure 2.1). The distance between the magnet tip and the detachment point can affect the electron collecting efficiency and the energy resolution. If the distance is too short, it can generate large noise signals by scattered photons, particularly for short wavelength detachment laser. Generally, a short distance is used for 532 and 355 nm experiments to achieve optimal PES resolution, since energies of these photons are too low to ionize the magnet material to produce noise electrons. The distance is increased for photon energies higher than 266 nm.

The photodetached electrons are detected by a set of three micro-channel plates (Jordon Co.), and the TOF spectra are recorded. Photoelectron detachment and measurement is operated at 20 Hz, twice as that of the laser vaporization source. That is, the detachment laser is fired alternately with and without the cluster beam presented, and the alternating shots without the beam are used for background subtraction.

The detachment lasers used in our experiments usually include two harmonics of a Nd:YAG laser (355 nm, 266 nm), and a 193 nm from an ArF excimer laser. In our system, the kinetic energy of a photoelectron is expressed as a function of its time of flight as: $E_k = a + b/(c+t)^2$, where t is the electron flight time, and a, b, c are parameters related to individual experimental conditions of the whole MTOF system. A number of sources can cause shift of these instrumental parameters, for example, the variation of vacuum conditions, or slight changes in detachment laser position. Accurate energy measurements require proper and frequent calibrations of the system. In practice, the machine is calibrated, usually on a daily basis, using the known spectra of Au^- (for 193 nm), Cu^- or Rh^- (for 355 and 266) atomic anions.

2.5. Experimental Control and Operation

The whole experiment was performed within vacuum chambers that were sustained by a differential pumping system. Generally, when the experiment is off, the background pressure in the source chamber, extraction zone, TOF tube, and detachment zone is on the orders of 10^{-6} Torr, 10^{-8} Torr, 10^{-9} Torr and 10^{-10} Torr, respectively. During the experiment, the corresponding pressures drop by about one order of magnitude.

The experiment was operated in pulsed mode. Figure 2.5 shows the timing sequence in one experimental cycle and the corresponding timing parameters defined in the software. First, the Jordan valve is triggered to deliver the He carrier gas. There is about 400 μs delay between the trigger signal and the arrival of the He to the nozzle. After a delay time (F1) relative to the Jordan valve trigger, the vaporization laser is triggered to fire, usually it is at the leading edge or the peak maximum of the He pulse.

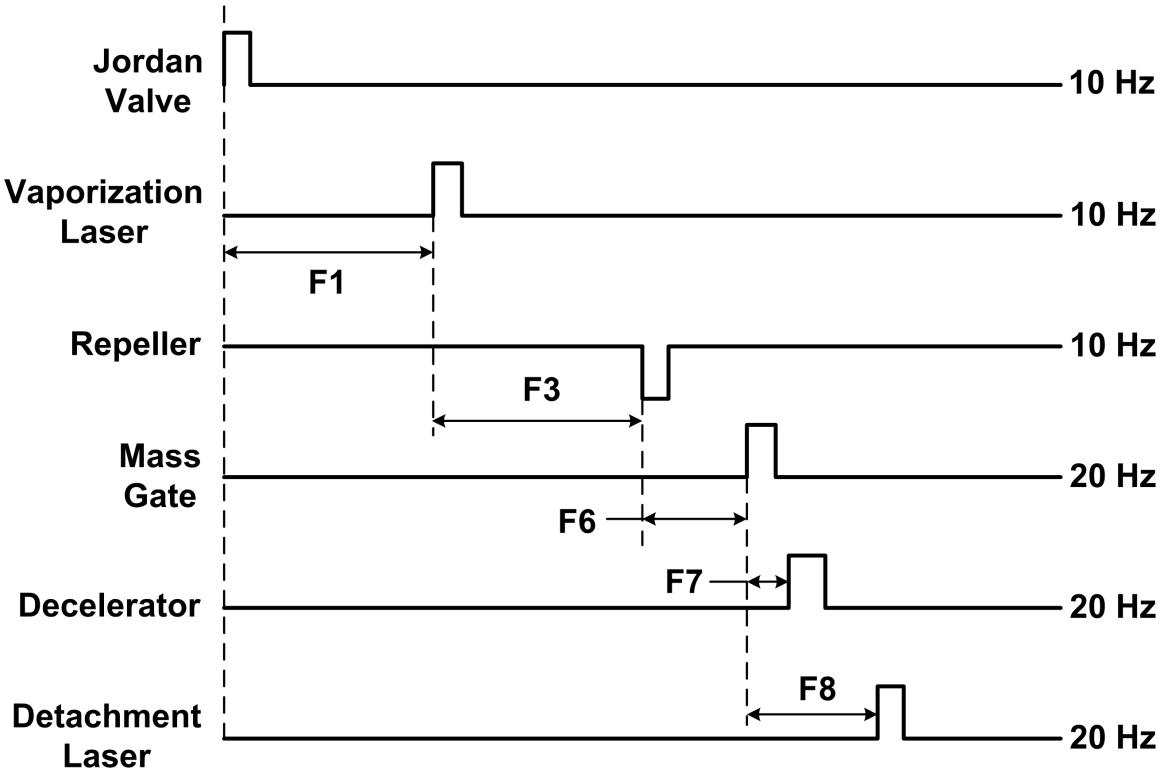

Figure 2.5 Experimental timing sequence.

When the produced clusters reach the center of the extraction zone, the high voltage to the repeller is trigged on. The time delay between the trigger of extraction voltage and the vaporization laser is defined as parameter F3 in the software, which is usually in the range of 250 ~ 400 μs. The mass gate timing is roughly 88% of the total time-of-flight of a given ion. The time delay between the mass gate and the repeller trigger (F6) can be adjusted to select the desired cluster. The time delay between the mass gate pulse and the deceleration pulse is defined as parameter F7, it is usually manually tuned in the range of 0.4 ~ 3 μs. Finally, the detachment laser is triggered to fire after a short delay time (F8) relative to the mass gate signal.

The entire experiment is controlled by a PC through a Computer Automated Measurement And Control (CAMAC) interface. In each experimental cycle, the computer issues a sequence of commands to generate timing pulses and delays through the CAMAC interface to initiate the experiment and acquire the data. These timing parameters discussed above are all scanable so as to achieve optimal operational conditions for each experiment.

2.6. Performance of the Photoelectron Spectrometer

We used Cu^- to test the performance of our photoelectron spectrometer. Figure 2.6 shows the typical PES spectra of Cu^- at three different photon energies, 3.496 eV (355 nm), 4.661 eV (266 nm) and 6.424 eV (193 nm). At 355 nm and 266 nm, three transition peaks are observed at 1.23 eV, 2.62 eV and 2.88 eV respectively. They correspond to the detachment transitions from the ground state of Cu^- (^1S, $3d^{10}4s^2$) to the ground state ($^2S_{1/2}$, $3d^{10}4s^1$) and the spin-orbit-split excited states ($^2D_{5/2,\ 3/2}$, $3d^9 4s^2$) of Cu.

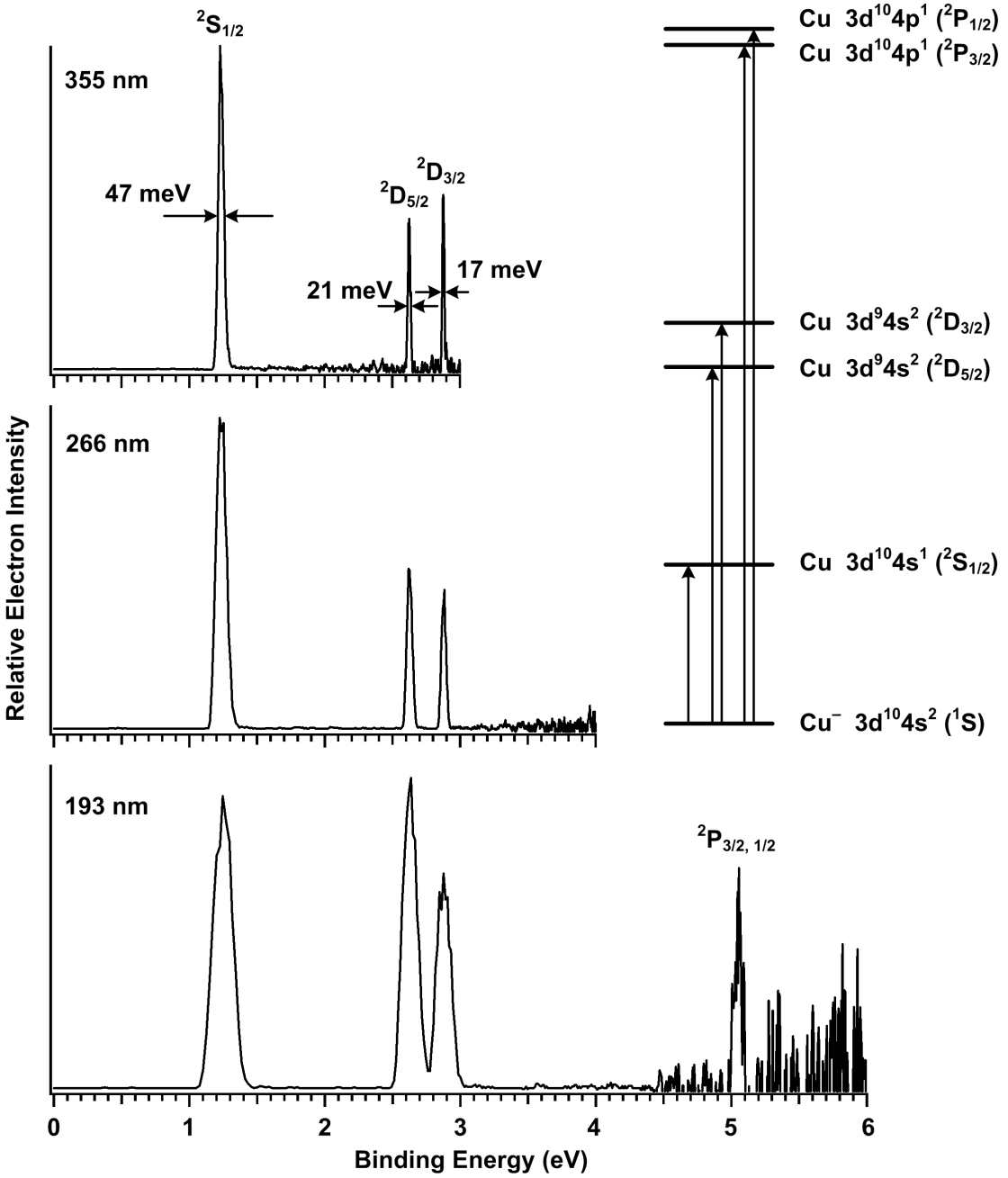

Figure 2.6 Photoelectron spectra of Cu^- at 355 nm (3.496 eV), 266 nm (4.661eV) and 193 nm (6.424 eV).

In the 355 nm spectrum, the peak widths (FWHM) for the $^2S_{1/2}$, $^2D_{5/2}$, and $^2D_{3/2}$ states are 47 meV, 21 meV, and 17 meV, respectively, indicating that the energy resolution depends on the electron kinetic energies. This dependence is also shown clearly by the increasing band widths for the 266 nm and 193 nm spectra. The 355 nm spectrum represents the best resolution of our PES spectrometer, which is $\Delta E/E$ ~2.5 %, i.e. about 25 meV for 1 eV kinetic energy electrons.

Another observation from the spectra is the photon energy dependence of detachment cross sections for different transitions. Since our magnetic-bottle spectrometer collects nearly 100% of the photoelectrons, the relative peak intensities thus represent the relative intrinsic detachment cross sections. As can be seen from Figure 2.6, the cross sections for the ^2D transitions increase with photon energies relative to that for the ^2S state. This is in line with the general observations in PES experiments that cross sections for detaching electrons from high angular momentum orbitals usually increase with photon energies. The variation of the detachment cross section with photon energies depends on the symmetry of the orbital and sometimes provides useful information for spectral assignments.

Finally, we note that a new peak at around 5 eV is observed in the 193 nm spectrum. This peak can be assigned, based on Cu atomic energy levels,[94] to the detachment transition to the ^2P excited state of the known atomic energy levels of Cu with a $3d^{10}4p^1$ electron configuration (see Figure 2.6). There is a small spin-orbit splitting ($^2P_{3/2}$ and $^2P_{1/2}$, 30 meV) which is not resolved by the 193 nm spectrum. Since the initial state is Cu^- (^1S, $3d^{10}4s^2$), the ^2P states are resulted from detaching one 4s electron and at the same time exciting another 4s electron to the 4p orbital, thus it is a two-electron

process. Such transition is usually called satellite or shake-up process and is due to electron correlation effects. Multi-electron transitions usually exhibit very small cross sections. It is surprising that the intensity of the ^2P state observed here is almost comparable to the main transitions, suggesting very strong electron correlation effects in Cu^-.

CHAPTER THREE

DOPING THE SMALL PLANAR GOLD CLUSTERS

3.1. General Introduction and Motivation

Bulk gold is the most noble, and probably the most inert metal in the periodic table; it does not tarnish on exposure to the air and retains its beautiful luster undiminished for millennia. Because of its chemical inertness as a bulk metal, gold appeared to provide very limited opportunities to open up new and exciting chemistries and received relatively little research attention. However, this is not now the case. The discovery that gold, when sub-divided to the nanometer scale, can be exceptionally active as a catalyst has spurred a huge interest in gold-containing systems, leading to an explosive growth in the volume of both experimental and theoretical researches on gold.[95] Now gold chemistry has become one of the most rapidly growing fields, attracting interest from several interdisciplinary areas, such as material science, catalysis, surface and synthetic chemistry. A collection of comprehensive reviews discussing the current research on gold can be found in a recent thematic issue of *Chemical Society Reviews*.[96]

The unique catalytic effects of gold nanoparticles supported on oxide substrates were first discovered by Haruta,[20] and it stimulated a flurry of research aiming at understanding its catalytic mechanisms and controlling the catalytic activities. It has been shown that catalytic properties of nanogold are sensitive to many factors, e.g. the nature of the substrate, the size, shape and charge state of the gold particles.[97] However, so far there has not been a conclusive picture concerning the mechanism of the peculiar catalytic properties of nano gold particles. A detailed understanding of the geometric and

electronic structures of free gold clusters is a prerequisite, which may hold the key to elucidating the catalytic, as well as other chemical and physical properties of supported gold nanoparticles. Motivated by this goal, during the past decades, there have been extensive experimental[6,13,15,59,69,98-108] and theoretical[14,109-119] studies dedicated to the size-dependent structural properties of both neutral and charged gold clusters. One of the most intriguing findings has been the discovery that small gold cluster anions possess planar structures up to Au_{12}^- and the 2D to 3D transition happens at a surprisingly large size of $n \geq 12$. The unusual preference of 2D structures by Au_n^- clusters was discovered by density-functional theory (DFT) calculations and ion mobility experiments,[13] and was explained to be due to the strong relativistic effects of gold,[14,109] which reduces Au 5d-6s energy gap and enhances the s-d hybridization. Subsequent photoelectron spectroscopy[15] and trapped ion electron diffraction[106,120] studies confirmed the planar structures of the small gold cluster anions and the 2D-3D structural transition at Au_{12}^-. Very recently, using Ar-tagging we further confirmed the coexistence of 2D and 3D structures and obtained isomer-specific PES spectra for Au_{12}^-.[121] Other interesting structures observed for gold clusters include the hollow golden cages Au_{16}^- – Au_{18}^-,[105-106,122] the gold pyramids Au_{20}^- and Au_{20},[6,69] and a possible tubular structure of Au_{24}^-.[123-124]

So far, the structures of pure gold clusters with less than about 20 atoms in size have been well established through joint experimental and theoretical studies, while continued efforts are being taken to solve the larger ones. On the other hand, doping with impurity atoms offers an additional dimensionality to fine tune the structure and property of gold clusters. For example, doping a W atom in Au_{12}^- results in an endohedral cluster with a beautiful icosahedral (I_h) structure;[125-126] while doped with a Si atom, the planar

structure of Au_4^- changes to a tetrahedral $SiAu_4^-$.[127] A series of transition metal atom doped gold clusters have been investigated through photofragmentation experiments and density functional theory (DFT), mainly by Lievens' group.[128-130]

In this chapter, I present our studies on doping the small planar gold clusters with two different groups of atoms, the group-11 atoms Ag and Cu, and group-14 atoms Si, Ge and Sn. We are interested in seeing how the unique planar structures of small gold clusters are affected by doping. Ag and Cu are congeners of Au, and they are expected to have little influence to the overall structures upon doping, while group-14 atoms are strongly covalent elements, whose doping may significantly distort the planar geometries of the parent gold clusters.

3.2. MAu_n^- Clusters (n = 8 – 11, M = Ag, Cu)

3.2.1. Introduction

Clusters of the two lighter coinage metals, silver and copper, are known to have structures very different from gold clusters (except for the small ones less than tetramer[131]), and the onset of 3D structures for $Ag_n^{0/+/-}$ and $Cu_n^{0/+/-}$ appears at relatively small sizes compared to gold clusters.[132-133] Similar to gold, the electronic character of Ag/Cu is also featured by a single s-valence electron with a completely filled d shell. However, there are significant differences between them, such as different atomic radii, different electronegativities, and particularly the much stronger relativistic effects in gold than silver and copper.[109] A natural question is what happens if one or more gold atoms in gold clusters are replaced by silver or copper? In comparison to pure gold clusters, the studies on mixed coinage-metal clusters are relatively scarce. The AgAu and CuAu dimers and some of the mixed trimers have been experimentally studied using resonant two-photon ionization spectroscopy.[134] Joint ion mobility measurements and DFT calculations on gold-silver mixed cations ($Ag_mAu_n^+$, $m + n < 6$) revealed significant charge transfers from silver to gold atoms,[135] in agreement with a previous DFT study.[131] The stability of photofragmented $Au_nX_m^+$ clusters (n = 1 – 65, m = 1, 2; X = Cu, Al, Y, In) were studied using mass spectrometry, where the Cu atom doped clusters ($n \leq 38$) were observed to have same shell closures as the corresponding pure gold clusters.[40] Photoelectron spectra of Au-Ag binary cluster anions up to tetramer[136] and of Au_nCu^- (n = 2–7) clusters[137] have been reported at a photon energy of 4.661 eV. Theoretically, the dimers and trimers of mixed coinage metals has been calculated using 19-electron effective core potential,[138] and more recently at the level of CCSD(T).[139] Structures of

single Cu atom doped gold clusters $Au_{n-1}Cu^-$ in the size range of n = 13–19 has recently been predicted.[140] DFT investigations on the geometric and electronic structures of small Au-Ag binary clusters with varying component Au_mAg_n (usually $m + n \leq 10$) have been reported by several groups.[131,141-142] Larger Ag/Cu-Au bimetallic systems have also been studied theoretically.[143-145]

In this sub-section, I present a combined PES and DFT investigation on a series of small gold cluster anions doped with a single Ag/Cu atom, $AgAu_n^-$ and $CuAu_n^-$ (n = 8 – 11). We chose the size range around the 2D-3D transition point known for pure gold anion clusters and our attention is focused on several questions: How do the atomic and electronic structures of the gold clusters change upon the isoelectronic substitution? Can the doped cluster anions maintain the unique 2D structures up to the same size as pure gold clusters? Our results show that the isoelectronic substitution induces an earlier 2D-3D transition for the doped clusters MAu_n^- than pure gold anions by one atom in size.[146]

3.2.2. Experimental Results

We used an Au/Ag or Au/Cu mixed disk target containing about 7% Ag or Cu, respectively, to produce the $AgAu_n^-$ and $CuAu_n^-$ clusters for PES study. The 193 nm photoelectron spectra of MAu_n^- from n = 8 to 11, as well as those of the corresponding pure gold clusters Au_{n+1}^- [15] are presented in Figures 3.1–3.4, respectively. The assigned structures and their simulated PES spectra are also shown for comparison, and will be discussed below. The first VDEs of the doped clusters (for the major isomer if there are multiple isomers) are given in Table 3.1 where they are compared to those of the pure gold clusters and the calculated values.

MAu_8^-. As shown in Figure 3.1, the PES spectrum of Au_9^- is featured with two intense and sharp peaks (X and A) at around 4 eV, and a large energy gap which separates these doublet peaks with the higher binding energy bands. The spectra of $AgAu_8^-$ and $CuAu_8^-$ (Figure 3.1b, c) are very similar to that of Au_9^-, both featuring the abovementioned doublet bands and the characteristic gap. The clear similarities observed in the spectra between MAu_8^- and Au_9^- suggests that Ag/Cu simply substitutes one Au atom and does not significantly alter the atomic and electronic structure of the parent cluster. However, an additional small peak is observed in the spectrum of $AgAu_8^-$ (X', Figure 3.1b) and that of $CuAu_8^-$ (X', Figure 3.1c). Such weak features in PES usually indicate presence of multiple isomers, which is very possible for MAu_8^- considering that there are multiple unequivalent substitution sites available in the structure of Au_9^-.

MAu_9^-. The photoelectron spectrum of Au_{10}^- has been shown to contain contributions from at least four isomers.[147] As shown in Figure 3.2a, the major features of the spectrum (X and higher binding energy part) show very high binding energies and lack an energy gap between the highest occupied molecular orbital (HOMO) and the lowest unoccupied molecular orbital (LUMO). They were known to come from a major isomer, while weak features at the low binding energy part (X', X'', X''') were suggested to be due to minor isomers.[147] At first glance, the spectra of $AgAu_9^-$ and $CuAu_9^-$ are very different from that of Au_{10}^-, in which the first peak with appreciable intensity (X'') appears at much lower binding energy and a fairly large HOMO-LUMO gap is observed for $AgAu_9^-$ and $CuAu_9^-$ (Figure 3.2b, c). In addition, the spectra of $AgAu_9^-$ and $CuAu_9^-$ show much more complicated spectral features at >= 4 eV range than that of Au_{10}^-. However, a careful reexamination reveals that the low binding energy peaks in the

spectra of $AgAu_9^-$ (X' and X'') and $CuAu_9^-$ (X', X'', and X''') may have one-to-one correspondence to those weak features in Figure 3.2a, and the spectra of the doped clusters are indeed similar to that of Au_{10}^-, except that X'' and X''' (only X'' for $AgAu_9^-$) are much more intense in the spectra of the doped clusters. The similarity for the X bands among three spectra is also discernable in terms of the peak position and shape (Figure 3.2). This suggests that there are also multiple isomers, similar to those of Au_{10}^-, presented in the beam of MAu_9^-, possibly with nearly equal contributions (X' may still be from a minor isomer according to its relatively low intensity) to its observed spectrum. Overlap and superposition of contributions from multiple isomers is consistent with the very complicated spectral patterns observed for $AgAu_9^-$ and $CuAu_9^-$, particularly in the high binding energy range.

MAu_{10}^-. The spectrum of Au_{11}^- features totally six well resolved detachment bands in the binding energy range of ~ 3.5 – 5.5 eV, with three very isolated peaks (X, A and B) in the front followed by three close ones (Figure 3.3a). Two weak peaks are discernable at the high binding tail of band X (X') and in between bands A and B (A'), respectively, indicating population of minor isomers. As shown in Figure 3.3, the spectral patterns of the doped clusters MAu_{10}^- are totally different from that of Au_{11}^-, suggesting that at this size, Ag/Cu substitution may substantially alter the structure of the parent gold cluster rather than simply replacing one Au atom. The spectra of $AgAu_{10}^-$ and $CuAu_{10}^-$ are in fact similar to each other (Figure 3.3b, c), both displaying four well resolved peaks at ~3.5 – 4.5 eV and followed by a sizable energy gap and then more congested signals at higher binding energy range. This suggests that the doped clusters $AgAu_{10}^-$ and $CuAu_{10}^-$ may have similar structures, though most likely different from that of Au_{11}^-. We note that,

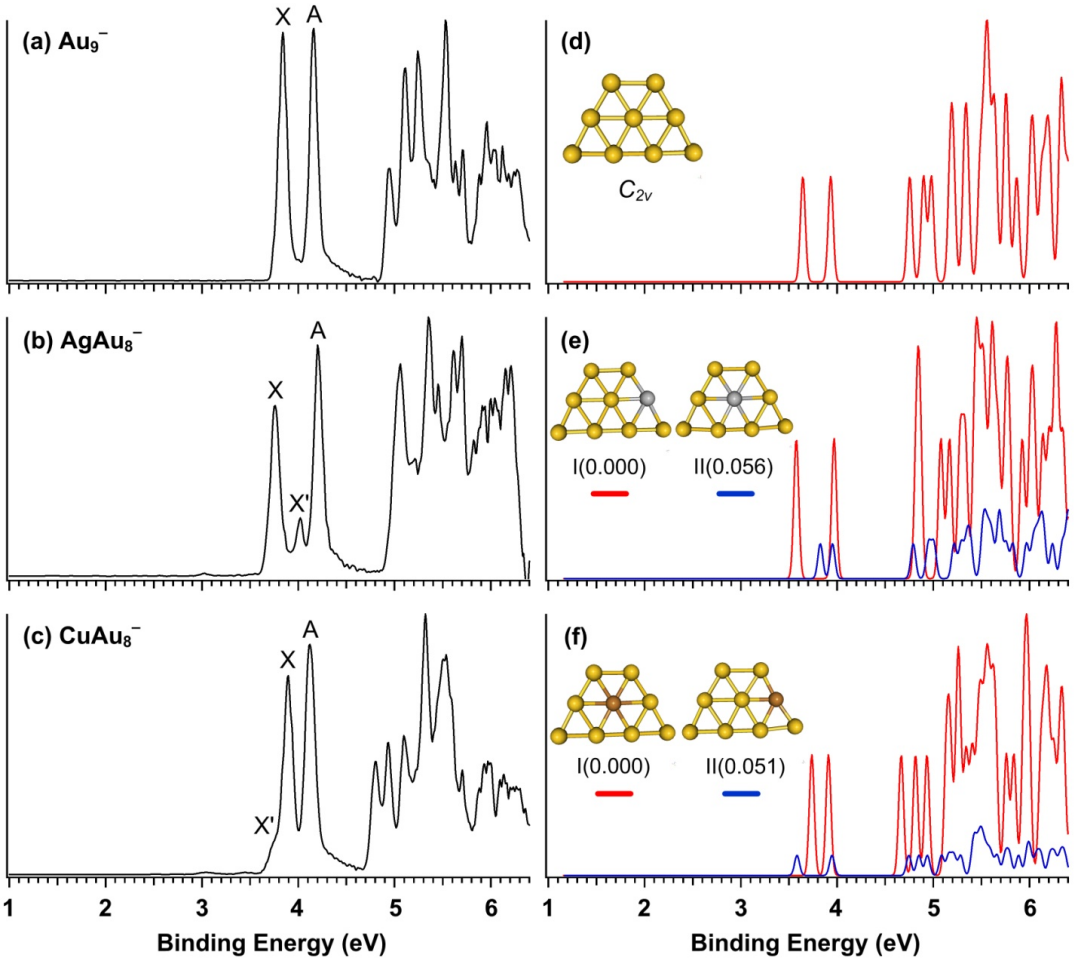

Figure 3.1 Experimental (left, a-c) and simulated (right, d-f) photoelectron spectra of Au_9^-, $AgAu_8^-$ and $CuAu_8^-$. The insets show the corresponding structures. The atoms are shown in colors as: Au (yellow); Ag (gray); Cu (brown).

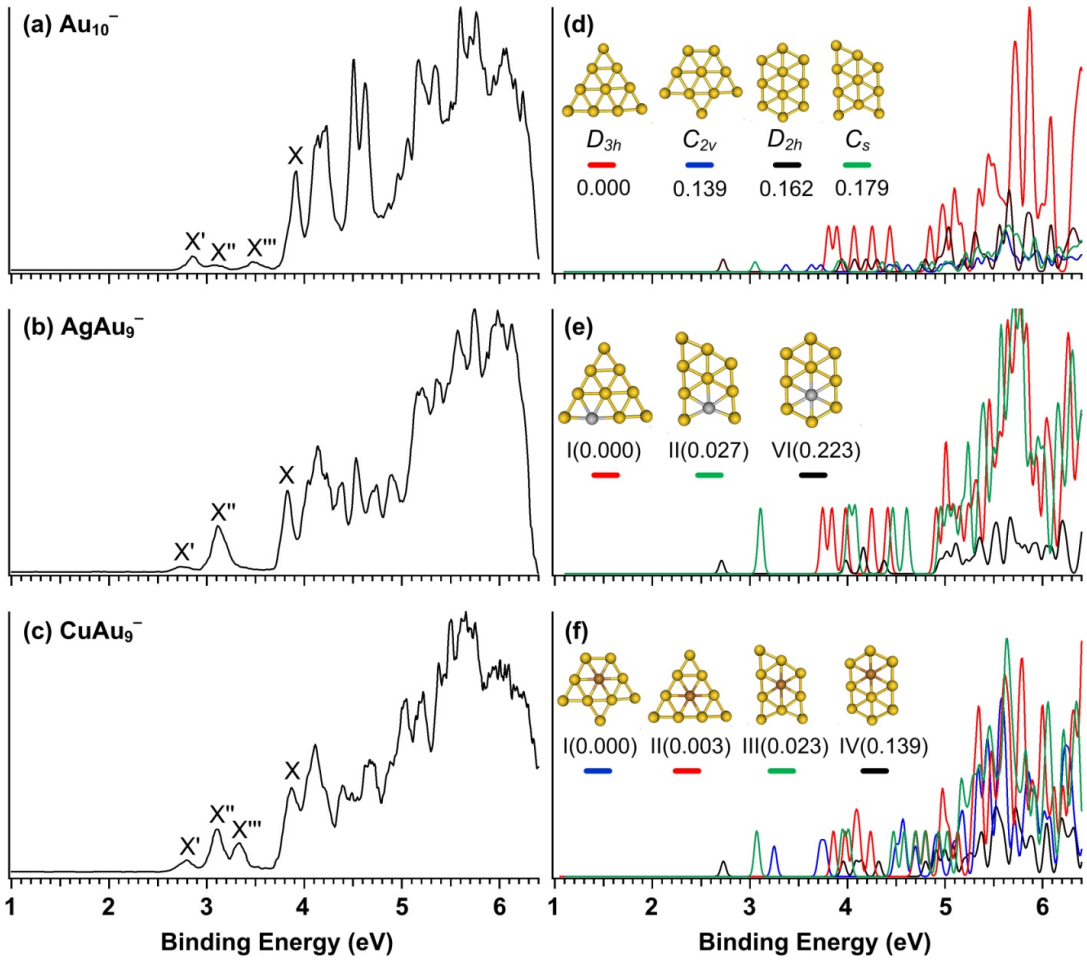

Figure 3.2 Experimental (left, a-c) and simulated (right, d-f) photoelectron spectra of Au_{10}^-, $AgAu_9^-$ and $CuAu_9^-$. The insets show the corresponding structures. The atoms are shown in colors as: Au (yellow); Ag (gray); Cu (brown).

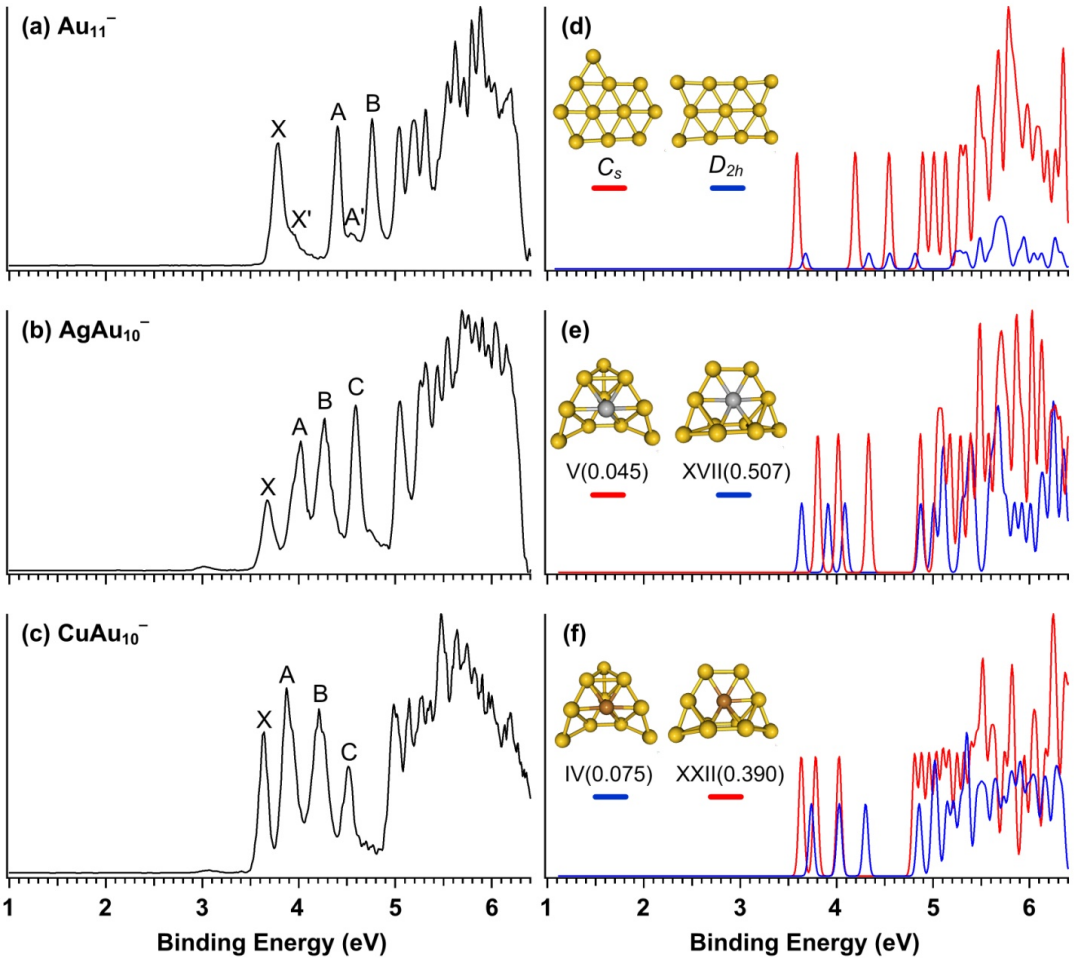

Figure 3.3 Experimental (left, a-c) and simulated (right, d-f) photoelectron spectra of Au_{11}^-, $AgAu_{10}^-$ and $CuAu_{10}^-$. The insets show the corresponding structures. The atoms are shown in colors as: Au (yellow); Ag (gray); Cu (brown).

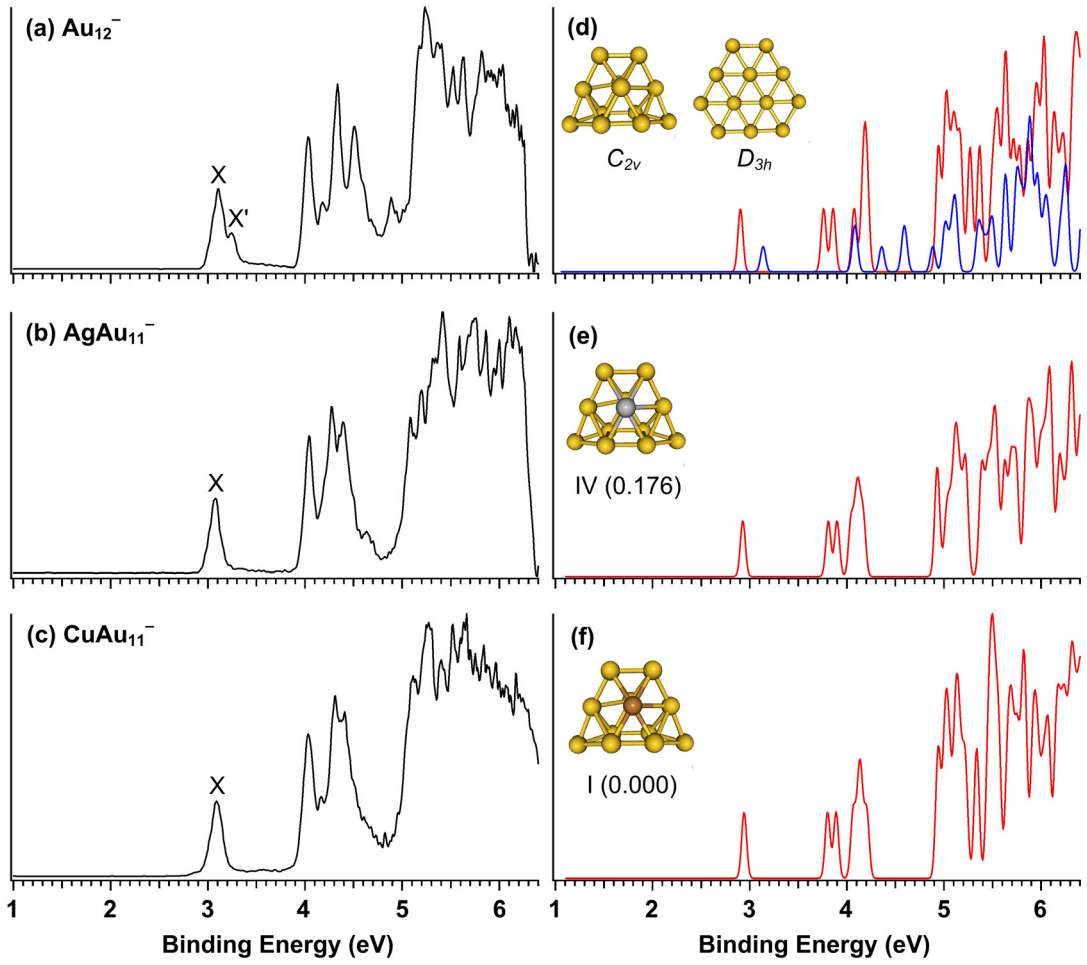

Figure 3.4 Experimental (left, a-c) and simulated (right, d-f) photoelectron spectra of Au_{12}^-, $AgAu_{11}^-$ and $CuAu_{11}^-$. The insets show the corresponding structures. The atoms are shown in colors as: Au (yellow); Ag (gray); Cu (brown).

Table 3.1 Experimental and calculated (PBE0/CRENBL) vertical detachment energies (VDE) of MAu_n^- and Au_{n+1}^- clusters (for the major isomer if there are multiple isomers) (M = Ag, Cu, n = 8–11).

n	Species	VDE (eV)	
		Exp.[a]	Cal.
	Au_9^-	3.83 (2)	3.64
8	$AgAu_8^-$	3.75 (5)	3.58
	$CuAu_8^-$	3.89 (5)	3.74
	Au_{10}^-	3.91 (2)	3.80
9	$AgAu_9^-$	3.11 (3)	3.10
	$CuAu_9^-$	3.10 (5)	3.07
	Au_{11}^-	3.80 (2)	3.59
10	$AgAu_{10}^-$	3.67 (3)	3.64
	$CuAu_{10}^-$	3.64 (5)	3.63
	Au_{12}^-	3.06 (2)	2.89
11	$AgAu_{11}^-$	3.08 (4)	2.93
	$CuAu_{11}^-$	3.09 (5)	2.94

[a] Numbers in parentheses represent the uncertainty in the last digits.

some of the detachment bands (particularly A and B) in the spectra of $AgAu_{10}^-$ and $CuAu_{10}^-$ are apparently broader than others and seem to contain fine structures (Figure 3.3b, c). This could be due to either overlap of multiple detachment transitions, or contributions from different isomers, which at this point we cannot distinguish.

MAu_{11}^-. For pure gold clusters, Au_{12}^- is the critical size for the 2D-3D structural transition, where isomers of both dimensionalities have been observed to be present in the cluster beam.[13,15] The PES spectrum of Au_{12}^- (Figure 3.4a) shows doublet features at its first band (X and X'), the major peak X was shown to be contributed by a 3D structure, while the small peak on the shoulder (X') was attributed to a planar minor isomer[15,121] Intriguingly, the spectra of $AgAu_{11}^-$ and $CuAu_{11}^-$ are very similar to that of the Au_{12}^- in terms of both spectral patterns and the peak positions, except that the weak features associated with the 2D isomer in Au_{12}^- are no longer seen in the spectra of the MAu_{11}^- (Figure 3.4). This indicates that: (1) for the doped clusters, 3D structures are overwhelmingly dominant over 2D, only 3D structures are presented in the experimental beam of MAu_{11}^-; (2) $AgAu_{11}^-$ and $CuAu_{11}^-$ should have similar 3D structures as that Au_{12}^-.

3.2.3. Theoretical Results and Discussion

Our collaborators performed global minimum search for structures of MAu_n^- (n = 8 – 11; M = Ag, Cu) (and also for Au_{10}^-) using the basin-hopping (BH) global optimization algorithm coupled with density functional theory geometry optimization,[148-149] within the generalized gradient approximation (GGA) in the Perdew-Burke-Ernzerhof (PBE) functional form,[150] using the DMol program.[149] A few to a few tens of top ranking

low energy structures of each species were selected and reevaluated at PBE0/CRENBL DFT level including spin-orbital (SO) coupling effect,[151] as implemented in the NWChem 5.1.1 program.[152] The simulated PES spectra were then used to compare with the experiment to identify the structures of MAu_n^- clusters.

MAu_8^- and Au_9^-. In previous studies,[13,15] Au_9^- has been shown to have a C_{2v} structure, which is a triangle with one missing apex, as depicted in Figure 3.1d. Our current results confirmed this structure and its simulated photoelectron spectrum agrees excellently with the experiment in which the characteristic doublet peaks and the following energy gap are well reproduced (Figure 3.1). As discussed above, our experimental observations suggest that MAu_n^- should have similar structures as Au_9^- by simple atom substitution. Apparently, there are five different sites for substitution in the C_{2v} structure of Au_9^- (Figure 3.1d), which may results in close-lying isomers for the doped clusters MAu_n^-. Indeed, our global minimum searches revealed that the lowest energy structure of $AgAu_8^-$ is similar to that of Au_9^- in which an Au atom on edge site was replaced by an Ag (structure I, Figure 3.1e). Its simulated spectrum agrees excellently with the experimental one. A center-substituted structure (II, Figure 3.1e) was found to be the second lowest-lying isomer only 0.056 eV above the global minimum, and its simulated spectrum indeed very well reproduced the weak feature X', in perfect agreement with the experiment. For $CuAu_8^-$, the center-substituted structure with C_{2v} symmetry (I, Figure 3.1f) was found to be the lowest energy, while the edge-substituted one (II, Figure 3.1f) becomes the low-lying isomer with 0.051 eV higher in energy. So the relative stability of the two structures is reversed in $CuAu_8^-$ as compared to $AgAu_8^-$, and Cu atom seems to prefer the center site while the Ag favors the open site like the

edge. This again is in quantitative match with the experiment, where the relatively closer doublet peaks (X and A) observed in the spectrum of $CuAu_8^-$ (relative to that of $AgAu_8^-$) are shown to be due to the global minimum structure I, while small population of isomer II accounts well for the weak feature X' at the low binding energy side (Figure 3.1f). We note that substitution on the edge site may result in slight local structural relaxation. Specifically, for $AgAu_8^-$, Ag atom is slightly popped outward (I, Figure 3.1e), while in $CuAu_8^-$ the Cu atom is apparently shrunk inward (II, Figure 3.1f). This is likely due to the smaller atomic radius of Cu than that of Ag.

MAu_9^- and Au_{10}^-. It has been shown that there are multiple isomers presented in the cluster beam of Au_{10}^-. The isomer issue of Au_{10}^- has recently been studied in detail by one of our groups using Ar-tagging and O_2 titration, which confirmed that at least four isomers were present.[147] It showed that the dominant isomer of Au_{10}^- is a D_{3h} triangular structure which has very high electron affinity and accounts for the major spectral features observed in its PES spectrum, while two of the low-binding-energy weak peaks (X', X'') were tentatively assigned to two low-lying isomers according to previous calculations,[15] and one (X''') remained unidentified. In the current study, we did extensive basin-hopping searches for the structure of Au_{10}^-. Four low-lying isomer structures were found within 0.2 eV, which are displayed in Figure 3.2d. Our search confirmed that the global minimum of Au_{10}^- is the D_{3h} triangular structure, whose simulated spectrum agrees well with the major spectral features in the experiment. The high electron affinity of the D_{3h} isomer is due to the open shell nature of its neutral, as explained by Hakkinen[153] recently using a 2D shell model developed by Lievens *et al*.[154] We assign the lowest binding energy peak (X') to the third isomer (0.162 eV) from our

search which is a D_{2h} structure (Figure 3.2d), consistent with our previous studies.[147] The second peak X'' has been tentatively assigned to a C_{2h} isomer before.[147] However, during our search we found a C_s structure (Figure 3.2d) which is lower in energy than the C_{2h} isomer by 0.17 eV, its first VDE agrees well with the X'' band. So we believe that feature X'' should be due to the C_s isomer, as will be shown below, this structure is also reproduced in the doped clusters. Finally, the previously unidentified X''' is assigned to a C_{2v} structure as shown in Figure 3.2d. It is the second low-lying isomer (0.139 eV) according to the search, and it can be viewed as reconstructed from the global minimum D_{3h} by moving one apex atom to the bottom.

Our theoretical results confirmed that the doped clusters MAu_9^- have similar isomer structures as Au_{10}^-. For $AgAu_9^-$, the two lowest-lying isomers (I, II) we got can be viewed as derived from the D_{3h} and C_s structures of Au_{10}^-, respectively, by substitution of an Au atom with a Ag, both at an edge site (Figure 3.2e). These two isomers are nearly degenerate in energy (0.027 eV for II), thus both are expected to have substantial populations in the beam, consistent with the experiment. The isomer II gives rise to the low binding energy peak X", while the high binding energy parts of the spectrum are contributed by the mixture of two. Similar to Au_{10}^-, the feature X' is assigned to the D_{2h}-derived structure (Figure 3.2e), which is the VI low-lying isomer, 0.223 eV above structure I. Though during the search other structures are found lower in energy than VI, they don't agree with experiment thus can be ruled out. The relatively high energy of structure VI is consistent with its small population in the experiment. For the Cu doping, the four low-lying isomer structures of Au_{10}^- are all reproduced in $CuAu_9^-$ as the top four lowest energy isomers. As shown in Figure 3.2f, the first three isomers (I, II, III) of

$CuAu_9^-$, corresponding to the C_{2v}, D_{3h}, C_s isomers of Au_{10}^- respectively, are also very close in energy, and superposition of their simulated spectra assuming nearly equal contribution acquires good agreement with the experiment. The isomer IV (0.139 eV) is assigned to X', similar to the case of Au_{10}^- and $AgAu_9^-$. Overall, despite the very complicated spectra, by combining the global minimum search and the comparison study of pure and doped clusters, we are able to identify all the isomers for Au_{10}^- and MAu_9^-. The isoelectronic substitution in fact offers a new way to recognize and identify minor isomers in the experiment. Note again that in the doped clusters MAu_9^-, the Ag atom tends to occupy the edge site, while Cu atom favors the center place. But neither of the dopant atoms seems to prefer the low-coordination apex site (Figure 3.2e, f).

MAu_{10}^- and Au_{11}^-. The global minimum of Au_{11}^- has been shown to have a C_s structure, which can be viewed as built from the D_{2h} isomer of Au_{10}^- by one more Au atom bridging at one edge (Figure 3.3d).[13,15] Our current work confirmed this result. As shown in Figure 3.3d, the simulated spectrum of this C_s structure agrees perfectly with the experimental spectrum of Au_{11}^-. In addition, a D_{2h} structure is identified as a minor isomer which gives rise to the weak features X' and A' observed in the experiment (Figure 3.3a, d).

For MAu_{10}^-, we carried out very extensive searches by starting from several randomly built initial structures. In addition, we considered every possible substitution site in the global minimum structure of Au_{11}^-. The obtained lowest twenty and twenty eight structures, respectively for $AgAu_{10}^-$ and $CuAu_{10}^-$, are sorted out in Figures 3.5 and 3.6, along with their simulated spectra. For $AgAu_{10}^-$, the first few low-lying isomers seem dominant by 2D structures (Figures 3.5), which all can be viewed as derived from

the C_s structure of Au_{11}^- (Figure 3.3d) by Ag-atom substitution. Except that one 3D isomer (V, Figure 3.5 is found to be competitive in energy (0.045 eV). For $CuAu_{10}^-$, the two lowest structures (I, II, Figure 3.6) obtained from our search are all 3D. A center-substituted 2D structure (III) and another 3D structure (IV) are found to be very close in energy to the global minimum one (Figure 3.6). Nevertheless, as can be seen from Figures 3.5 and 3.6, none of the simulated spectra for a single structure can produce a pattern that agrees with the experiment for either $AgAu_{10}^-$ or $CuAu_{10}^-$. This is consistent with the experimental observation that spectra of $AgAu_{10}^-$ and $CuAu_{10}^-$ might contain contributions from multiple isomers. According to our experimental results discussed above, the broad nature of bands A and B (Figure 3.3b) suggests that they could be due to overlap of multiple peaks. Among the extensive structures of $AgAu_{10}^-$, the best agreement with experiment was obtained by mixture of two 3D isomers, structure V and XVII (Figure 3.3e). The isomer V is only 0.045 eV, and can viewed as degenerate with the global minimum within the uncertainties of DFT energies. While structure XVII is a high energy isomer (0.507 eV according to our calculation). The isomer XVII is similar to the structure of $AgAu_{11}^-$, as will be shown in the next part, which is reasonable since the structures should have a smooth evolution when growing from the smaller clusters to the larger ones. Two similar structures as those of $AgAu_{10}^-$ are assigned to $CuAu_{10}^-$ (IV and XXII, Figure 3.3f). Again while structure IV (0.075 eV) is competing with the global minimum, the isomer XXII is a high-lying structure (0.390 eV). It is known that DFT energies calculated for gold clusters around the 2D-3D transition point usually show large uncertainties.[120] That is possibly one reason that the isomer XVII of $AgAu_{10}^-$ and the isomer XXII of $CuAu_{10}^-$ were observed in the experiment, thought calculated to be high

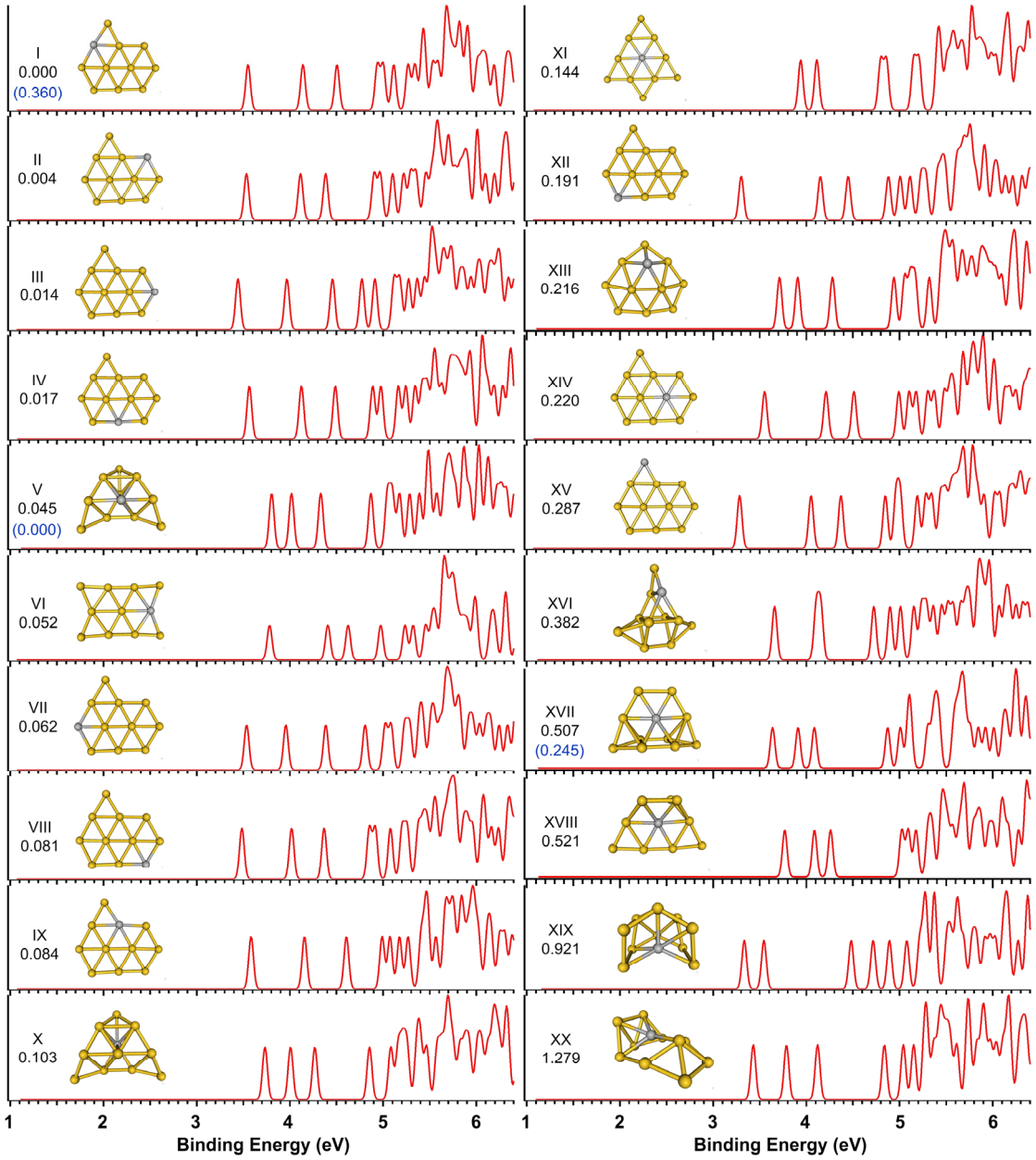

Figure 3.5 The simulated photoelectron spectra of the twenty low-lying isomers of $AgAu_{10}^-$. The insets show the structures and relative energies. The values in the parenthesis (marked blue) are the relative energies calculated at M06-L level.

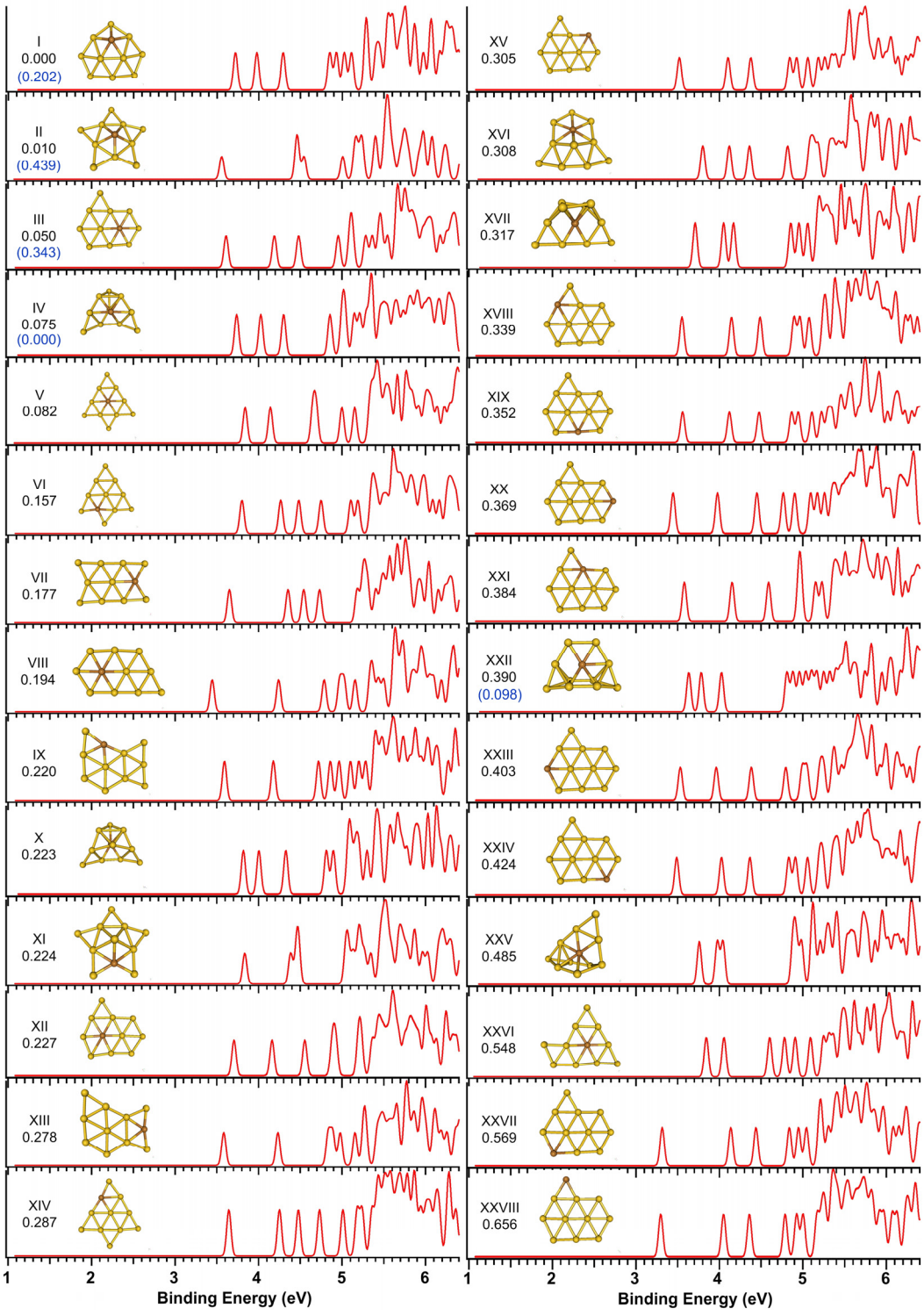

Figure 3.6 The simulated photoelectron spectra of the twenty eight low-lying isomers of $CuAu_{10}^-$. The insets show the structures and relative energies. The values in the parenthesis (marked blue) are the relative energies calculated at M06-L level.

in energies. Two recent theoretical works suggest that M06-L functionals can correctly predict the relative energies for gold clusters.[155-156] So we recalculated single point energies of the two assigned structures, as well as a few lowest isomers of MAu_{10}^- at M06-L/CRENBL level of theory. The two assigned structures for both $AgAu_{10}^-$ (V & XVII) and $CuAu_{10}^-$ (IV & XXII) indeed turn out to be the two lowest energy isomers (among those checked) at this level (see Figures 3.5 & 3.6). In any case, our experimental data and theoretical search suggest that, in contrast to the planar Au_{11}^-, 3D structures are significantly populated for MAu_{10}^-. The different atomic properties of Ag/Cu as compared to Au somehow induce "chemical perturbations" to the doped clusters, which results in an earlier 2D-3D structural transition for $AgAu_{11}^-$ and $CuAu_{10}^-$, as compared with the parent gold cluster.

MAu_{11}^- and Au_{12}^-. So far, it has been conclusive that Au_{12}^- is the dimension crossover point where the 2D-3D transition occurs for gold cluster anions. Though initially there has been controversial between experiment and theory about the critical size for 2D-3D transition,[13,15] two recently work reaffirmed unequivocally the coexistence of both 2D and 3D isomers in the beam of Au_{12}^-, using combined trapped ion electron diffraction and the state-of-the-art DFT calculations,[120] and Ar-tagging photoelectron spectroscopy,[121] respectively. Particularly in the later work, 2D/3D isomer-specific photoelectron spectrum of Au_{12}^- has been obtained. So here we will only briefly present our new simulations. As shown in Figure 3.4d, the 3D and 2D structures of Au_{12}^- are of C_{2v} and D_{3h} symmetry, respectively. The simulated spectra by overlap of both isomers with 3D/2D ratio ~ 3/1, as suggested by the experimental data, are in good agreement with the experiment. We would like to point out that, for open shell species

like Au_{12}^-, photodetachment would result in a final neutral state which could be of either triplet or singlet spin coupling, as has been discussed in section 1.3.4. Such singlet-triplet splitting can not be quantitatively reproduced in the simulated density of states. Thus the agreement between experiment and the simulation for these open shell clusters is usually not as prefect as that of closed shell ones. However, the overall agreement between the experimental and simulated spectra of Au_{12}^- is satisfactory (Figure 3.4), confirming the 2D and 3D structures assigned. We also would like to mention that though the experimental data suggests that the 3D structure (C_{2v}) should be the global minimum for Au_{12}^-, our calculation gives the result that it is 0.414 eV above the 2D (D_{3h}). This is consistent with the conclusion from previous studies[15,120] that DFT methods using traditional generalized gradient functionals are heavily biased towards 2D structures. Again we rechecked the relative energies of the C_{2v} and the D_{3h} using M06-L functional, it shows that the 3D structure (C_{2v}) is indeed more stable than the 2D (D_{3h}) by 0.276 eV, in excellent agreement with the experiment.

For $AgAu_{11}^-$ and $CuAu_{11}^-$, our calculations confirmed that only the 3D structure is present, which is consistent with our proposal that the 2D-3D transition happens at MAu_{10}^-. $AgAu_{11}^-$ and $CuAu_{11}^-$ have similar structures, which is also similar to the C_{2v} isomer of Au_{12}^- but with one Au atom at a six-coordination site replaced by the Ag or Cu atom (Figure 3.4e, f), consistent with the experimental observations. For $AgAu_{11}^-$, this is isomer IV, 0.176 eV above the lowest energy structure, but the later can be ruled out because its simulation does not agree with the experiment. For $CuAu_{11}^-$, it is the lowest energy structure among our searched isomers.

3.2.4. Conclusions

In summary, we presented a joint PES and DFT studies on a series of isoelectronically doped gold clusters, MAu_n^- (n = 8 –11, M = Ag, Cu). Comparison between the spectra of the doped clusters and the corresponding pure gold clusters at same sizes, aided by high level DFT calculations, allow us to gain insight into the structural characteristic of those bimetallic species. As expected, generally the photoelectron spectra of the doped clusters MAu_n^- were found to be very similar to those of the corresponding pure gold cluster Au_{n+1}^-, indicating that substitution of an Au atom by an Ag/Cu atom does not significantly alter the geometric and electronic structures of the parent clusters. The only exception is for n = 10, where very different spectra were observed between MAu_{10}^- and Au_{11}^-, suggesting substantial structural changes upon doping at this size. Our theoretical results confirmed experimental observations. In short, for n = 8 and 9, MAu_n^- possess very similar isomeric structures as those of Au_9^- and Au_{10}^- in which Ag or Cu simply substitutes one Au atom. For n = 10, while the pure gold cluster Au_{11}^- is planar, the doped clusters MAu_{10}^- are dominant with 3D structures. Finally, only 3D structures are observed for MAu_{11}^-, in contrast to the 2D/3D structural coexistence for Au_{12}^-. Our work demonstrated that the isoelectronic substitution in the doped clusters induces an earlier onset (by one atom in size) for 3D structures as compared to the parent pure gold cluster anions.

3.3. MAu_x^- Clusters (M = Si, Ge and Sn; x = 5–8)

3.3.1. Introduction

Group-14 atoms Si, Ge and Sn are strongly covalent elements and their compounds with gold are usually characterized by strong covalent M-Au bonding.[157-158] Such strong covalent bonding would be expected to distort the overall structures of small gold clusters upon doping with a group-14 atom. Particularly for Si, it has strong sp^3 hybridization, thus tends to form tetrahedral boning with other ligand atoms. It indeed has been reported that the small Si-doped gold clusters are not planar, and their structures are dominated by Si dopant.[127,159-161] Particularly, one of our previous studies shows that Au behaves like a hydrogen atom in the $SiAu_4$ cluster, in that both the tetrahedral structure of $SiAu_4$ and its chemical bonding resemble that of the silane molecule (SiH_4).[127] This intriguing Au/H analogy was later confirmed and extended in other small Si-doped gold clusters.[160-161] Those clusters should rather be viewed as molecular-like speices. However, recent *ab initio* computations suggested that such Au/H analogy does not exist in $GeAu_4$ and $SnAu_4$, and these two clusters exhibit square-pyramidal C_{4v} structures, rather than the T_d structure of $SiAu_4$.[162] This is likely due to the fact that the sp^3 hybridization for Ge and Sn is not as strong as that in Si. As the size of gold clusters increases, it might be expected that the effect of a dopant atom on the overall structure of doped gold clusters diminishes. A recently DFT study suggested that the local tetrahedral structure motif around Si dopant does not exist any more for $SiAu_x$ clusters larger than $SiAu_5$, and $SiAu_6$ – $SiAu_8$ clusters have quasi-planar structures.[163]

In this subsection, we explore structural evolution of Si, Ge and Sn doped anion Au clusters, MAu_x^- (M = Si, Ge, Sn), in the size range of x = 5–8.[164] We focus on (1) the

structural evolution and the interplay between molecule-like behavior around the group-14 dopant (e.g. local T_d $SiAu_4$ unit) and the tendency to retain overall structural integrity of the gold clusters with increasing cluster size, and (2) how the chemical similarity and/or difference among Si, Ge and Sn dopant affect the growth pattern of Si, Ge and Sn-doped Au clusters.

3.3.2. Experimental Results

Since the group-14 atoms are very easy to cluster, the dopant content in the targets were carefully adjusted (~ 2% Si, 2% Ge and 2.5% Sn, respectively) to minimize the multi-atom doping so as to achieve clean mass selection of MAu_{5-8}^-. The measured photoelectron spectra of MAu_{5-8}^- (M = Si, Ge, Sn) at 193 nm are displayed in Figures 3.7–3.10, respectively, along with the simulated spectra for comparison. The first VDEs of each species are summarized and compared to the calculated values in Tables 3.2–3.5, respectively.

MAu_5^-. As seen in Figure 3.7, the spectrum of $SiAu_5^-$ is relatively simple with four apparent features (Figure 3.7a). The X band is sharp and intense, which defines an accurate VDE of 4.21 eV. The A and B bands are rather broad with some unresolved features, suggesting that they likely contain multiple electronic transitions. We note that the patterns of the broad features A and B in the spectrum of $SiAu_5^-$ are similar to the corresponding parts in the spectrum of $SiAu_4^-$,[127] suggesting that its electronic structure is not significantly altered relative to $SiAu_4^-$. Hence it is possible that their geometrical structures also do not differ too much and the tetrahedral $SiAu_4$ unit [127] may be retained in $SiAu_5^-$. It was shown previously that $SiAu_4$ is closed shell with a very large HOMO-

LUMO gap. In $SiAu_4^-$, the extra electron occupies the delocalized LUMO orbital of $SiAu_4$, giving rise to a very low binding energy peak (X) in its PES spectrum.[127] In contrast, the first band (X) in $SiAu_5^-$ is at much higher binding energy than that of $SiAu_4^-$, suggesting that it is likely originated from the extra Au atom.

The spectra of $GeAu_5^-$ and $SnAu_5^-$ are very similar (Figure 3.7b, c), both featuring two closely spaced peaks at ~ 3.5 – 4 eV (X and A) followed by a sizable energy gap and several well-resolved peaks. The first VDE of $GeAu_5^-$ and $SnAu_5^-$ are measured to be 3.68 eV and 3.58 eV, respectively, notably smaller than that of $SiAu_5^-$ (Table 3.2). The clear similarities in their PES spectra suggest that $GeAu_5^-$ and $SnAu_5^-$ should have similar structures. However, there are some weak features observed in the spectrum of $SnAu_5^-$ at the low binding energy part below ~ 3.5 eV (Figure 3.7c), suggesting possible isomers or impurities in the $SnAu_5^-$ cluster beam.

MAu_6^-. As shown in Figure 3.8a–c, the overall spectral patterns are similar among the three doped clusters MAu_6^- (M = Si, Ge, Sn), each displaying three peaks in the low binding energy region (< ~ 4 eV) with a fairly large HOMO-LUMO gap (X–A separation): 0.97, 0.93 and 0.95 eV for M = Si, Ge and Sn, respectively. The first VDE measured for MAu_6^- are 2.70, 2.65, and 2.57 eV for M = Si, Ge, and Sn, respectively, quite close to each other. The similar doublet features A and B in the spectra of MAu_6^- are likely due to the detachment transitions to the first triplet and singlet excited states of the neutrals, judging by their relative intensities. Since the MAu_6^- anion clusters are open shell with one unpaired electron and detaching one electron from an orbital other than its SOMO (the X band) will result in an excited state of the neutral which could be of either a singlet or a triplet spin arrangement. The higher intensity A band represents the

detachment transition to the lowest triplet excited state of the neutral MAu_6 species, and B the corresponding singlet state. The triplet-singlet splitting (A–B separation) is nearly identical in the three spectra of MAu_6^-: 0.30, 0.32 and 0.30 eV for M = Si, Ge and Sn, respectively. The spectral similarities as well as their close VDEs, HOMO-LUMO gaps and possible triplet-singlet splitting suggest that major isomers of MAu_6^- may have similar structures. Again, some weak features are observed in the spectra of $GeAu_6^-$ (X' in Figure 3.8b) and $SnAu_6^-$ (X' and X" in Figure 3.8c), indicating presence of minor isomers.

MAu_7^-. The spectra of MAu_7^- (Figure 3.9a–c) are also quite similar to each other, each revealing four well-resolved peaks in the region between 3 – 5 eV followed by more congested bands in the higher binding energy side. The intense and sharp ground state transition (X) suggests that the MAu_7^- anions are closed shell and there is negligible geometrical change between the anion and the neutral. The binding energies of bands X, A and C and the overall spectral patterns are very similar for the three MAu_7^- clusters, and even the features beyond 5 eV are also comparable, suggesting that the three clusters should have similar structures. The only major difference among the three spectra is that the binding energy of the B band in the spectrum of $SiAu_7^-$ is much lower as compared to that of $GeAu_7^-$ and $SnAu_7^-$ (Figure 3.9), suggesting that it is likely due to detachment from a dopant-dominated molecular orbital and reflecting the chemical difference between Si and Ge/Sn in the doped clusters. It should also be noted that the spectra of all three MAu_7^-clusters seem free of weak features due to minor isomers. This implies that there must be a relatively stable structure type for the three clusters.

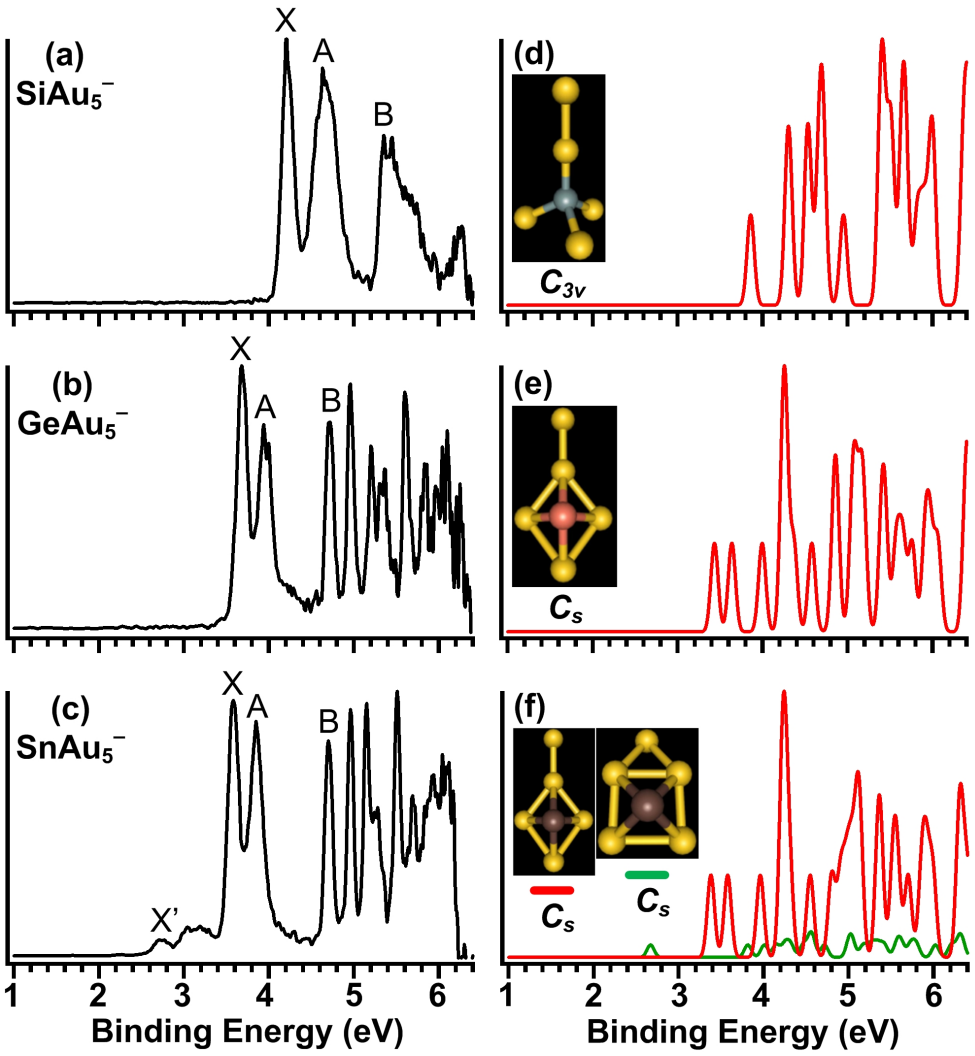

Figure 3.7 The experimental (left) and simulated (right) photoelectron spectra of MAu_5^- (M = Si, Ge, Sn). The insets show the corresponding structures. The dopant atoms are shown in color (Si in grey, Ge in red, and Sn in brown).

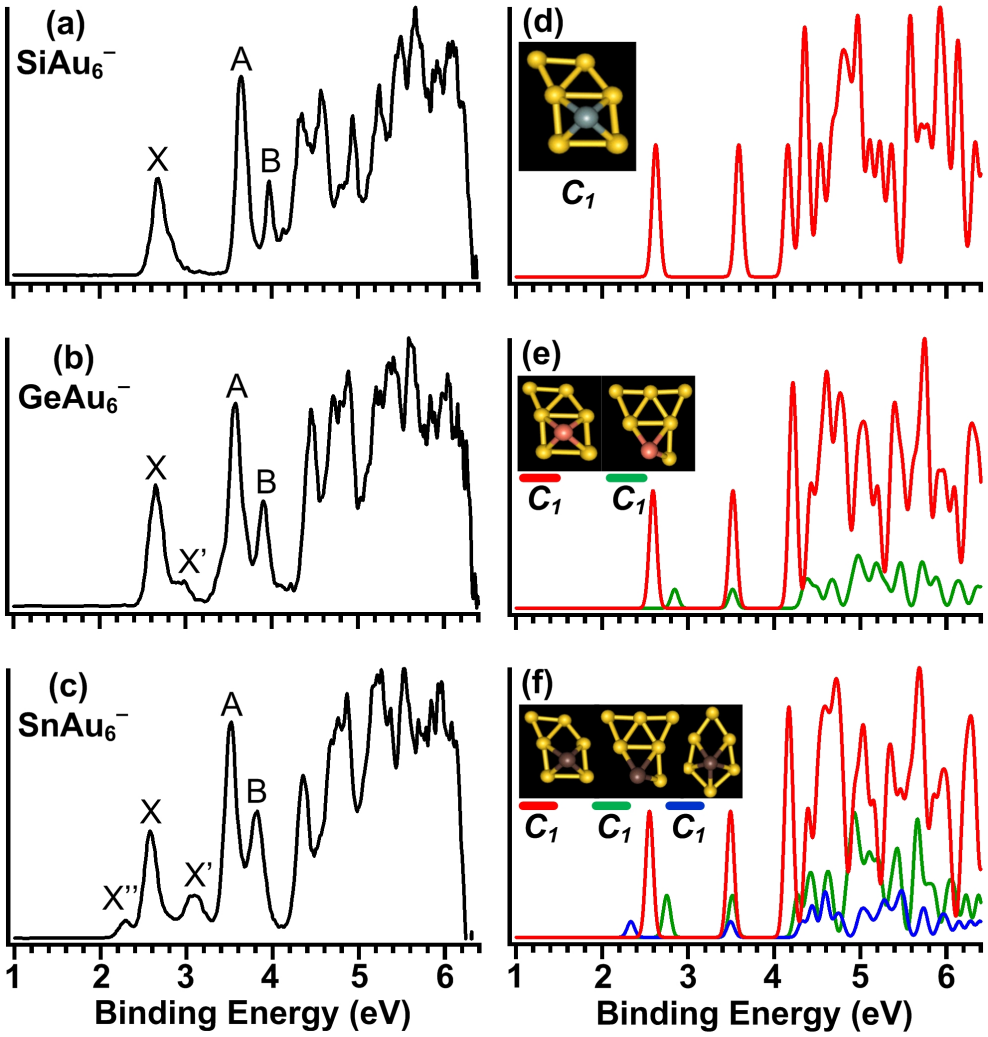

Figure 3.8 The experimental (left) and simulated (right) photoelectron spectra of MAu_6^- (M = Si, Ge, Sn). The insets show the corresponding structures. The dopant atoms are shown in color (Si in grey, Ge in red, and Sn in brown).

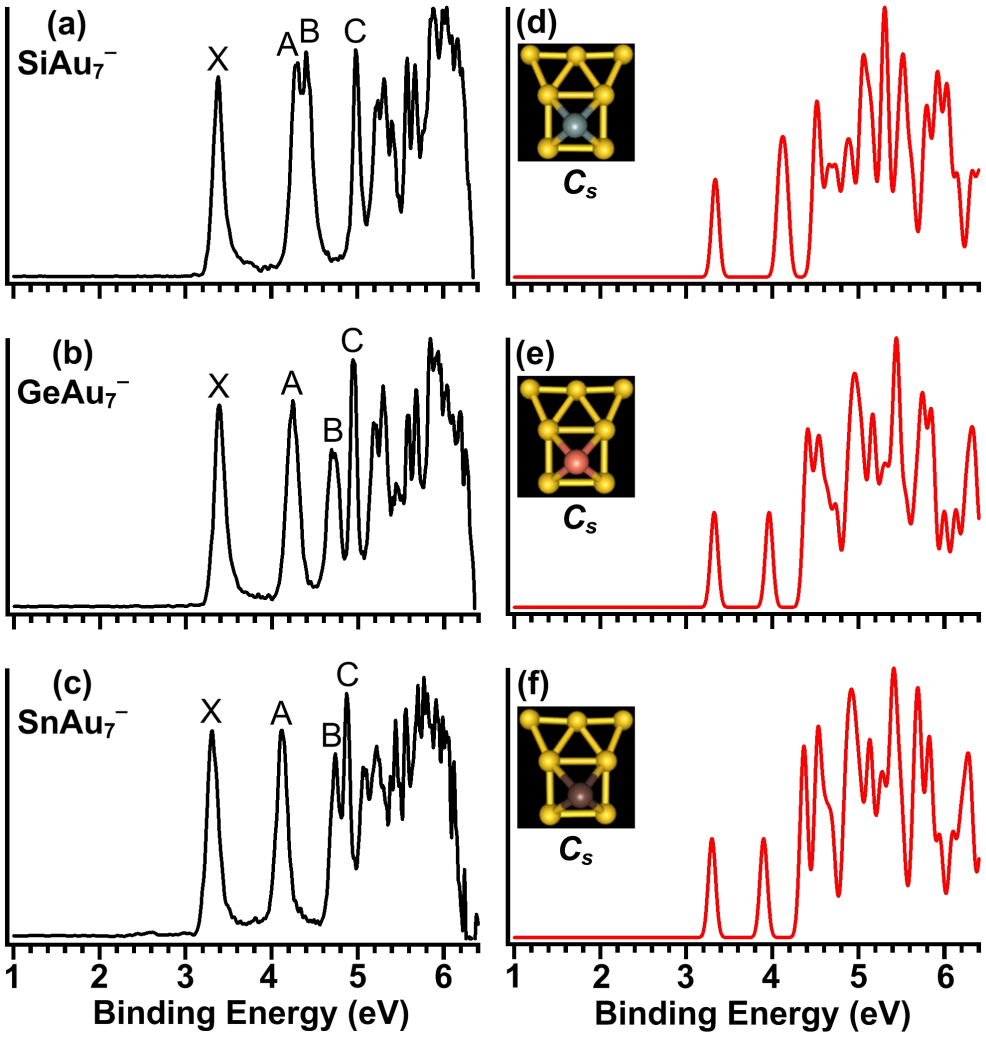

Figure 3.9 The experimental (left) and simulated (right) photoelectron spectra of MAu_7^- (M = Si, Ge, Sn). The insets show the corresponding structures. The dopant atoms are shown in color (Si in grey, Ge in red, and Sn in brown).

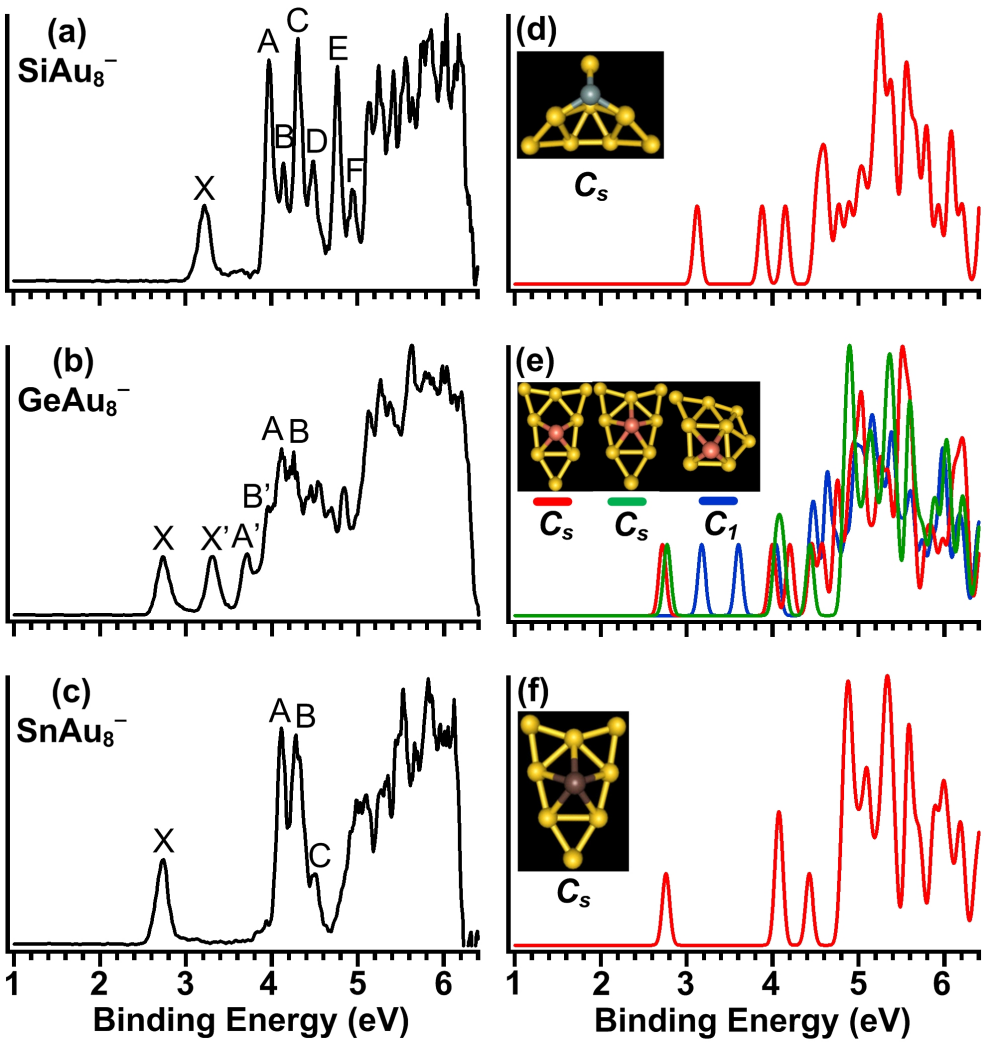

Figure 3.10 The experimental (left) and simulated (right) photoelectron spectra of MAu_8^- (M = Si, Ge, Sn). The insets show the corresponding structures. The dopant atoms are shown in color (Si in grey, Ge in red, and Sn in brown).

MAu_8^-. For MAu_8^-, the three doped clusters display dramatically different PES spectra (Figure 3.10a–c), suggesting a major structural divergence among them. For $SiAu_8^-$, the first VDE (X) is observed to be 3.23 eV. Following the X band and a HOMO-LUMO gap of 0.75 eV, three sharp excited-state-transition bands (A, C, and E, Figure 3.10a) are observed between ~ 4 – 5 eV, each followed by a weaker peak with separations of 0.15 eV (A–B), 0.17 eV (C–D) and 0.18 eV (E–F). The relative intensities of these peaks also imply that they are due to transitions to triplet and singlet final states, that is, bands A, C and E define the first, second and third triplet excited states of the neutral $SiAu_8$, while bands B, D and F represent the corresponding singlet states, respectively.

The spectrum of $GeAu_8^-$ (Figure 3.10b) is much more complicated as compared to that of $SiAu_8^-$. The X band defines a VDE of 2.73 eV, much smaller than that of $SiAu_8^-$. The energy gap between the first (X) and the second peak (X') does not look like a usual HOMO-LUMO gap, since the second band displays similar intensity as the first one. In addition, the spectral features between 4–5 eV in the spectrum of $GeAu_8^-$ are much more congested and complicated than any other species studied here, suggesting that there might be coexistence of multiple isomers with nearly equal contributions to the observed spectrum. Indeed, a closer look reveals that parts of the spectral features in $GeAu_8^-$ (X, A, B) actually are very similar to the corresponding peaks in the spectrum of $SnAu_8^-$ (Figure 3.10c), suggesting that one of the isomers observed for $GeAu_8^-$ is similar to $SnAu_8^-$. Thus bands X', A' and B' should be due to a different isomer.

The spectrum of $SnAu_8^-$ is relatively simple with a large HOMO-LUMO gap of 1.37 eV (Figure 3.10c), suggesting a high stability of neutral $SnAu_8$, and possibly also

high symmetry. The first VDE of $SnAu_8^-$ is 2.74 eV, which is very close to that of the X band in $GeAu_8^-$. The intense peak B with a shoulder (C) is again an indication of triplet-singlet splitting. The band A may also have a corresponding singlet part, which is likely buried in the intense band B.

3.3.3. Theoretical Results

As usual, our collaborators started with BH searches for low-lying isomers of MAu_{5-8}^-. A pool of low energy structures were then re-optimized at PBEPBE/SDD DFT (Gaussian03 software package[165]) level. However, due to the complexity of the clusters, another DFT method (PBE/TZP) (ADF software package[166]) as well as higher level *ab initio* calculations (including MP2, MP4 and CCSD(T)) were further carried out to evaluate the relative energy rankings of 5 lowest-lying isomers for some species to aid structural assignment. The theoretical results for the top-5 lowest energy structures of MAu_5^- – MAu_8^-, respectively, are summarized in Figures 3.11–3.14 and Tables 3.2–3.5. The isomers are ranked based on their relative energies at the PBE/TZP level except a few leading isomers which are ranked at higher level theory (see table captions).

MAu_5^-. For $SiAu_5^-$, DFT (ADF and G03), MP4(SDQ), and CCSD(T) computations all predict isomer 1 (C_{3v}) as the global minimum (Figure 3.11a), which can be viewed as a tetrahedral $SiAu_4$ bonded by another Au atom through a terminal gold atom. While the MP2 calculations seem to prefer isomer 2 as the lowest energy, which is also of C_{3v} symmetry (Figure 3.11b). Two previously reported structures of neutral $SiAu_5$[159,163] are also checked and found to be higher energy isomers for the anion $SiAu_5^-$ and disagree with the experiment. For $GeAu_5^-$, both PBE/TZT (ADF) and MP4(SDQ)

calculations locate a C_s structure (isomer 1, Figure 3.11f) to be the global minimum, while MP2 calculation suggests isomer 1 is 0.064 eV higher than isomer 2. For $SnAu_5^-$, the lowest energy structure is also the C_s structure (isomer 1, Figure 3.11k) similar to $GeAu_5^-$. The lowest energy structures (at MP4 level) of $GeAu_5^-$ and $SnAu_5^-$ can be viewed as derived from the square-pyramidal $GeAu_4$ and $SnAu_4$,[162] respectively, by attaching one more terminal Au atom. Notice that another structure related to the square-pyramidal $SnAu_4$, with one more bridging Au, is found to be 0.311 eV at PBE/TZP level and 0.21 eV at MP2 level for $SnAu_5^-$ (Figure 3.11o).

MAu_6^-. DFT calculations predict isomer 3 and isomer 2 as the global minimum for $SiAu_6^-$. They are both 3D and of C_s symmetries. Isomer 3 can be viewed as based on the tetrahedral $SiAu_4$ unit (Figure 3.12c). However, the higher level MP4 calculation reveals a C_1 structure (isomer 1, Figure 3.12a) as its ground state, which is *quasi-planar* and can be viewed as derived from isomer 3 of $SiAu_5^-$ by attaching one more bridging Au atom. For $GeAu_6^-$, all four levels of computations indicate that isomer 1 (C_1, Figure 3.12f) is the global minimum (Table 3.3). Isomer 1 of $GeAu_6^-$ is also *quasi-planar* and can be viewed as derived from the isomer 1 of $GeAu_5^-$. Isomer 2 (Figure 3.12g), which is an edge-bridged triangle with the Ge atom located at one apex, is found to be very close in energy (0.033 eV at MP4). For $SnAu_6^-$, two C_1 structures (1 & 2, Figure 3.12k, i) are found to be nearly degenerate in energy (Table 3.3). They are similar to isomer 2 and isomer 1 of $GeAu_6^-$, respectively. Another low-lying isomer 3 (C_s, Figure 3.12m), in which Sn atom is penta-coordinated, is also found close in energy to isomers 1 and 2 at DFT levels (Table 3.3). Notice that a similar structure as isomer 3 of $SnAu_6^-$ has been previously reported for $SiAu_6$,[163] but we did not find it as low-lying isomer for $SiAu_6^-$.

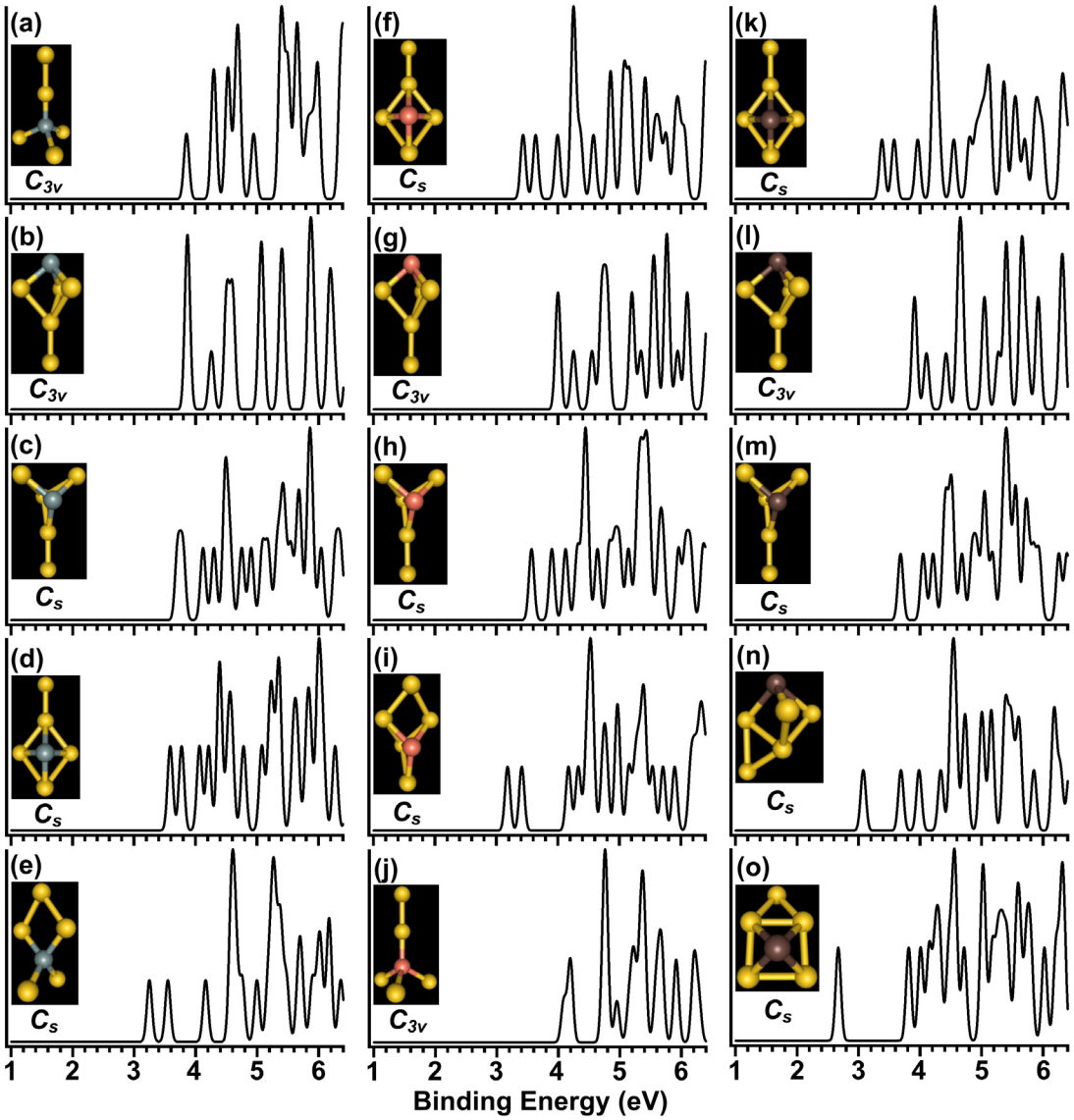

Figure 3.11 The simulated PES spectra of the top-five lowest-lying isomers of $SiAu_5^-$ (left, a – e), $GeAu_5^-$ (middle, f – j), and $SnAu_5^-$ (right, k – o). For each species, the isomers are numbered from the top to bottom (i.e. a – e, or f – j, or k – o) as isomer 1 to 5 in accordance with those in Table 3.2. The insets show the corresponding structures. The dopant atoms are shown in color (Si in grey, Ge in pink, and Sn in brown).

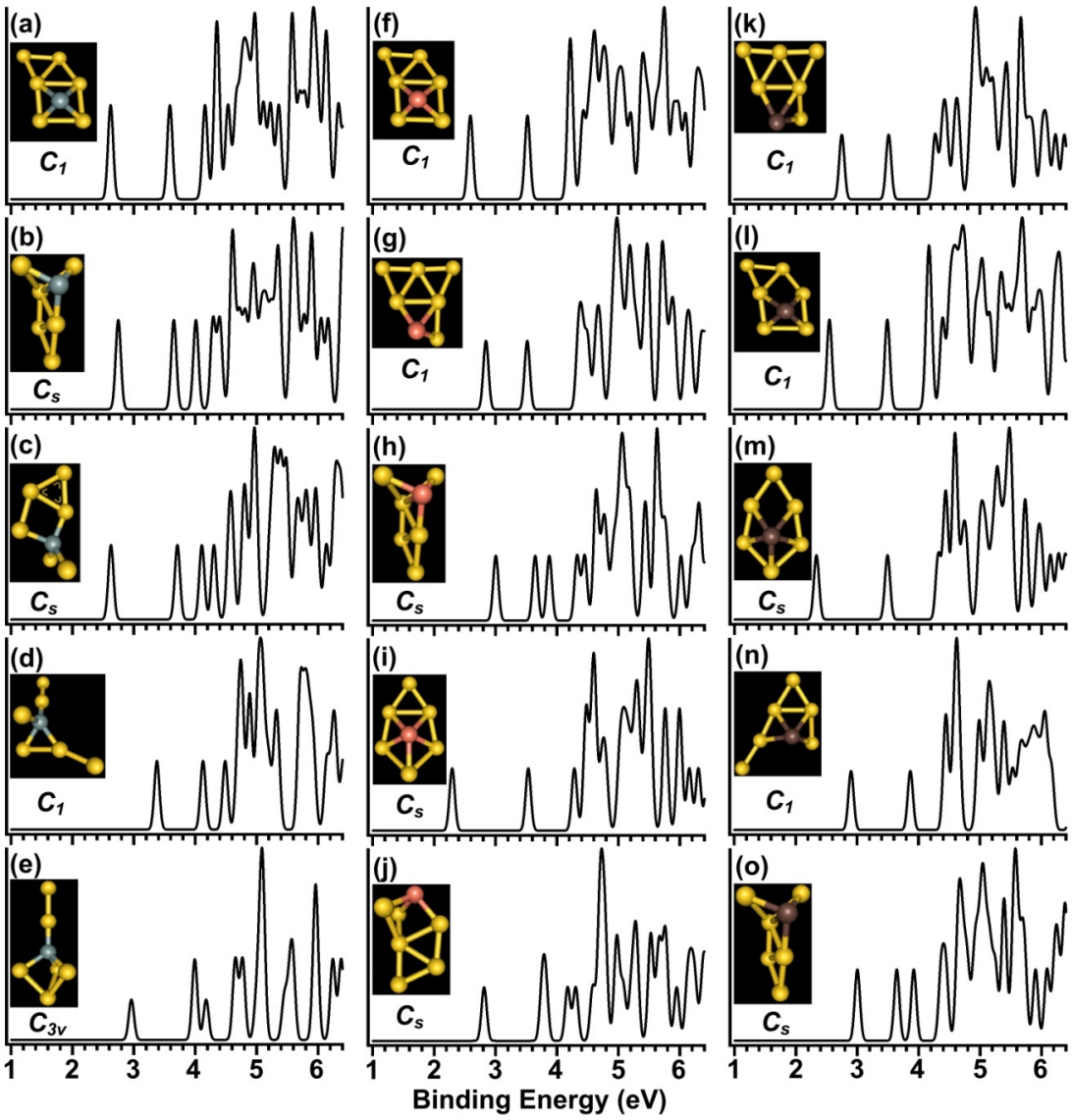

Figure 3.12 The simulated PES spectra of the top-five lowest-lying isomers of $SiAu_6^-$ (left, a – e), $GeAu_6^-$ (middle, f – j), and $SnAu_6^-$ (right, k – o). For each species, the isomers are numbered from the top to bottom (i.e. a – e, or f – j, or k – o) as isomer 1 to 5 in accordance with those in Table 3.3. The insets show the corresponding structures. The dopant atoms are shown in color (Si in grey, Ge in pink, and Sn in brown).

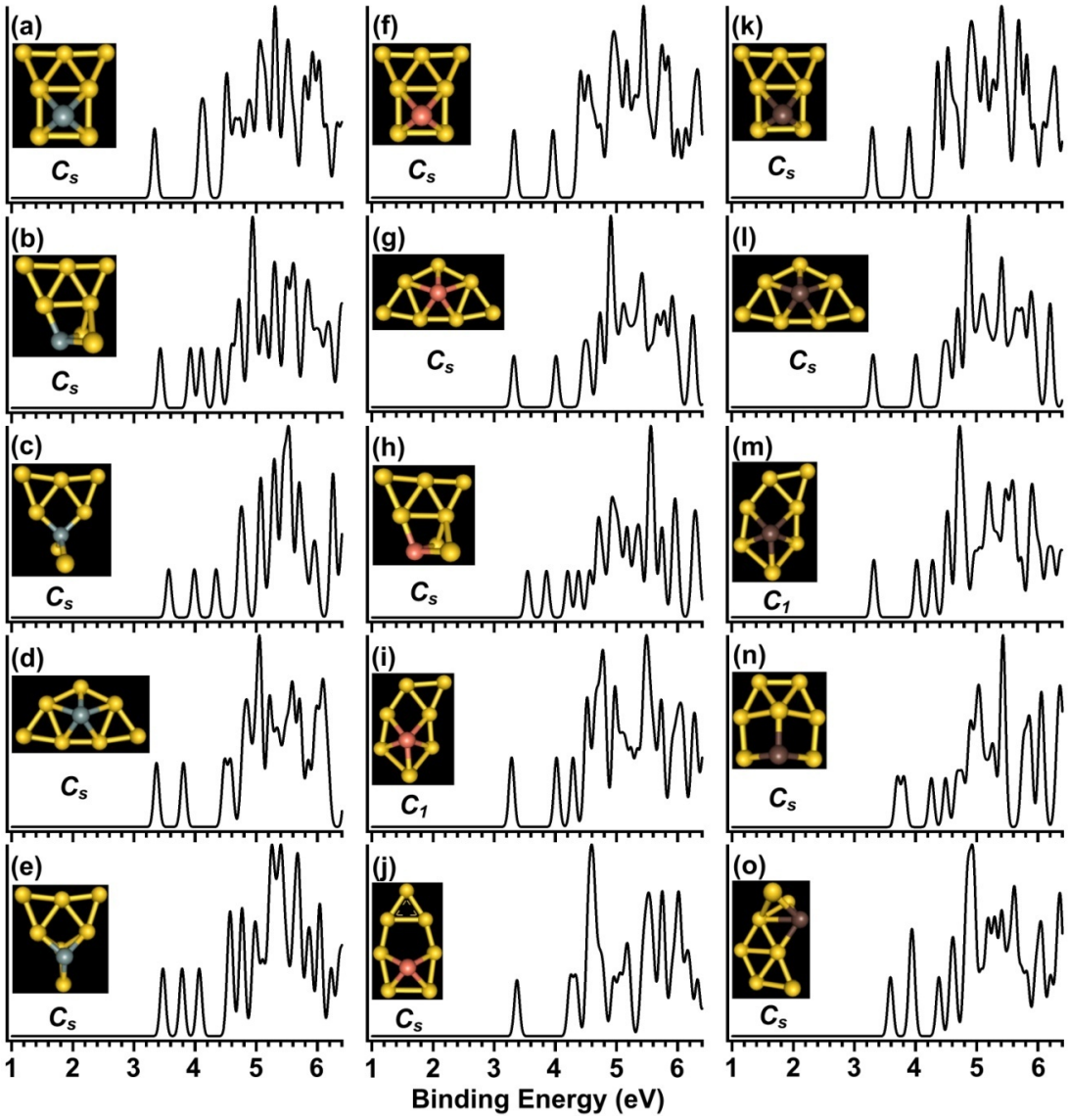

Figure 3.13 The simulated PES spectra of the top-five lowest-lying isomers of $SiAu_7^-$ (left, a – e), $GeAu_7^-$ (middle, f – j), and $SnAu_7^-$ (right, k – o). For each species, the isomers are numbered from the top to bottom (i.e. a – e, or f – j, or k – o) as isomer 1 to 5 in accordance with those in Table 3.4. The insets show the corresponding structures. The dopant atoms are shown in color (Si in grey, Ge in pink, and Sn in brown).

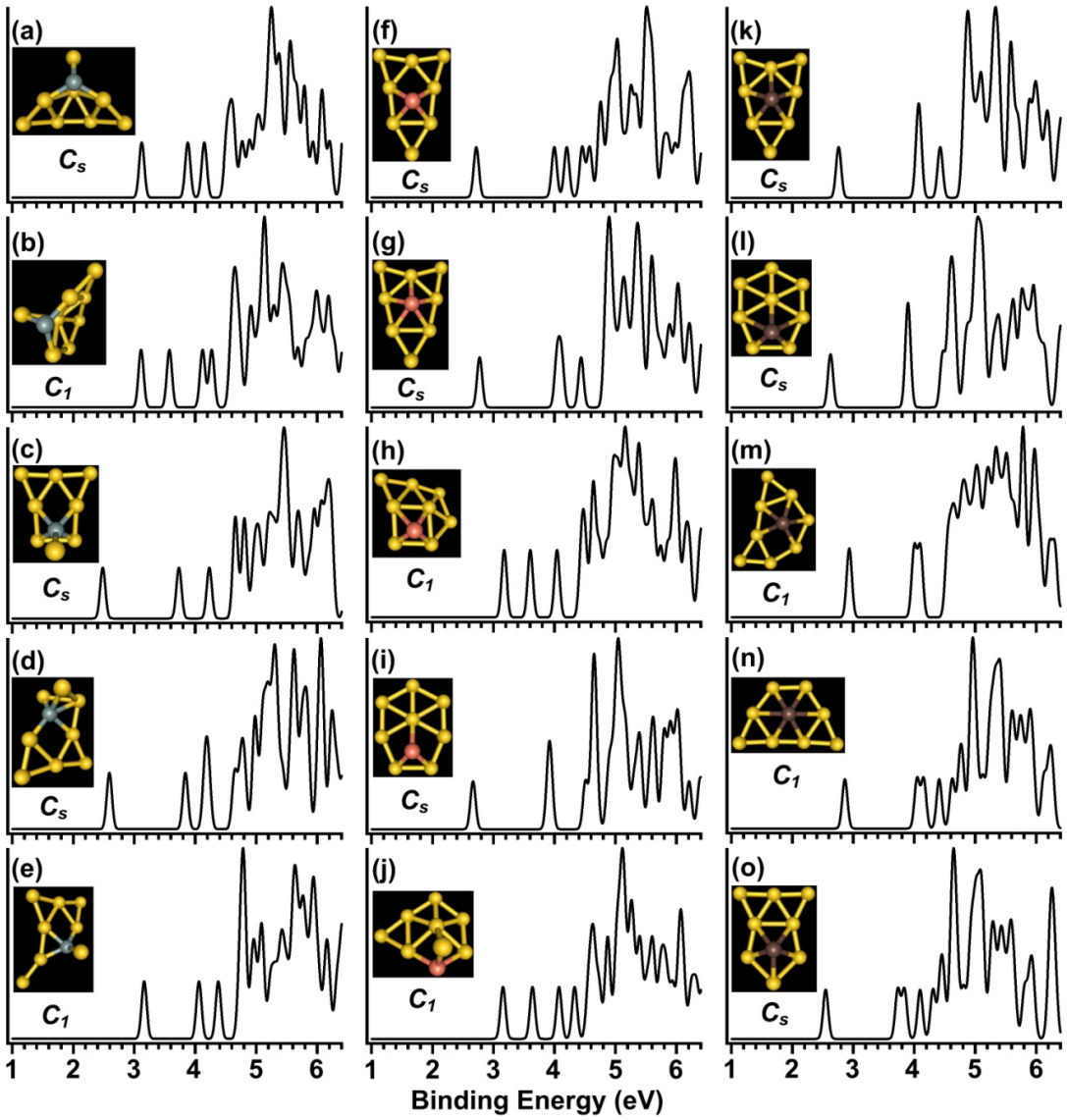

Figure 3.14 The simulated PES spectra of the top-five lowest-lying isomers of $SiAu_8^-$ (left, a – e), $GeAu_8^-$ (middle, f – j), and $SnAu_8^-$ (right, k – o). For each species, the isomers are numbered from the top to bottom (i.e. a – e, or f – j, or k – o) as isomer 1 to 5 in accordance with those in Table 3.5. The insets show the corresponding structures. The dopant atoms are shown in color (Si in grey, Ge in pink, and Sn in brown).

Table 3.2 Relative energies (eV) of five low-lying isomers of MAu_5^- (M = Si, Ge, Sn) at PBE/TZP (ADF) and PBEPBE/SDD (G03) levels of theory, as well as MP2/aug-cc-pVDZ//MP2/SDD, MP4(SDQ)/aug-cc-pVDZ//MP2/SDD, CCSD(T)/aug-cc-pVDZ//MP2/SDD, levels of theory for $SiAu_5^-$, MP2/aug-cc-pVDZ//MP2/SDD and MP4(SDQ)/aug-cc-pVDZ//MP2/SDD levels of theory for $GeAu_5^-$, and MP2/SDD and MP4(SDQ)/SDD//MP2/SDD levels of theory for $SnAu_5^-$. The VDEs are computed at PBE/TZP level and compared to the experimental values.

Isomer		Relative Energies (eV)					VDE (eV)	
		ADF	G03	MP2	MP4(SDQ)	CCSD(T)	ADF	Exp.
	1.	**0.000**	**0.000**	0.244	**0.000**	**0.000**	3.86	
	2.	0.466	0.199	**0.000**	0.024	0.139	3.86	
$SiAu_5^-$	3.	0.273	0.093	0.154	0.083	0.148	3.70	4.21 (3)
	4.	0.415	0.165	0.114	0.068	0.182	3.59	
	5.	0.377	0.363	0.668	0.277		3.23	
	1.	**0.000**	0.003	0.064	**0.000**		3.43	
	2.	0.045	0.066	**0.000**	0.003		3.99	
$GeAu_5^-$	3.	0.006	**0.000**	0.143	0.108		3.57	3.68 (4)
	4.	0.301	0.282				3.18	
	5.	0.322	0.255				4.27	
	1.	**0.000**	0.023	**0.000**	**0.000**		3.38	
	2.	0.046	0.093	0.092	0.092		3.90	
$SnAu_5^-$	3.	0.027	**0.000**	0.195	0.196		3.68	3.58 (4)
	4.	0.214	0.272	0.209			3.07	
	5.	0.311	0.381	0.210			2.67	

Table 3.3 Relative energies of five low-lying isomers of MAu_6^- (M = Si, Ge, Sn) at PBE/TZP (ADF) and PBEPBE/SDD (G03) levels of theory, as well as MP2/aug-cc-pVDZ//MP2/SDD and MP4(SDQ)/aug-cc-pVDZ//MP2/SDD levels of theory for $SiAu_6^-$ and $GeAu_6^-$, and MP2/SDD and MP4(SDQ)/SDD//MP2/SDD levels of theory for $SnAu_6^-$. The VDEs are at PBE/TZP level and compared to the experimental values.

Isomer		Relative Energies (eV)				VDE (eV)	
		ADF	G03	MP2	MP4(SDQ)	ADF	Exp.
	1.	0.121	0.006	**0.000**	**0.000**	2.62	
	2.	0.088	**0.000**	0.067	0.045	2.75	
$SiAu_6^-$	3.	**0.000**	0.125	0.584	0.309	2.63	2.70 (3)
	4.	0.082	0.171			3.37	
	5.	0.115	0.195			2.96	
	1.	**0.000**	**0.000**	**0.000**	**0.000**	2.58	
	2.	0.050	0.055	0.261	0.033	2.84	
$GeAu_6^-$	3.	0.126	0.118	0.191	0.147	3.00	2.65 (4)
	4.	0.136	0.110			2.29	
	5.	0.144	0.141			2.81	
	1.	0.009	0.056	0.156	**0.000**	2.75	
	2.	**0.000**	0.007	**0.000**	0.075	2.54	
$SnAu_6^-$	3.	0.032	**0.000**	0.170	0.281	2.33	2.57 (4)
	4.	0.116	0.131			2.90	
	5.	0.118	0.114			2.99	

Table 3.4 Relative energies (eV) of five low-lying isomers of MAu_7^- (M = Si, Ge, Sn) at PBE/TZP (ADF), PBEPBE/SDD (G03), MP2/SDD and MP4(SDQ)/SDD//MP2/SDD levels of theory. The VDEs are computed at PBE/TZP level and compared to the experimental values. Energies of the lowest-energy isomers are highlighted in bold.

Isomer		Relative Energies (eV)				VDE (eV)	
		ADF	G03	MP2	MP4(SDQ)	ADF	Exp.
	1.	0.139	**0.000**	**0.000**	**0.000**	3.34	
	2.	0.155	0.029	0.135	0.118	3.43	
$SiAu_7^-$	3.	**0.000**	0.136	0.925	0.644	3.56	3.40 (3)
	4.	0.251	0.203			3.36	
	5.	0.351	0.278			3.47	
	1.	**0.000**	**0.000**	**0.000**		3.32	
	2.	0.112	0.097	0.212		3.32	
$GeAu_7^-$	3.	0.110	0.106	0.430		3.55	3.38 (4)
	4.	0.326	0.302			3.28	
	5.	0.350	0.349			3.37	
	1.	0.021	0.059	**0.000**	**0.000**	3.30	
	2.	**0.000**	**0.000**	0.290	0.223	3.29	
$SnAu_7^-$	3.	0.230	0.223			3.32	3.30 (4)
	4.	0.334	0.399			3.70	
	5.	0.391	0.419			3.58	

Table 3.5 Relative energies of five low-lying isomers of MAu_8^- (M = Si, Ge, Sn) at PBE/TZP (ADF), PBEPBE/SDD (G03), and MP2/SDD levels of theory. The VDEs are computed at PBE/TZP level and compared to the experimental values. Energies of the lowest-energy isomers are highlighted in bold.

Isomer		Relative Energies (eV)			VDE (eV)	
		ADF	G03	MP2	ADF	Exp.
	1.	**0.000**	**0.000**		3.12	
	2.	0.189	0.160		3.11	
$SiAu_8^-$	3.	0.190	0.399		2.59	3.23 (3)
	4.	0.220	0.354		2.48	
	5.	0.226	0.334		3.16	
	1.	**0.000**	0.020	**0.000**	2.72	
	2.	0.007	**0.000**	0.216	2.77	
$GeAu_8^-$	3.	0.152	0.164	0.272	3.17	2.73 (4)
	4.	0.153	0.133	0.351	2.66	
	5.	0.216	0.217		3.15	
	1.	**0.000**	**0.000**		2.76	
	2.	0.179	0.177		2.63	
$SnAu_8^-$	3.	0.179	0.178		2.93	2.74 (4)
	4.	0.203	0.196		2.86	
	5.	0.244	0.227		2.54	

MAu_7^-. For $SiAu_7^-$, again while DFT (ADF) predicts a T_d $SiAu_4$-based structure (isomer 3, Figure 3.13c), all other levels of calculation locate a *quasi-planar* C_s structure (isomer 1, Figure 3.13a) as the global minimum (Table 3.4). This C_s isomer can be viewed as built upon isomer 1 of $SiAu_6^-$ by adding one Au atom to bond with the bridging gold and an apex gold atom. A similar structure has been reported for neutral $SiAu_7$.[163] For $GeAu_7^-$, the lowest-energy structure found is isomer 1, which has the same structure as $SiAu_7^-$ (Figure 3.13f). For $SnAu_7^-$, two DFT methods show that isomers 1 and 2 are very close in energy. While MP2 and MP4(SDQ) clearly favor isomer 1 as the global minimum (Table 3.4), which is a similar *quasi-planar* C_s structure as that of $SiAu_7^-$ and $GeAu_7^-$. In isomer 2, the Sn atom is penta-coordinated.

MAu_8^-. The C_s isomer 1 (Figure 3.14a) is found as the lowest-energy structure for $SiAu_8^-$, all other structures are substantially higher in energy (Table 3.5). It is a 3D structure containing a tetrahedral $SiAu_4$ unit. It can also be viewed as a dangling Au-Si unit sitting on the surface of a seven-gold-atom cluster. For $GeAu_8^-$, isomers 1 and 2 are nearly iso-energetic at DFT levels, while MP2 calculations predict isomer 1 as the global minimum. Isomers 1 and 2 are very similar, both can be viewed as evolved from the global minimum structure of $GeAu_7^-$ by adding one bridging Au atom at the bottom and some subsequent structural relaxation. In isomer 1 the dopant Ge atom is tetra-coordinated, while in isomer 2 it is penta-coordinated (Figure 3.14f, g). Note that isomer 3, which is 0.152 eV above isomer 1 at PBE/TZP (ADF) level, can also be derived from the global minimum of $GeAu_7^-$ by adding a bridging Au atom at a side instead of at the bottom. For $SnAu_8^-$, isomer 1 with C_s symmetry is located as the global minimum. It is the same structure as isomer 2 of $GeAu_8^-$ but with a penta-coordinated Sn (Figure 3.14k).

3.3.4. Structure Assignments

MAu_5^-. For $SiAu_5^-$, the lowest-energy isomer 1 gives a well-matched PES pattern as compared to the experiment. Specifically it gives congested features in between 4–5 eV and 5–6 eV, which can be qualitatively correlated with the broad features A and B in the experimental spectra, respectively (Figure 3.7d). Moreover, considering its likelihood of growing from the very stable T_d-$SiAu_4$,[127] as suggested by the similarities between its spectrum and that of $SiAu_4^-$, we assign isomer 1 (C_{3v}) as the most stable structure of $SiAu_5^-$. Molecular orbital analysis (see Figure 3.15a) shows that the HOMO of $SiAu_5^-$ is primarily made up of the 6*s* atomic orbital of the terminal Au atom, while the HOMO-1 is nearly identical to the HOMO of neutral $SiAu_4$.[162] This indicates that its electronic structure is not significantly altered as compared to $SiAu_4$ and the extra terminal Au atom in $SiAu_5^-$ provides a relatively localized orbital to accommodate the two extra electrons (relative to $SiAu_4$), consistent with the experimental observations.

For $GeAu_5^-$, the simulated PES spectrum of the global minimum structure, isomer 1 (C_s), agrees best with the experiment. Particularly, the first doublet features (X and A) are well reproduced in the simulation. All other structures should have negligible contribution to the PES spectrum. For $SnAu_5^-$, isomer 1 (C_s) is assigned as the primary structure which is similar to that of $GeAu_5^-$, consistent with their similar PES spectra. Isomer 5 of $SnAu_5^-$ gives a transition at ~ 2.7 eV, and it is assigned as a minor isomer to account for the weak feature (X') observed in its spectrum. Both isomers 1 and 5 can be viewed as derived from the square-pyramidal $SnAu_4$.[162]

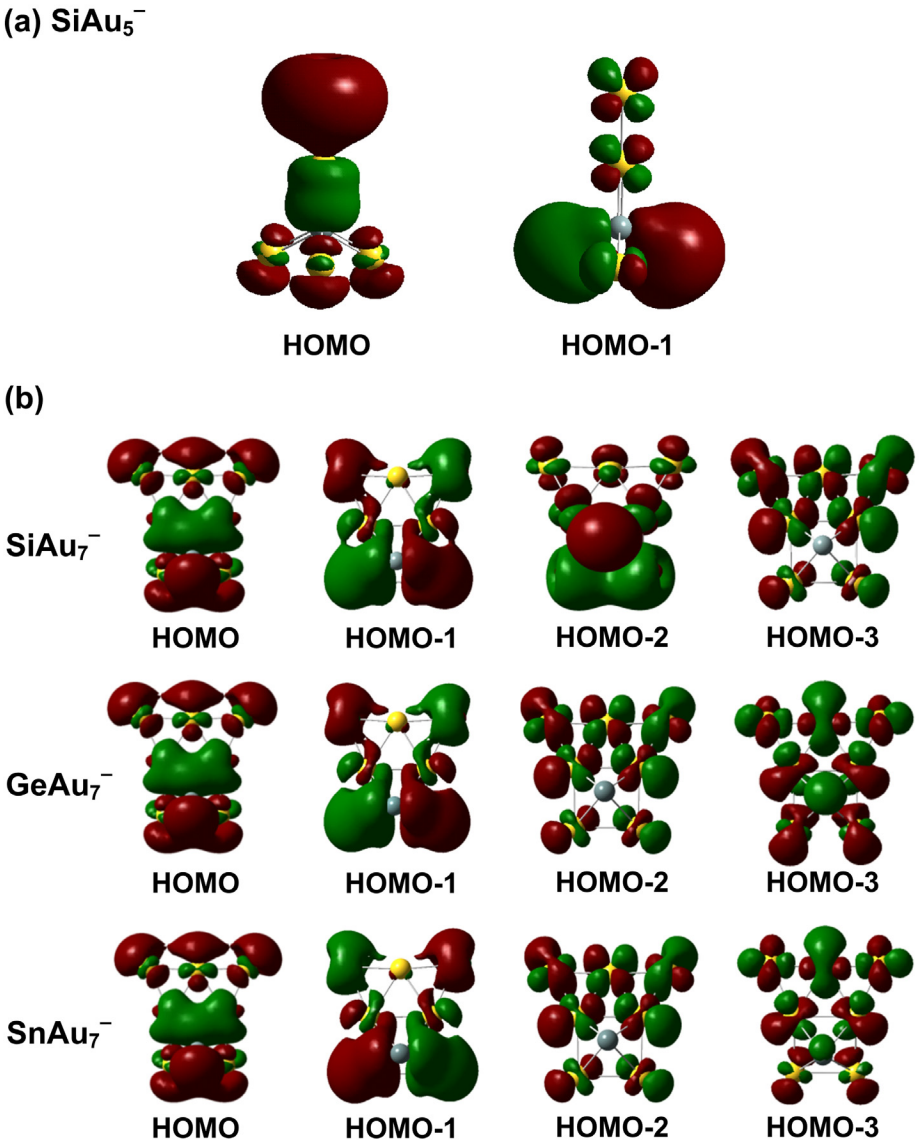

Figure 3.15 Selected frontier molecular orbitals of (a) $SiAu_5^-$ and (b) MAu_7^- (M = Si, Ge, Sn).

MAu_6^-. For $SiAu_6^-$, the top-3 isomers all appear to provide good match to the experimental PES spectra in terms of the first VDE and the HOMO-LUMO gap (Figure 3.12a-c). However, based on the energy ordering at high-level MP4(SDQ) calculations (Table 3.3), as well as its similarity to $GeAu_6^-$ and $SnAu_6^-$ as suggested by the experimental observations, isomer 1 (C_1) is taken as the ground state structure for $SiAu_6^-$.

For $GeAu_6^-$, the global-minimum isomer 1 gives the best match to the experimental PES spectrum (Figure 3.12f) and its VDE is also in good agreement with the observed value (Table 3.3). The nearly iso-energetic isomer 2 is assigned as a minor isomer, whose simulated PES spectrum well reproduces the weak feature (X') observed in the experimental spectrum (Figure 3.8b, e). For $SnAu_6^-$, the nearly iso-energetic isomers 2 and 1 are assigned as the primary and the secondary isomers contributing to the PES spectrum, respectively, similar to the case of $GeAu_6^-$. However, for $SnAu_6^-$, the experimental PES spectrum suggests that there is an additional minor isomer populated in the beam, which gives rise to the weak peak X" at ~ 2.30 eV. Indeed, isomer 3 is found to be only 0.032 eV above the global minimum (at PBE/TZP level) and its first VDE (2.33 eV) agrees very well with that of the band X" (Figure 3.8f).

We would like to point out that the band B in the experimental spectra, assigned to transitions to singlet final states of neutral MAu_6, could not be reproduced in the theoretical simulations (Figure 3.8), because the simulated PES spectra are basically plots of density of states, disregarding the detailed electronic configurations.

MAu_7^-. For MAu_7^- (M = Si, Ge, Sn), isomer 1 is universally assigned for each species. They all represent the global minimum at the *ab initio* levels and their simulated PES spectra agree well with the experiment (Figure 3.9). For $SiAu_7^-$, the theoretical

results show that the second band in the simulated PES spectrum (Figure 3.9d), which is apparently higher and broader than that of $GeAu_7^-$ and $SnAu_7^-$, indeed contains two transitions separated by 0.069 eV. This is in good agreement with the doublet features (A and B) in the experimental PES spectrum with a separation of 0.12 eV (Figure 3.9a), confirming the global minimum of isomer 1. For $GeAu_7^-$ and $SnAu_7^-$, isomer 2 also shows good agreement with the experiment. However, it is ruled out based on its higher energy at MP2 and MP4(SDQ) levels, as well as the experimental evidence of the similarities among the three MAu_7^- clusters.

The first four molecular orbitals of MAu_7^- are plotted in Figure 3.15b. Interestingly, although MAu_7^- have very similar structures, their molecular orbitals show some differences in orders. Particularly, the HOMO-2 of $SiAu_7^-$, which is dominated by the Si atom, is very different from that of $GeAu_7^-$ and $SnAu_7^-$ which shows little contribution from the dopant atom. This well explains the appreciable difference observed in the VDE of the B band, which corresponds to detachment from HOMO-2, between $SiAu_7^-$ and $GeAu_7^-$/$SnAu_7^-$ (Figure 3.9), lending further support to the structure assignment for MAu_7^-.

MAu_8^-. For M = Si and Sn, clearly structure 1 is the primary isomer observed in the experiment. It is the lowest energy structure by DFT calculations, and its simulated PES spectrum agrees very well with the experimental data except that transitions to singlet states could not be reproduced in the simulation (Figure 3.10d, f). For $GeAu_8^-$, isomers 1 and 2 are very similar in structure, so are their simulated PES spectra (Figure 3.14f, g). They both fit the experimental VDE well. Considering their very close energies (at DFT level, see Table 3.5), it is possible that both isomers 1 and 2 of $GeAu_8^-$ are

populated. As aforementioned, the complicated PES spectrum of $GeAu_8^-$ suggests that there should be at least one more isomer present to account for the features X', A' and B'. The next low-lying structure, isomer 3, seems to fit. As seen in Figure 3.10e, by assuming equal population of isomers 1, 2 and 3, the simulated PES spectra of the mixture acquires good agreement with the experimental data. However, we note that isomer 3 is > 0.15 eV (PBE/TZP level) above the calculated global minimum. Usually it is rare to have such high energy isomer with large population in the experiment. One possibility is that the relative energy of isomer 3 for $GeAu_8^-$ may be somewhat overestimated by the current theoretical methods.

3.3.5. Discussion

As seen in Figures 3.7–3.10, the most intriguing finding in our structural study of MAu_{5-8}^- (M = Si, Ge, Sn) is the 3D ($SiAu_5^-$) → *quasi-planar* 2D ($SiAu_6^-$ and $SiAu_7^-$) → 3D ($SiAu_8^-$) structural evolution of the Si doped clusters, which leads to a structural convergence for MAu_x^- (M = Si, Ge, Sn) at x = 6, 7. It reflects the competition between the strong tendency of forming tetrahedral bonding structures around the Si atom (M-Au interactions) and the strong tendency of forming planar structures for small anion gold clusters (Au-Au interactions). We have shown before that due to the strong sp^3 hybridization of the Si atom, the structures of Si-doped gold clusters are usually dominated by the local tetrahedral $SiAu_4$ unit, e.g. in $SiAu_4^-$.[127] While the corresponding Ge or Sn doped gold clusters show different structural motif, reflecting its less tendency of sp^3 hybridization in the doped clusters. Particularly, $GeAu_4^-$ and $SnAu_4^-$ do not have T_d structures as that of $SiAu_4^-$, but a square-pyramidal structure in which the dopant atom is

located slightly above the plane of a square Au_4 unit.[162] This structural behavior of MAu_4^- also correlates with the trend of M-Au bonding energy, which is ~ 71.2, 68.1 and 66.2 kcal/mol, respectively, for M = Si, Ge, and Sn (computed at the CCSD(T)/SDD//MP2/SDD level of theory). Our current results show that, due to the high stability of tetrahedral $SiAu_4$, the structure of $SiAu_5^-$ is still T_d-based, in which the Si atom is tetrahedrally coordinated to four Au atoms to optimize the local Si-Au interactions. However, $SiAu_6^-$ and $SiAu_7^-$ show *quasi-planar* structures, in which the Si atom is also four-fold coordinated but with a square-pyramidal local arrangement. This anomaly in structural evolution reflects that as the cluster size increases, the Au-Au interactions become competitive and important in determining the cluster structures. The strong tendency of forming planar structures for Au_6^- and Au_7^- results in the *quasi-planar* structures of $SiAu_6^-$ and $SiAu_7^-$ in which the Au-Au interactions dominate. As the number of gold atoms further increases, the delicate balance between the abovementioned two factors results in the convex structure for $SiAu_8^-$, which can be viewed as an Au-Si dangling unit bonded to a quasi-planar Au_7. On the other hand, the dopants Ge and Sn behave similarly in the doped clusters under study. The major isomers of $GeAu_{5-8}^-$ all have similar structures as the corresponding $SnAu_{5-8}^-$ clusters, and they can simply be viewed as evolved from the motif of square-pyramidal $GeAu_4^-$ and $SnAu_4^-$, respectively, by successive addition of Au atoms with subsequent structural relaxation.

3.3.6. Conclusion

In conclusion, we have conducted a combined photoelectron spectroscopy and computational study on the structural evolution of doped gold anion clusters MAu_x^- (M =

Si, Ge, Sn; x = 5–8). For x = 5, the $SiAu_5^-$ cluster was observed to have a tetrahedral-based 3D structure, while the primary isomers of $GeAu_5^-$ and $SnAu_5^-$ have quasi-planar structures based on a square-pyramid motif. For x = 6 and 7, all the three doped clusters MAu_x^- (M = Si, Ge, Sn) exhibit similar *quasi-planar* structures. This unusual structural convergence reflects a subtle and delicate competition between Au-Au interactions and Au-M interactions in determining the structures of the MAu_x^- clusters. For x = 8, $SiAu_8^-$ again has a 3D structure showing an Au-Si dangling unit on top of a quasi-planar seven-gold-atom surface. In contrast, $GeAu_8^-$ and $SnAu_8^-$ still have quasi-planar structures. In the future work, it would be interesting to locate the size at which the quasi-2D to 3D transition occurs in MAu_x^- (M = Ge, Sn).

CHAPTER FOUR

DOPING THE GOLDEN BUCKYBALLS

4.1. Introduction

During our continued efforts in the investigation of gold clusters, motivated primarily by the discovery of the novel catalytic properties of supported gold nanoparticles,[20] one of our recent studies on the structures of Au_n^- clusters in the medium size range (n = 15-19) has shown that Au_n^- clusters with n = 16-18 possess unprecedented empty cage structures.[105] In particular, the Au_{16}^- cluster has a beautiful tetrahedral structure with an inner diameter of about 5.5 Å and can be compared to the fullerenes (buckyballs).[7] Although polyhedral cages are common in inorganic compounds,[167] hollow cages of metal clusters with large internal volumes are very rare.[18,168] Au_{32} was first suggested to be a "24-carat golden fullerene",[114,169] however, subsequent experiment showed that the Au_{32}^- anion is in fact a low-symmetry compact 3D structure.[104] Other larger gold cage clusters have also been proposed computationally,[170-172] but none has been observed or is expected to be the global minimum. The cage structures of Au_{16}^- and Au_{17}^- have recently been confirmed by trapped ion electron diffraction experiment[106] and thus they represent the first experimentally confirmed smallest hollow golden cages.

It is known that the fullerene buckyballs can host foreign atoms inside to form endohedral fullerenes.[173-175] The large empty space inside the golded cage clusters immediately suggested that they can also be doped with a foreign atom to produce a new class of endohedral gold cages, analogous to the endohedral fullerenes.[173-176] A gold cage containing a central atom was first predicted for a series of icosahedral clusters $M@Au_{12}$

(M = W, Ta^-, Re^+) based on the 18-electron rule[125] and has been subsequently confirmed experimentally.[126,177] However, since Au_{12} itself does not possess a cage structure, the dopant atom with the appropriate electron count plays an essential role in holding the cage together in $M@Au_{12}$. Following the discovery of the golden cages,[105] two subsequent theoretical studies have appeared concerning doping them with a foreign atom of Si/Al,[178] and Mg,[179] respectively. Since the parent Au_{16}^- and Au_{17}^- clusters are empty cages, many different types of atoms may be used as dopants to form new endohedral gold clusters.

It has been shown that only alkali, alkali earth, or rare earth elements can be doped inside the fullerenes to form charge transfer complexes,[180] while transition metal (M) atoms do not form endohedral fullerenes due to the strong M-C interactions that lead to the formation of metal carbides. It would be interesting and important to understand what kind of atoms can be doped inside the golden buckyballs, and how the structures and the electronic and magnetic properties of the gold cage clusters are affected by the doping. In this chapter, I present a systematic investigation of doping the golden buckyballs with a series of different atoms. Our results show that main group metal elements like Cu, Ag, Zn, and In can be doped inside the golden buckyball with little structural distortion, and they form charge transfer complexes with the gold cluster. However, doping with a group-14 atom Si, Ge or Sn leads to exohedral structures, in which the parent cage structure is significantly distorted by strong dopant-gold covalent bond. Transition metal atoms Fe, Co and Ni can also be doped inside the golden cage, but with appreciable distortions to its initial symmetry due to d-d interactions. The dopant

atom Fe, Co and Ni maintain their atomic-like magnetic moments in the doped clusters, forming a class of endohedral clusters with varying magnetic properties.

4.2. $Cu@Au_{16}^-$ and $Cu@Au_{17}^-$ Clusters

We start with doping the two smallest golden cages Au_{16}^- and Au_{17}^- with a Cu atom.[181] The $CuAu_{16}^-$ and $CuAu_{17}^-$ clusters were produced by laser vaporization of an Au/Cu composite disk target containing about 7% Cu, and their photoelectron spectra were taken at 193 nm.

Figure 4.1 shows the spectra of $CuAu_{16}^-$ and $CuAu_{17}^-$ along with those of the parent gold clusters.[105] Let us first focus on $CuAu_{16}^-$, whose PES spectrum is remarkably similar to that of the parent Au_{16}^-, as can be seen clearly in Figure 4.1. The first three features (X, A, B) and the gap between B and C are all very similar in the PES spectra of the two systems, except that the intensity of the ground state band (X) is greater for the doped cluster $CuAu_{16}^-$ and its electron binding energies are slightly higher (Table 4.1). The similarity between the spectra of $CuAu_{16}^-$ and Au_{16}^- suggest that the Cu doping does not alter significantly the geometric and electronic structures of Au_{16}^-, which is possible only if Cu is trapped inside the Au_{16}^- cage. The Au_{16}^- cluster itself is unique and its PES spectrum does not exhibit an energy gap as other even-sized gold clusters in this size range.[15,101,105] The high electron binding energies and the lack of an energy gap suggested that the Au_{16} neutral cluster is open-shell and possibly with two unpaired electrons (a triplet state). This means that two extra electrons would be required to reach a closed shell 18-electron Au_{16}^{2-} (18 electrons correspond to a major shell closure ($1S^21P^61D^{10}$) in the electron shell model[3,42]), which is also born out from a recent theoretical work.[178]

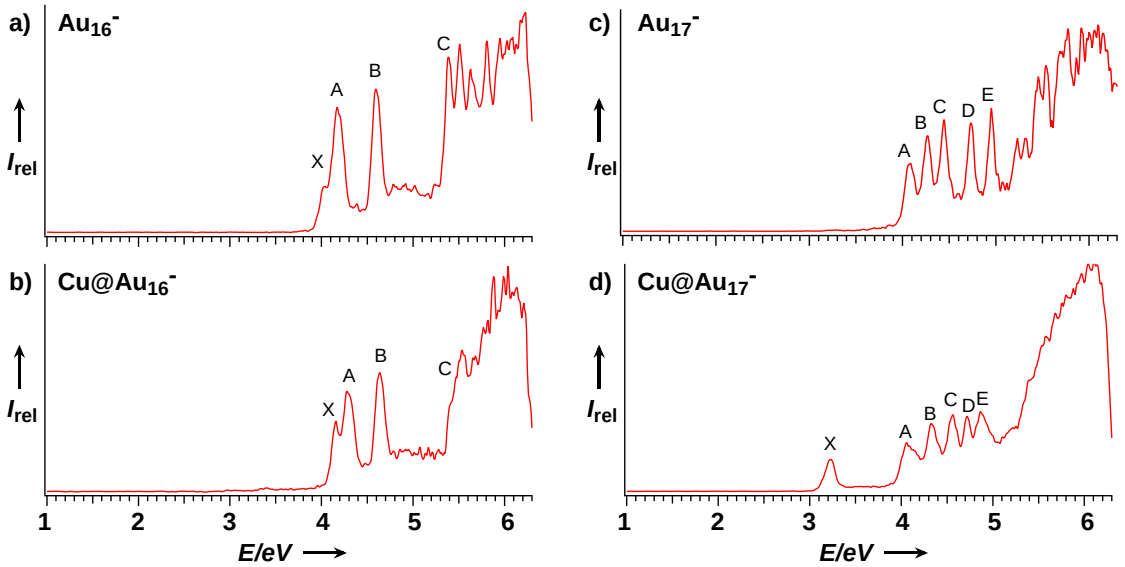

Figure 4.1 Photoelectron spectra of $CuAu_{16}^-$ and $CuAu_{17}^-$, compared to Au_{16}^- and Au_{17}^-.

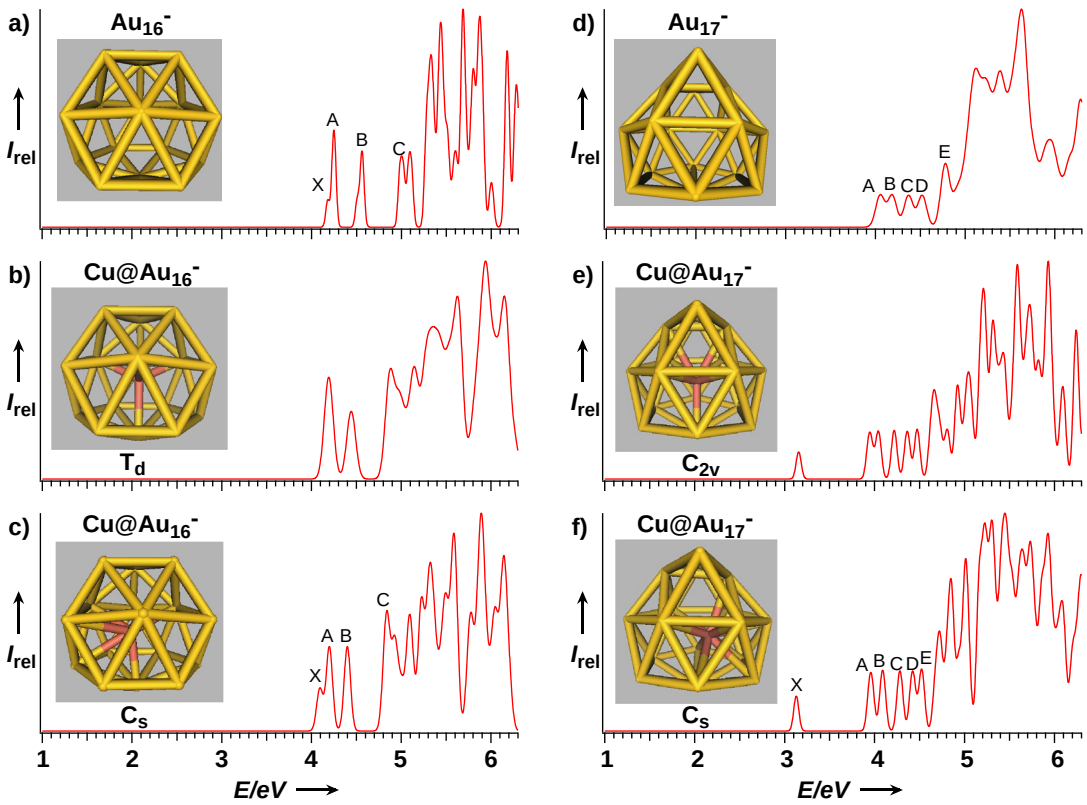

Figure 4.2 Simulated photoelectron spectra of two endohedral structures each for $Cu@Au_{16}^-$ and $Cu@Au_{17}^-$ along with those for Au_{16}^- and Au_{17}^-.

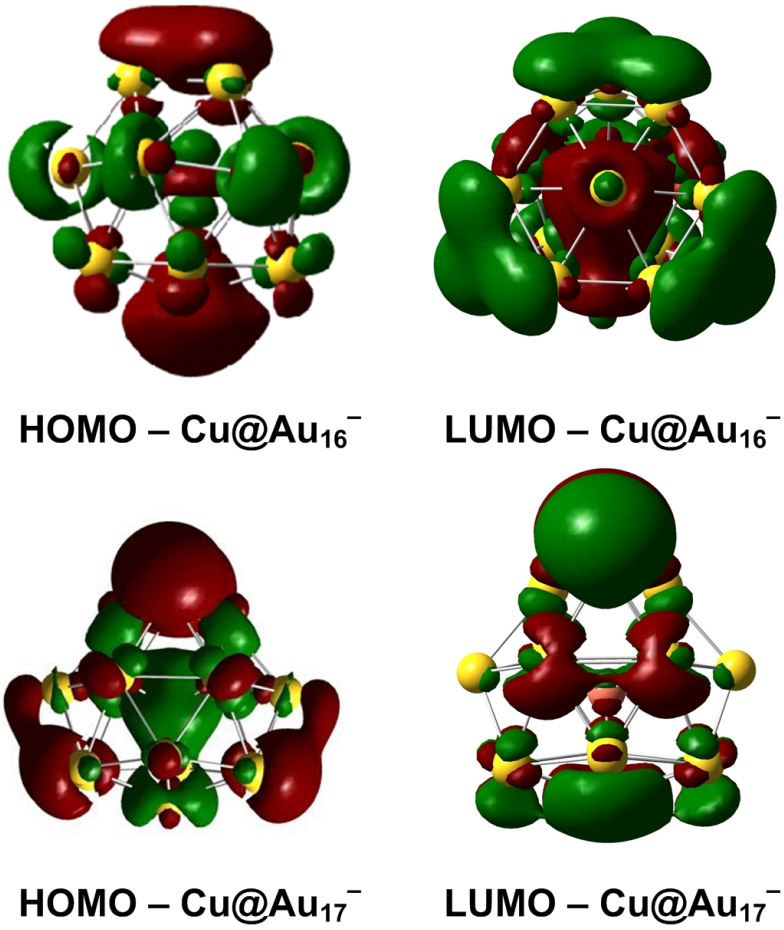

Figure 4.3 The HOMO and LUMO of $Cu@Au_{16}^-$ (C_s) and $Cu@Au_{17}^-$ (C_{2v}).

Table 4.1 Experimental adiabatic (ADE) and vertical (VDE) detachment energies of the doped clusters $Cu@Au_{16}^-$ and $Cu@Au_{17}^-$ along with those of Au_{16}^- and Au_{17}^-, and the calculated values. All energies are in eV.

Species	Experimental		Theoretical
	ADE	VDE	VDE
Au_{16}^-	3.99 ± .03	4.03 ± 0.03	4.179
$Cu@Au_{16}^-$ (C_s)	4.12 ± 0.05	4.16 ± 0.03	4.092
Au_{17}^-	4.03 ± 0.03	4.08 ± 0.03	4.053
$Cu@Au_{17}^-$ (C_{2v})	3.16 ± 0.06	3.23 ± 0.03	3.155

Because of the high electron affinity of Au, the Cu atom can be viewed as donating an electron to the Au_{16}^- cage in $CuAu_{16}^-$, giving rise to a closed shell and stable Au_{16}^{2-} species. Thus, $CuAu_{16}^-$ can be viewed as $Cu^+@Au_{16}^{2-}$.

The spectrum of $CuAu_{17}^-$ is also very similar to that of the parent gold cluster Au_{17}^-, except that there is one low binding energy peak followed by a large energy gap in the spectrum of the Cu-doped cluster (Figure 4.1d). The five peaks between 4-5 eV in the spectrum of $CuAu_{17}^-$ (labeled A-E in Figure 4.1d) are remarkably similar to the five characteristic low binding energy features in the spectrum of Au_{17}^- (Figure 4.1c). This spectral similarity again suggested that the Cu doping induced very little structural change to the Au_{17}^- cage except that it donates one electron. Au_{17}^- is closed shell with 18 valence electrons, therefore the extra electron from the dopant is expected to enter the LUMO of the Au_{17}^- cage, giving rise to the low-binding-energy peak (X) in the spectrum of $CuAu_{17}^-$ (Figure 4.1d). All these observations again imply that Cu stays in the center of the Au_{17}^- cage ($Cu^+@Au_{17}^{2-}$) and does not perturb the electronic and geometric structures of the cage significantly.

To confirm these observations, we carried out theoretical calculations. The results revealed that the endohedral $Cu@Au_{16}^-$ and $Cu@Au_{17}^-$ clusters are overwhelmingly favored than any other structures with the Cu atom on the outside of the cage. Figure 4.2 shows the simulated PES spectra of two endohedral structures each for $Cu@Au_{16}^-$ and $Cu@Au_{17}^-$ in comparison to those of the bare clusters. In one structure, the Cu atom sits in the center of the cages and in the other the Cu atom is slightly displaced from the center. The energy differences between the two isomers are very small and their simulated PES spectra are also very close to each other. The endohedral $Cu@Au_{16}^-$ with

Cu in the center possesses T_d symmetry with a triply degenerate HOMO orbital, which gives rise to the first simulated PES band (Figure 4.2b). In the structure in which the Cu atom is displaced from the center, the $Cu@Au_{16}^-$ cluster becomes C_s symmetry and the triplet degenerate HOMO is split, giving rise to the doublet peaks (X and A) in the simulated PES spectrum (Figure 4.2c), which is in excellent agreement with the experiment (Figure 4.1b). For $Cu@Au_{17}^-$, the C_{2v} and C_s structures are almost degenerate in energies (C_s is 0.034 eV more stable), and the simulated spectra for them are similar to each other and both are in good agreement with the experiment, suggesting that the Cu atom in the center of the Au_{17}^- cage might be somewhat fluxional. The calculated VDEs for $Cu@Au_{16}^-$ and $Cu@Au_{17}^-$ are also in good agreement with the experimental values (Table 4.1). Overall, the excellent agreement between theory and experiment confirms unequivocally the endohedral structures of the Cu doped smallest golden cages. It is important to note that even in the low symmetry structures the Au_{16}^- and Au_{17}^- cages are not distorted significantly from the parent clusters. Figure 4.3 shows the frontier orbitals of the two endohedral clusters, in which the electron densities are clearly dominated by the cages with little contribution from the central Cu atom, consistent with the description of $Cu@Au_{16}^-$ and $Cu@Au_{17}^-$ as $Cu^+@Au_{16}^{2-}$ and $Cu^+@Au_{17}^{2-}$, respectively. The Mulliken charge and natural population analyses show that the Cu atom in $Cu@Au_{16}^-$ and $Cu@Au_{17}^-$ indeed carries a positive partial charge. The charge transfer interactions between the cage and its dopant are also reminiscent of the endohedral fullerenes[173-176] and is consistent with strong ionic character in the CuAu diatomic molecule.[182]

Doping gold clusters can provide a powerful way to fine tune its chemical and physical properties.[183-185] Our current success in the Cu doping suggests that indeed a

new class of endohedral golden cages is viable. In these cases, the cage structures of Au_{16}^- and Au_{17}^- are maintained by simply changing the dopant atoms, similar to the cases of endohedral fullerenes.[173-176]

4.3. M@Au_{16}^- (M = Ag, Zn, In) Clusters

Our work on the Cu-doped golden buckyballs[181] spurred immediate theoretical interests,[186-189] suggesting possible doping with other atoms. In one of the studies, Sun *et al.*[187] showed that Si cannot be doped into the Au_{16}^- cage, in contradiction with a previous theoretical suggestion.[178] In another theoretical study, Sun *et al*. also investigated the Au_{16} cage doped with a W atom and found that the resulting WAu_{16} cluster is distorted to a W@Au_{12} unit plus four additional Au atoms on the outside.[188] As discussed above, the W@Au_{12} cluster was predicted previously by Pyykkö and Runeberg to be a highly stable 18-electron icosahedral cluster[125] and was confirmed experimentally.[126] A more recent theoretical study suggested that Li and Na atom can be doped into the Au_{16}^- cage, while Ag and K cannot be doped inside because of their larger atomic sizes.[189] In this subsection, we investigate the doping of the golden cage by three metal atoms, Ag, Zn, and In, which possess different numbers of valence electrons.[190] The inclusion of Ag also allows us to examine the effects of dopant size by comparing with our previous work on Cu@Au_{16}^-. Our results show that all three elements can be doped into the Au_{16}^- cage to form highly stable endohedral M@Au_{16}^- clusters with little distortion to the parent cage. We further show that the interactions between the dopant atoms and the golden cage can be viewed as charge transfer from the dopant to the cage, demonstrating that the electronic structures of the gold cage can be tuned systematically,

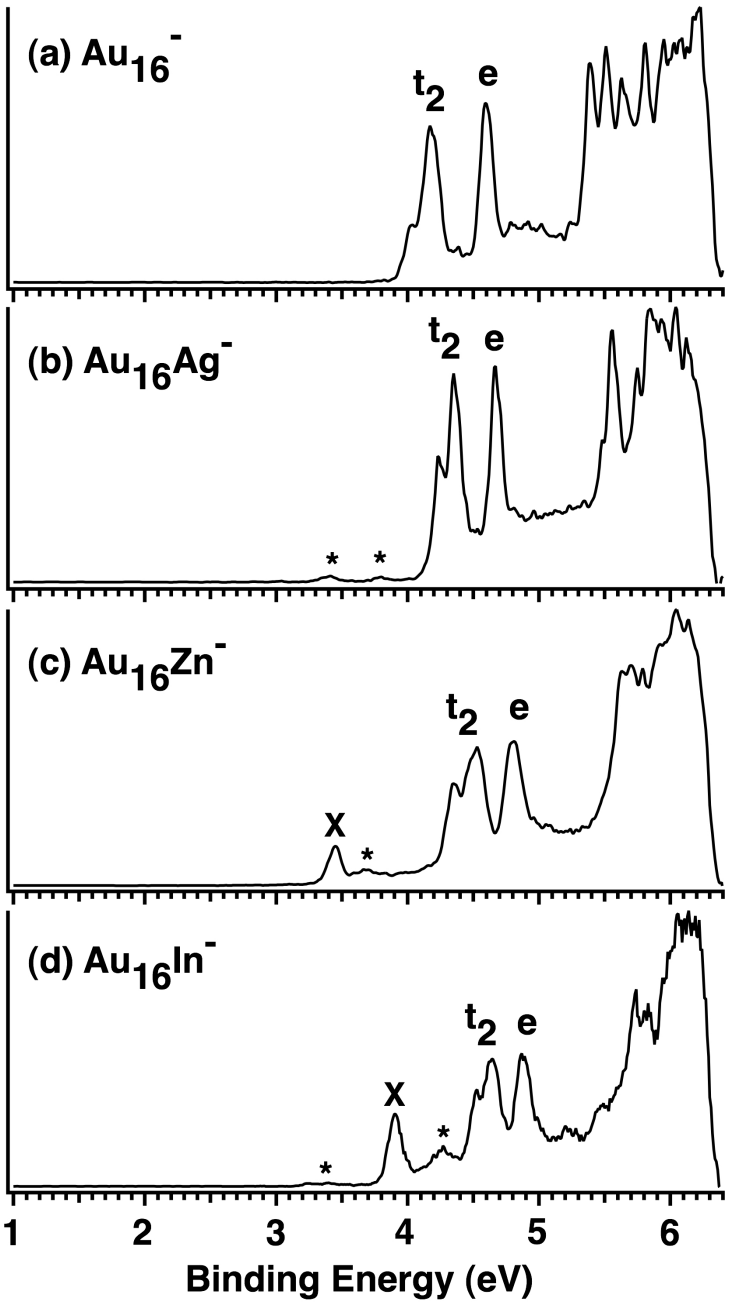

Figure 4.4 photoelectron spectra of the doped golden cages $Au_{16}M^-$ (M = Ag, Zn, In) at 193 nm, compared to that of Au_{16}^-.

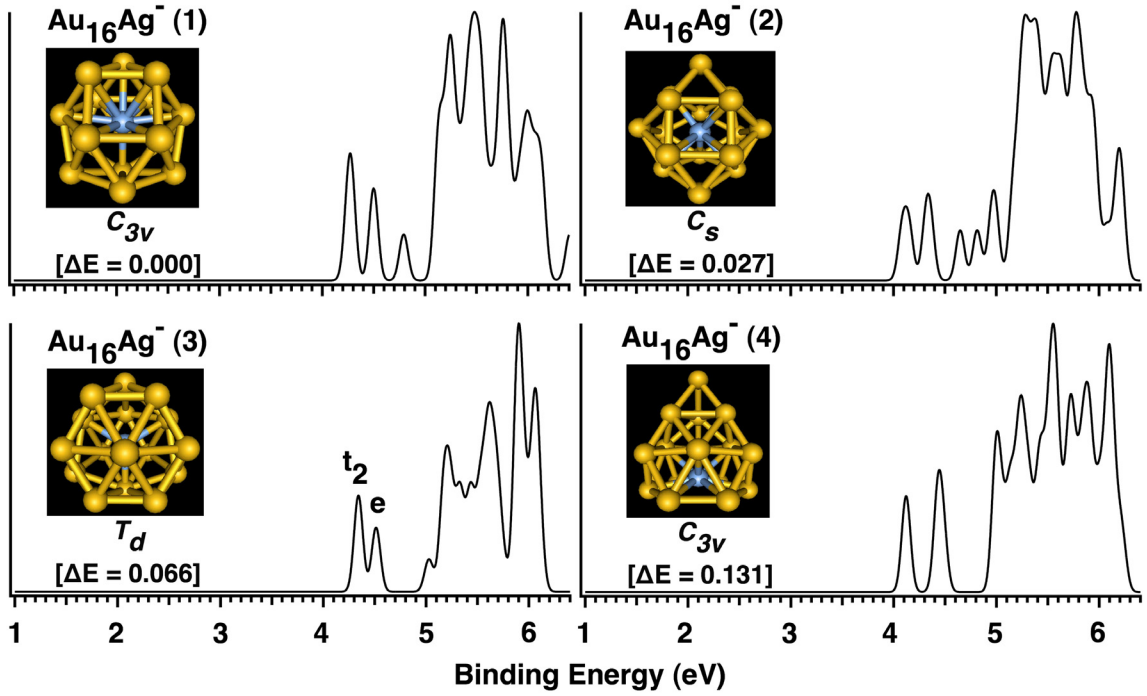

Figure 4.5 Structures, relative energies (ΔE) in eV, and simulated photoelectron spectra for the four low-lying isomers of $Au_{16}Ag^{-}$.

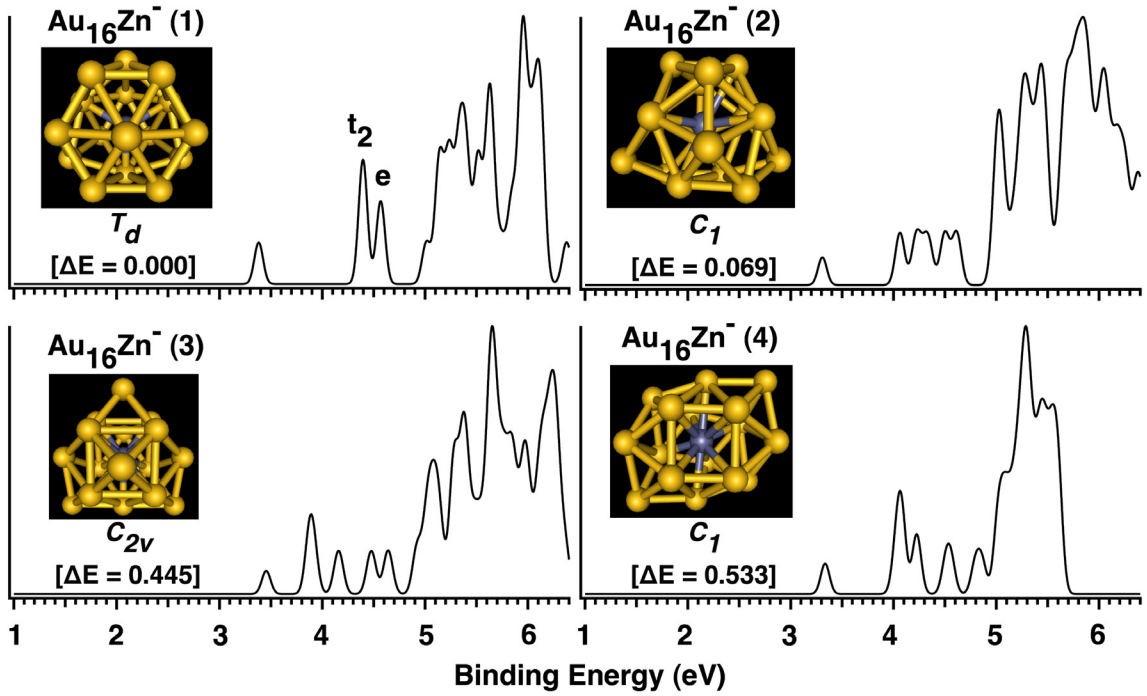

Figure 4.6 Structures, relative energies (ΔE) in eV, and simulated photoelectron spectra for the four low-lying isomers of $Au_{16}Zn^{-}$.

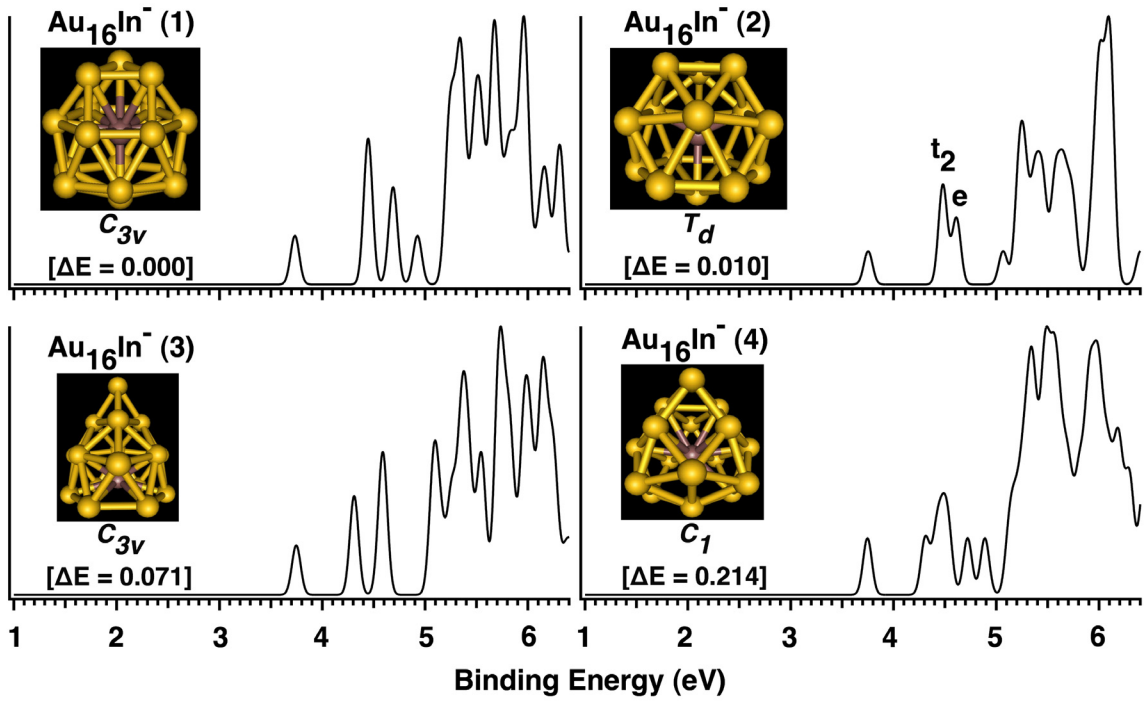

Figure 4.7 Structures, relative energies (ΔE) in eV, and simulated photoelectron spectra for the four low-lying isomers of $Au_{16}In^{-}$.

Table 4.2 The measured vertical detachment energies (VDE) compared to calculated VDE for the T_d isomers of the doped clusters $M@Au_{16}^-$ (M = Ag, Zn, In).

	VDE (eV)	
	Exp	Theo
$Ag@Au_{16}^-$ (T_d)	4.23 ± 0.04	4.34
$Zn@Au_{16}^-$ (T_d)	3.46 ± 0.04	3.38
$In@Au_{16}^-$ (T_d)	3.91 ± 0.04	3.75

by changing the dopant atom with different valence electrons.

The MAu_{16}^- (M = Ag, Zn, In) clusters were produced by laser vaporization of Au/M composite disk targets containing about 7% Ag, 8% Zn, and 4% In, respectively, and their photoelectron spectra were measured at 193 nm. Figure 4.4 displays the photoelectron spectra of the three MAu_{16}^- clusters, along with that of Au_{16}^- for comparison. The spectrum of $AgAu_{16}^-$ (Fig. 4.4b) is similar to that of Au_{16}^- with three well-resolved peaks in the low binding energy range between 4.1-4.8 eV followed by a large energy gap and more congested spectral features beyond 5.5 eV. The spectra of $ZnAu_{16}^-$ and $InAu_{16}^-$ are similar to that of $AgAu_{16}^-$ except an extra low binding energy feature (X) in the doped clusters. We note that the low binding energy band X in the $InAu_{16}^-$ spectrum (Fig. 4.4d) has a higher electron binding energy than that in the $ZnAu_{16}^-$ and is also more intense. The weak features denoted with "*" in the spectra of MAu_{16}^- are either due to impurities or weakly populated isomers. The VDEs of the ground state bands for the three MAu_{16}^- clusters are given in Table 4.2 and compared with the theoretical values.

As discussed previously,[105,181] the Au_{16}^- spectrum is unique: it has a very high electron binding energy and does not exhibit a large energy gap like other even-sized gold clusters,[15,101] which is because the tetrahedral Au_{16} cage is open shell with two unpaired electrons and two extra electrons are needed to make a closed-shell 18-electron Au_{16}^{2-} cage. Walter and Hakkinen[178] used the electron shell model to rationalize the high stability of the Au_{16}^{2-} cage with three filled electron shells, $1s^21p^61d^{10}$. The five-fold degenerated 1d shell transforms into a three-fold degenerated t_2 and a two-fold degenerated e molecular orbitals (MOs) under the T_d symmetry crystal field splitting. The

t_2 orbital is the highest occupied MO, which can be further split by the Jahn-Teller effect, as shown in the PES spectrum of Au_{16}^- in Fig. 4.4a. The higher binding energy features beyond 5 eV are mainly due to the gold 5d band, whereas the 1s and 1p shells possess much higher electron binding energies according to Walter and Hakkinen. Thus, the relatively simple spectral pattern due to the 1d shell, i.e., the t_2 and e MOs, provides the electronic fingerprint for the T_d cage structure of Au_{16}^- and may be used as experimental evidence to judge whether the cage is significantly distorted upon doping with a given atom.

As shown in Fig. 4.4, the spectral signatures due to the t_2 and e orbitals can be clearly recognized in the PES spectra of all the three doped species, MAu_{16}^- (M = Ag, Zn, In), suggesting that the electronic structures and the near-T_d symmetry of the Au_{16}^- cage are not significantly distorted by the doping, which is possible only if the dopant atoms are trapped inside the cage. The spectrum of $AgAu_{16}^-$ (Fig. 4.4b) is almost identical to that of $CuAu_{16}^-$ because both are 18-electron closed-shell systems and can be viewed as $M^+@Au_{16}^{2-}$. Zn is valence two and can donate two electrons to the Au_{16} cage. Therefore, neutral $ZnAu_{16}$ is an 18-electron system isoelectronic to $AgAu_{16}^-$ and $CuAu_{16}^-$. In the $ZnAu_{16}^-$ anion, the extra electron should enter the next shell, which is the 2s shell. The large energy gap observed in the spectrum of $ZnAu_{16}^-$ (Fig. 4.4c) represents the 1d-2s energy gap and suggests that neutral $ZnAu_{16}$ should be a highly stable species. Similarly, indium has three valence electrons and the extra electron should fill up the 2s shell, giving rise to a highly stable 20-electron $InAu_{16}^-$ cage ($1s^21p^61d^{10}2s^2$). The fact that the X band of $InAu_{16}^-$ is more intense and has a higher binding energy than that in the $ZnAu_{16}^-$ spectrum is consistent with the filled 2s shell.

Our theoretical calculations confirmed these observations. The global minimum search revealed that the endohedral cages with T_d symmetry either represent the global minimum structure for the doped clusters ($ZnAu_{16}^-$), or are within less than 0.1 eV from the calculated global minima ($AgAu_{16}^-$ and $InAu_{16}^-$). The simulated PES spectra of the four lowest-lying isomers of MAu_{16}^- (M = Ag, Zn, In) are shown in Figs. 4.5–4.7, respectively. For $AgAu_{16}^-$, the lowest energy structure we obtained is a C_{3v} endohedral cage (Fig. 4.5), which is only slightly distorted from T_d symmetry. However, its simulated PES spectrum shows an additional peak in between the energy gap region, inconsistent with the experimental data. The endohedral T_d cage is the third lowest-lying isomer, about 0.066 eV above the C_{3v} structure. Importantly, the simulated spectrum of the T_d isomer, featuring the characteristic doublet peaks (labeled t_2 and e), agrees well with the experimental data. It should be pointed that the Jahn-Teller splitting due to detachment from the t_2 orbital cannot be reproduced from our calculations because the geometry was fixed in calculating the first VDE. Considering the uncertainty of the DFT energies for such systems, we conclude that the T_d structure should be assigned as the global minimum for $Ag@Au_{16}^-$. Note that the recent theoretical study[189] that suggested an exohedral $AgAu_{16}^-$ is not supported by the experiment or the current calculation. Our DFT results show that the exohedral $AgAu_{16}^-$ structure is a higher energy isomer and gives a very different PES spectrum that does not agree with the experimental one.

For $ZnAu_{16}^-$, the global minimum structure we found is the endohedral T_d cage (Fig. 4.6). Its simulated PES spectrum is in good agreement with the experiment; note again that the Jahn-Teller splitting of the t_2 orbital cannot be reproduced in our current calculation. For $InAu_{16}^-$, the lowest energy structure from our calculations is also a C_{3v}

cage (Fig. 4.7), similar to $AgAu_{16}^-$. However, the T_d isomer is only 0.01 eV higher in energy and yields a simulated spectrum in better agreement with the experiment. Thus, we conclude that the true global minimum of $InAu_{16}^-$ should be the endohedral T_d structure. The calculated first VDEs of the T_d cages for all the three doped clusters are also in good agreement with the experimental data (Table 4.2). The overall agreement between the experimental and theoretical results provides considerable credence for the endohedral structures for $M@Au_{16}^-$ (M = Ag, Zn, In), in which the dopant atom induces little structural distortion to the parent golden cage.

The observation of the electron filling patterns in the current series of doped $M@Au_{16}^-$ clusters is very intriguing. It provides experimental evidence that the metal dopant does not significantly alter the electronic or atomic structure of Au_{16}^-, but simply transfers its valence electrons to the golden cage in MAu_{16}^-, which can be viewed approximately as $Ag^+@Au_{16}^{2-}$, $Zn^{2+}@Au_{16}^{3-}$, and $In^{3+}@Au_{16}^{4-}$. The current work suggests a convenient means to systematically tune the electronic, hence the chemical and optical, properties of the golden cage by endohedral doping, while maintaining its cage structure. For example, previous experiments have demonstrated that, unlike other even-sized small gold cluster anions, Au_{16}^- is very inert toward O_2 chemisorption owing to its anomalously high electron affinity (~ 4 eV) which prevents the electron transfer to oxygen molecule.[191-192] We expect that, with the reduced electron affinity (~ 3.4 eV) by doping, $Zn@Au_{16}^-$ should be reactive to O_2, whereas $Cu@Au_{16}^-$ and $Ag@Au_{16}^-$ would be similar to Au_{16}^- and unreactive to O_2. Those doped golden cage clusters with tunable chemical reactivities provide ideal model systems for the catalysis study of nanogold.

4.4. M@Au_{16}^- (M = Si, Ge, Sn) Clusters

As we have discussed in section 3.2, group-14 atoms are strongly covalent elements and the structures of group-14 atom-doped small gold clusters MAu_x^- are dominated by the strong local M-Au interactions.[164] It would be interesting to see if a group-14 atom (Si, Ge or Sn) can be endohedrally doped inside the golden cage. Although a previous theoretical study suggested that both Si and Al can be doped into the Au_{16} cage with little structural distortion to the parent symmetry,[178] no experimental evidence has been reported. In this section, we present a joint PES and theoretical study of doping a group-14 atom into the Au_{16}^- cage cluster.[193] We find surprisingly that the lowest-energy structures of MAu_{16}^- (M = Si, Ge, Sn) are no longer in the form of endohedral structures. Instead, the dopant atom is found to be either exohedral (Ge, Sn) or becomes a part of the gold cage (Si), in which the initial cage structure of the parent cluster is significantly distorted by local M-Au interactions, similar to that in the smaller doped gold clusters.[164]

The doped gold clusters MAu_{16}^- (M = Si, Ge, Sn) were produced by laser vaporization of an Au/Si, Au/Ge and Au/Sn composite disk target containing about 2% Si, 2% Ge and 2.5% Sn, respectively. Again the concentration of the dopant materials in the target was carefully adjusted to minimize the multi-atom doping in the $M_xAu_y^-$ clusters and provide the MAu_y^- series as the dominant doped species in order to achieve clean mass-selection for the MAu_{16}^- clusters. The PES spectra of MAu_{16}^- have been obtained at two detachment photon energies, 193 nm and 266 nm, which are presented in Figures 4.8 and 4.9 respectively. In Figure 4.8, simulated PES spectra of assigned structures for MAu_{16}^- (M = Si, Ge, Sn) are also shown for comparison.

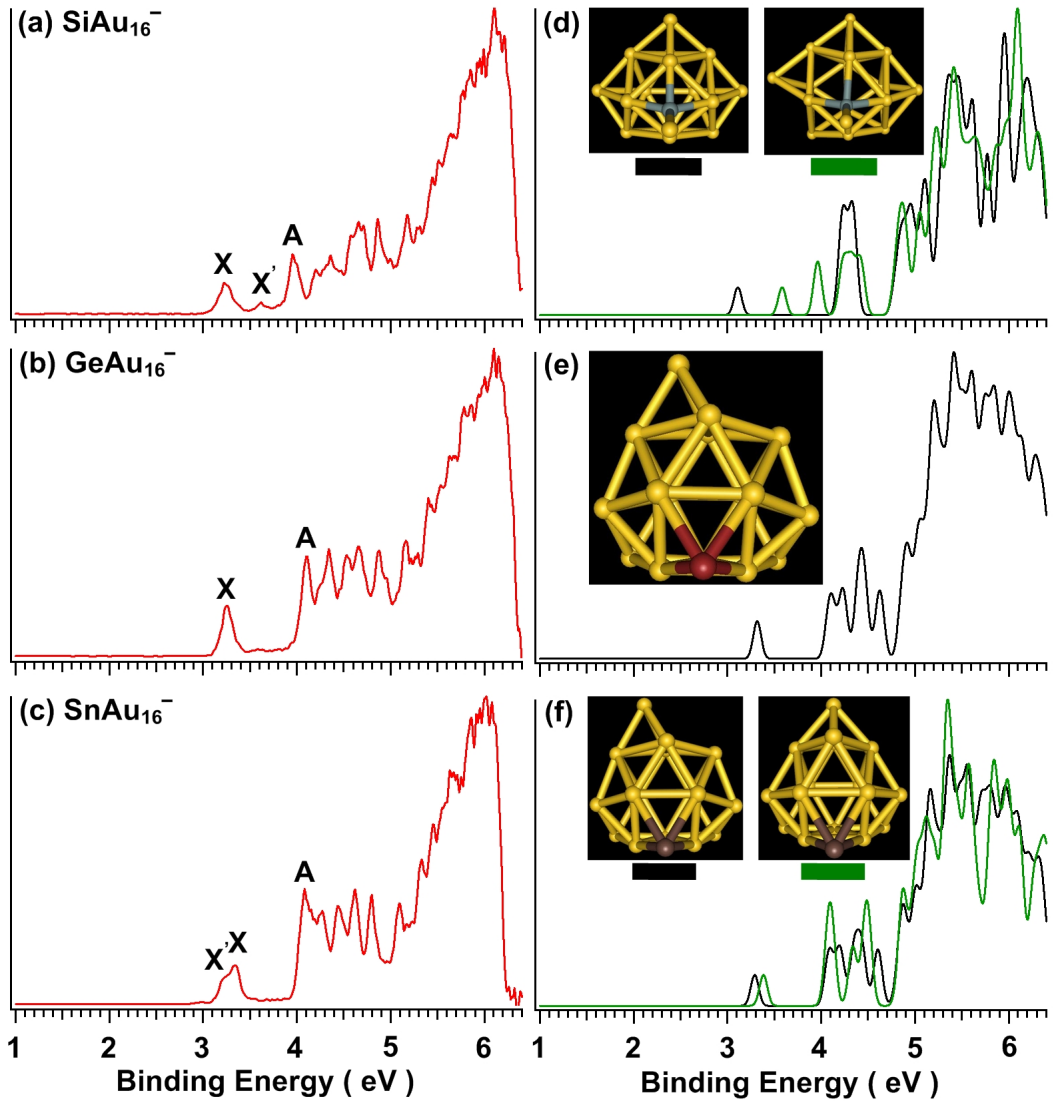

Figure 4.8 The experimental (left panel) and simulated PES (right panel) of $SiAu_{16}^-$, $GeAu_{16}^-$ and $SnAu_{16}^-$. The inset shows the global minimum and a low-lying isomer (for $SiAu_{16}^-$ and $SnAu_{16}^-$). The dopant atoms are shown in color (Si in grey, Ge in red, and Sn in brown).

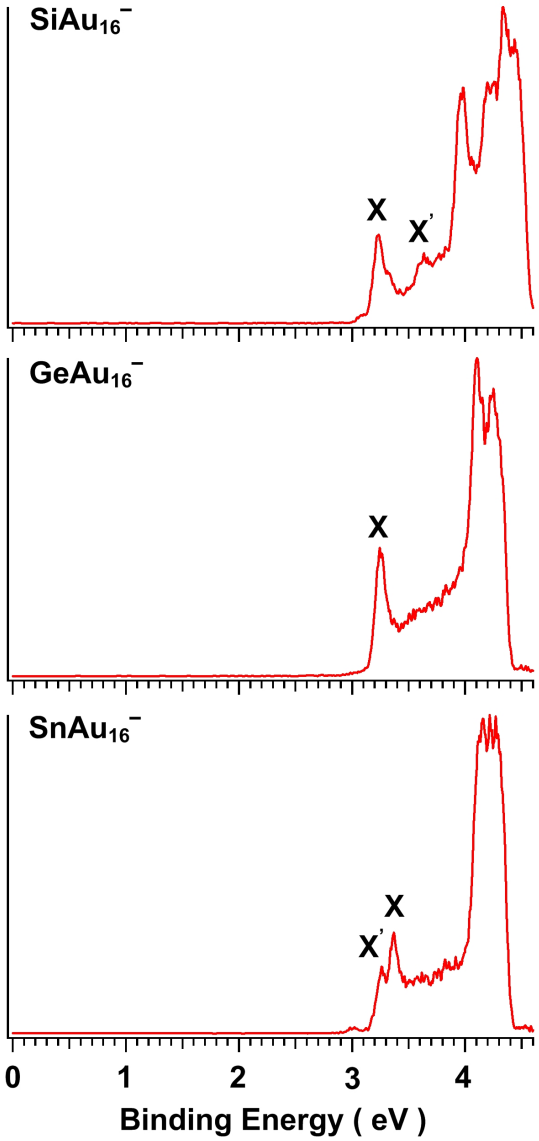

Figure 4.9 Photoelectron spectra of $SiAu_{16}^-$, $GeAu_{16}^-$ and $SnAu_{16}^-$ at 266 nm (4.661 eV).

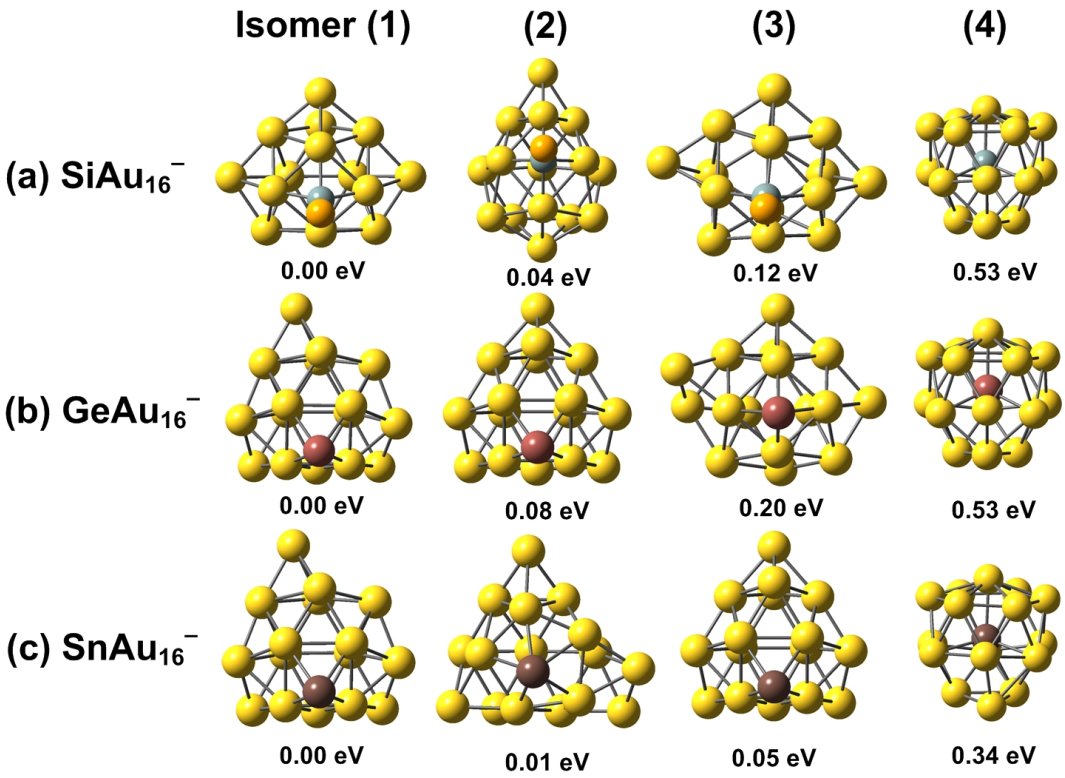

Figure 4.10 The top-three lowest-lying isomers (1 – 3) plus one endohedral isomer (4) of (a) $SiAu_{16}^-$ (b) $GeAu_{16}^-$, and (c) $SnAu_{16}^-$, and their relative energies at PBEPBE/LANL2DZ level of theory. The dangling Au atom is represented in orange in the case of the $SiAu_{16}^-$ clusters.

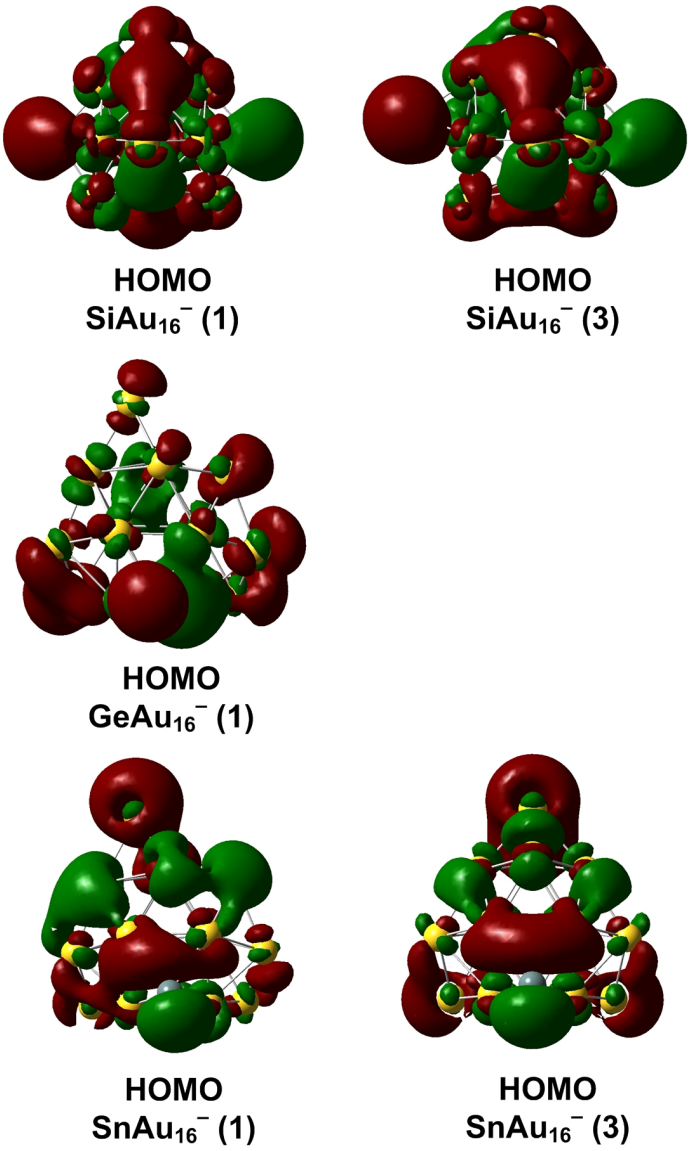

Figure 4.11 The HOMOs of the selected low-lying isomers of MAu_{16}^-.

Table 4.3 Relative energies, experimental ADE, VDE, and calculated VDE of the lowest-energy isomers of MAu_{16}^-. All calculations were at the PBEPBE/LAN2DZ level of theory. All energies are in eV.

Isomer	Rel. Energies	ADE (exp)[a]	VDE (exp)[a]	VDE (theo)
$SiAu_{16}^-(1)$ (C_s)	0.00	3.20 (5)	3.23 (3)	3.11
$SiAu_{16}^-(3)$ (C_1)	0.12	–	3.63 (3)	3.58
$GeAu_{16}^-(1)$ (C_1)	0.00	3.21 (4)	3.26 (3)	3.31
$SnAu_{16}^-(1)$ (C_1)	0.00	3.21 (4)	3.26 (3)	3.28
$SnAu_{16}^-(3)$ (C_s)	0.05	3.30 (6)	3.37 (3)	3.37

[a] The numbers in the parentheses represent the uncertainty in the last digit.

As shown in Figure 4.8, The PES spectra among three doped clusters are somewhat similar to each other, each revealing a fairly large HOMO-LUMO gap (X-A gap). This suggests that the doped clusters may have similar structures. Remarkably, the abovementioned spectral features as the signature of the T_d cage (originated for the t_2 and e orbitals,[190] see also section 4.3) are no longer seen in the spectra of the gropu-14 atom doped species. In stead, the transition bands in between ~ 4 and 5 eV for the spectra of MAu_{16}^- (M = Si, Ge, Sn) are featured with more complicated patterns (Figure 4.8), indicating that the high fold degeneracy of the t_2 and e orbitals are further split, hence the T_d symmetry is likely distorted significantly in MAu_{16}^-. The spectrum of $SiAu_{16}^-$ (Figure 4.8a) shows a weak feature (X') in the HOMO-LUMO gap region, suggesting the presence of a minor isomer. The first feature in the spectrum of $SnAu_{16}^-$ (Figure 4.8c) displays a doublet feature (also see Figure 4.9), which is also an indication of another isomer (see below). The X band represents the ground state transition, yielding adiabatic and vertical detachment energies (ADE/VDE) of 3.20/3.23, 3.21/3.26, and 3.30/3.37 eV, respectively, for M = Si, Ge, and Sn) (Table 4.3).

To affirm if the group-14 atoms can be doped into the Au_{16}^- cage, our theoretical collaborators carried out unbiased basin-hopping (BH) searches for the global-minimum structures of MAu_{16}^- (M = Si, Ge, Sn). Surprisingly, our global-minimum search shows that the Au_{16}^- clusters doped with a group-14 atom are exohedral in nature with significant distortions to the parent cage (Figure 4.8). The structures with endohedral doping are all higher-lying isomers (Figure 4.10). The VDEs of all the lowest-energy isomers are in very good agreement with the experiment (Table 4.3). The simulated spectrum for the global minimum of $GeAu_{16}^-$ agrees well with the experimental spectrum

(Figure 4.8b, e). For the Si- and Sn-doped clusters, there is experimental evidence of an additional isomer present in the PES spectra (Figure 4.8a, c), which is indeed borne out in the simulated spectra (Figure 4.8d, f). The similarities in the structures of the lowest-energy isomer with the Ge and Sn dopants are reflected in their similar PES patterns (Figure 4.8b, c). For $SnAu_{16}^-$, isomers 1 and 3 give almost identical simulated spectra; isomer 3 seems to contribute significantly to the experimental spectra and is competing for the global minimum. For $SiAu_{16}^-$, the two low-lying isomers are quite different from those of $GeAu_{16}^-$ and $SnAu_{16}^-$, in that, the Si dopant is capped by an extra Au atom that is not a part of the cage but dangling over the Si atom. Isomer 1 for $SiAu_{16}^-$ is the main species, while isomer 3 gives rise to the minor feature (X', Figure 4.8a and Table 4.3). Note that, a simultaneously published theoretical work by Sun *et al.*[187] located a similar structure as isomer 1 for $SiAu_{16}$, consistent with our study.

The dangling Au atom atop Si in $SiAu_{16}^-$ is reminiscent of the Au/H analogy discovered in the $SiAu_4$ cluster[127] as well as the $SiAu_8^-$[164] cluster that discussed in chapter 3. We found recently that this Au/H analogy does not exist in $GeAu_4$ and $SnAu_4$, since the latter have square-pyramidal structures.[162] Such chemical difference between Si and Ge/Sn is also reflected in the MAu_{16}^- clusters; A closer look at the structures of $GeAu_{16}^-$ and $SnAu_{16}^-$ reveals that the local geometry around the Ge/Sn atom is nearly square-pyramidal (Figure 4.8), just as that of $GeAu_4$ and $SnAu_4$. On the other hand, the local structure around Si in $SiAu_{16}^-$, with dangling Au atom atop it, is also very similar to that of the $SiAu_5$[163] and $SiAu_8^-$[164] clusters. This reflects that the local structures in the MAu_{16}^- clusters are dominated by the strong M-Au covalent bonding, similar to that in MAu_4 and

other small group-14 atom-doped gold clusters. It is such strong covalent interaction that distorts the cage structure of the parent Au_{16}^- cluster.

Molecular orbital analyses offer further insight into the local interactions between the dopant and Au in MAu_{16}^- clusters. The dangling Au atom in $SiAu_{16}^-$, besides giving a unique geometry to the doped cluster, has a significant contribution to the HOMO of the doped cluster, resulting in strong bonding with the Si atom (Figure 4.11). The HOMO pictures of the Ge- and Sn-doped clusters show significant contribution from both the dopant atom and the cage, indicating strong bonding between them. The local electron density distribution around the group-14 atom resembles the molecular orbital pictures obtained in the cases of $GeAu_4^-$ and $SnAu_4^-$.[162] Apparently, the strong interactions between Au and the group-14 atoms (particularly as in the diatomic molecule MAu) lead to reconstruction of the parent Au_{16}^- cage structure in the global minima of MAu_{16}^-.

The neutral MAu_{16} clusters all possess 20 valence electrons and are closed shell species, as evident from the sizable HOMO-LUMO gaps of ~ 0.6–0.8 eV observed in their PES spectra (Figure 4.8). However, because of the strong M-Au local interactions, the MAu_{16} clusters may no longer be viewed as 20-electron closed-shell systems in the sense of the electron-shell model. They should rather be considered as 16-electron systems because four electrons are needed for the local M-Au bonding, and there is no charge transfer from the dopant atom (Si, Ge, Sn) to the gold cluster. Hirshfeld charge analyses on the neutral clusters show that all dopant atoms entail a small negative charge in MAu_{16}, consistent with the description that MAu_{16}^- clusters are not charge transfer complexes but covalently bonded systems.

To summarize, in this section we studied the group-14 atom-doped golden cage clusters, MAu_{16}^- (M = Si, Ge, Sn), and found that their global minima do not possess the endohedral structures. The global minima are dominated by the strong M-Au local interactions reminiscent of the MAu_4 clusters. In particular, a dangling Au atom is observed in the low-lying isomers of $SiAu_{16}^-$ which confirms the Au/H analogy found earlier in small Si-Au mixed clusters.[127,164] Our results show that the nature of the dopant-Au local interactions is the key factor in determining if a given atom can be dope inside the golden cages.

4.5. M@Au_{16}^- (M = Fe, Co, Ni) Clusters

Finally, I present our studies on the magnetic doping of the golden cage cluster. The local magnetic properties of dilute magnetic impurities in nonmagnetic hosts have been addressed with great experimental and theoretical efforts in the past decades.[194-199] Atomic clusters provide a unique medium for exploring local magnetism, as the cluster size, the number of valence electrons, and the local structures can be readily controlled and varied.[200-205] In particular, a single magnetic atom trapped in a metallic cage would be an interesting system and an ideal molecular model for dilute magnetic alloys.[206-210] The Au_{16}^- cluster with the large internal volume[105] provides the possibility to encapsulate a transition metal atom to form magnetic clusters. Here we report a study on doping the Au_{16}^- cage with transition-metal atoms, MAu_{16}^- (*M* = Fe, Co, Ni). We use photoelectron spectroscopy (PES), collaborated with the trapped ion electron diffraction (TIED) experiments and density functional theory (DFT) calculations in the current study. The TIED technique probes the atomic structures of size-selected cluster ions,[61,211] and PES is

a powerful technique to probe the electronic structure of clusters, which is also sensitive to their geometries. The combination of these experimental techniques with DFT calculations affords a comprehensive understanding of the structural, electronic, and magnetic properties of the transition-metal-atom-doped golden cages. We found that the three magnetic atoms (Fe, Co, Ni) are all doped inside the golden cage, but with significant distortions to the parent cage structure. The dopant atoms maintain their atomic-like *d* configurations in $M@Au_{16}$, while their 4*s* electrons can be viewed as transferred to the golden cage.[212]

The bimetallic cluster anions MAu_{16}^- (*M* = Fe, Co, Ni) were produced either by a magnetron sputtering source for TIED or by a laser vaporization source for PES using composite *M*/Au target disks. We assume that the two different cluster sources used in TIED and PES experiments give similar ion ensembles. For theoretical part, our collaborators carried out basin-hopping (BH) global minimum searches for both high spin and low spin states for each species. For all the three MAu_{16}^- clusters, our global minimum searches found many low-lying isomers very close in energies and with subtle structural differences. The candidate structures for each cluster are obtained by comparing both experimental data with the corresponding DFT simulations, and at the same time the relative energies are also taken into consideration. For TIED experiments, a quantitative measurement of the agreement between experimental and simulated scattering functions is expressed in a weighted profile factor R_w,[212] where smaller R_w value corresponds to better agreement.

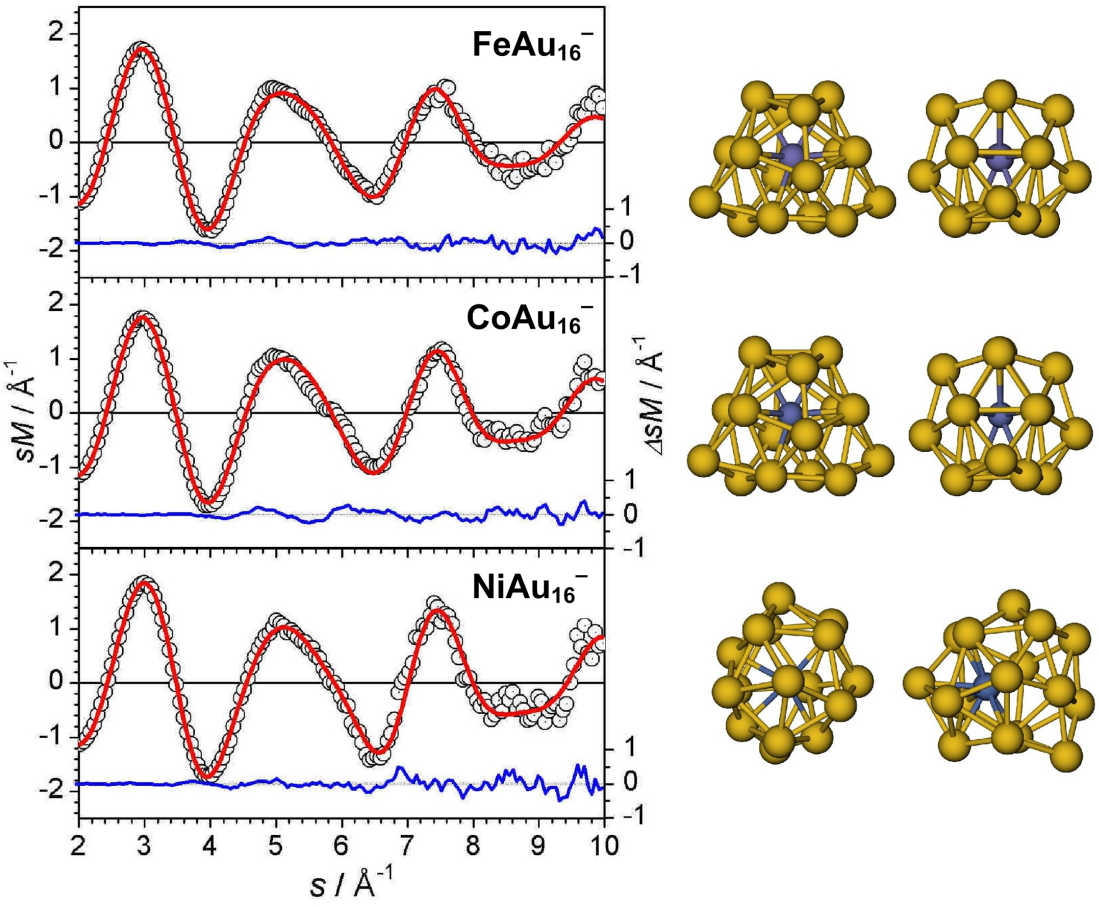

Figure 4.12 Modified experimental electron scattering functions (open circles) for $M\mathrm{Au}_{16}^-$ (M = Fe, Co, Ni) with the best fit (red line) using the structures shown on the right (two views rotated by 90°). The lower traces in each frame show the residuals.

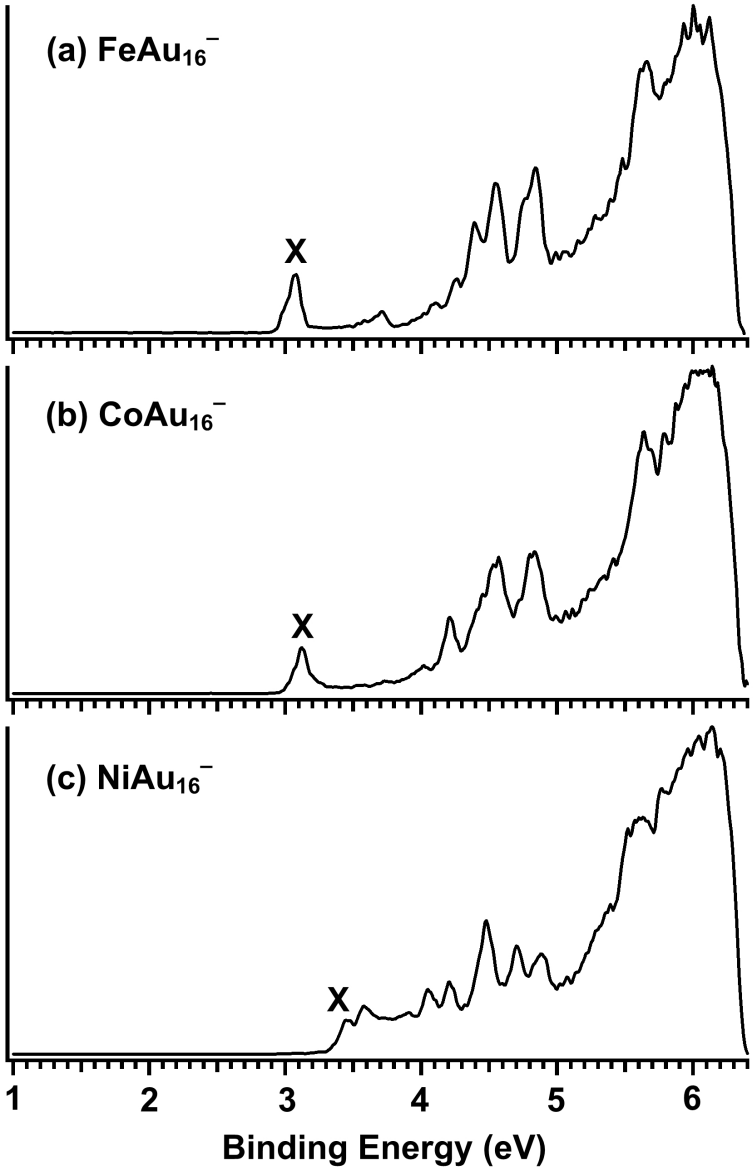

Figure 4.13 Photoelectron spectra of $M\mathrm{Au}_{16}^{-}$ (M = Fe, Co, Ni) at 193 nm (6.424 eV).

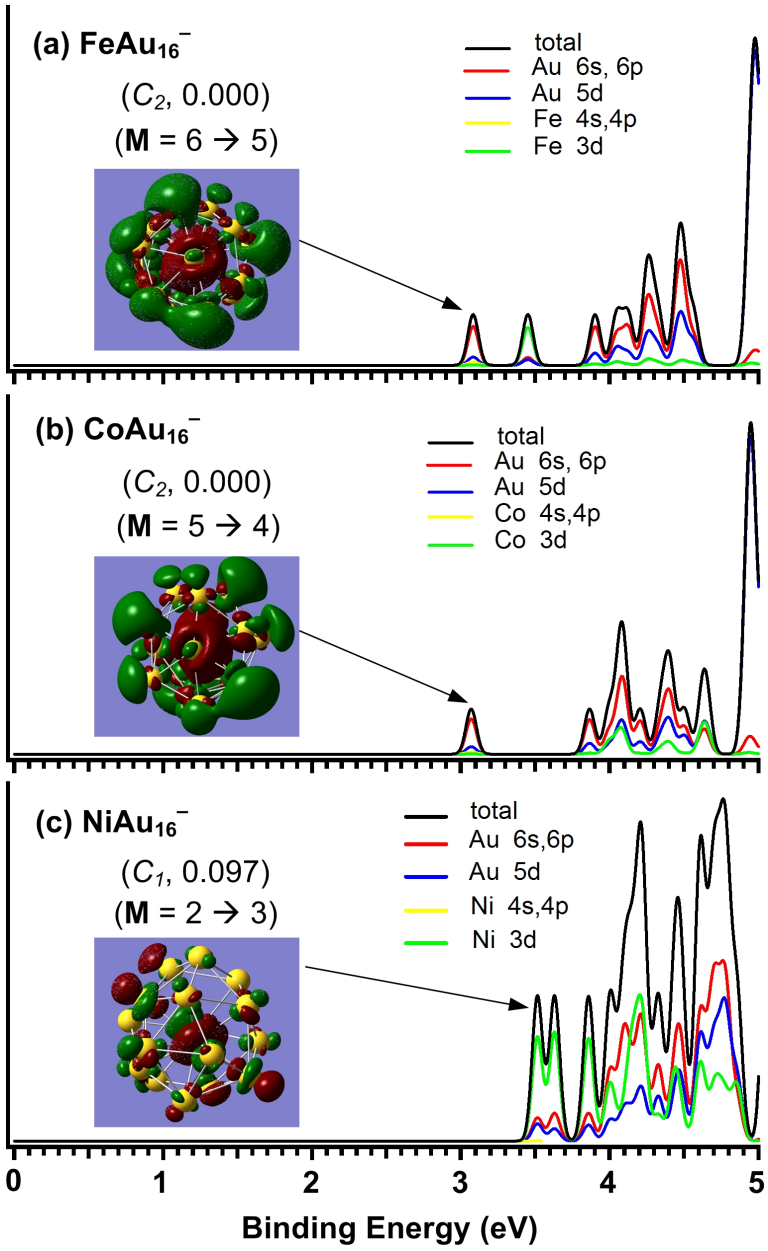

Figure 4.14 Simulated photoelectron spectra of $M\text{Au}_{16}^-$ (M = Fe, Co, Ni) for the structures shown in Figure 4.12. The symmetry and relative energy (in eV) are given in the parenthesis. **M** denotes the spin multiplicity from the anion to the neutral. The inset shows the highest occupied molecular orbital. Contributions from different atomic orbitals to the density of states are also shown.

Table 4.4 The experimental vertical detachment energies (VDE) of MAu_{16}^- (M = Fe, Co, Ni) compared to calculated values.

	VDE (eV)	
	Exp.	Theo.
$FeAu_{16}^-$ (C_2)	3.07 ± 0.03	3.08
$CoAu_{16}^-$ (C_2)	3.11 ± 0.03	3.07
$NiAu_{16}^-$ (C_1)	3.46 ± 0.04	3.51

Fig. 4.12 displays the TIED data fitted using the best candidate structures for $M\mathrm{Au}_{16}^-$ (M = Fe, Co, Ni) that also agree well with the PES data, as will be discussed below. For FeAu_{16}^-, the lowest energy structure is of C_2 symmetry (Fig. 4.12), which is endohedral in nature, but with some appreciable distortion to the parent tetrahedral (T_d) Au_{16}^- cage. Of all the low-lying structures the simulated scattering function of the C_2 isomer fits the TIED data best (R_w = 2.7%). The endohedral structure with T_d symmetry shows a much larger R_w value (8.0%) and can be ruled out as a major contributor to the cluster ensemble probed. Nevertheless, a small contribution from the T_d-like structure is possible, because a mixture fit by adding ~20% T_d isomer leads to a slight improvement in the R_w value (2.0%). The lowest energy structure found for CoAu_{16}^- is very similar to FeAu_{16}^-, i.e. a C_2 structure (Fig. 4.12), which is among the structures giving the best fit (R_w = 3.3%) to the TIED data. However, several other low-lying endohedral structures can also fit the TIED data well. In particular, a C_1 structure (0.13 eV higher in energy) similar to that of NiAu_{16}^- (see below) gives a very good R_w value of 2.8%. Contributions from different isomers are also probable, because mixtures of the C_2 or the C_1 structure with the T_d structure in the ratio of 0.7/0.3 or 0.8/0.2 lead to improved R_w values of 2.5% or 2.0%, respectively. However, we assign the C_2 isomer as the main contributor for CoAu_{16}^-, because it is the lowest energy structure from our calculation and it also gives better agreement with our PES data (see below). For NiAu_{16}^-, the structure giving the best agreement between experimental and simulated scattering functions is a C_1 structure (R_w = 2.4%), as shown in Fig. 4.12. The C_2 structure similar to FeAu_{16}^- or CoAu_{16}^- gives an R_w of 3.4% and a mixture fit of both does not significantly reduce the R_w value. Both structures are slightly higher lying isomers, 0.10 eV and 0.14 eV, respectively, above the

lowest energy structure which itself can be ruled out as a major component because of its high R_w value (9.1%). Again the tetrahedral cage structure (R_w = 11%) can be ruled out as a major contributor.

The above structure assignments are corroborated and complemented by comparison between the experimental and simulated PES spectra. Fig. 4.13 shows the experimental PES spectra of $M\text{Au}_{16}^-$ (M = Fe, Co, Ni) at 193 nm. The spectra of FeAu_{16}^- and CoAu_{16}^- are similar, both featuring a low binding energy peak at ~3 eV (X) followed by an energy gap, a group of well-resolved peaks between 4-5 eV, and more congested Au 5d band beyond 5.5 eV. The spectrum of NiAu_{16}^- is very different and much more congested in the low binding energy range compared to that of FeAu_{16}^- and CoAu_{16}^-, suggesting that the structure of NiAu_{16}^- may also be very different as born out from the above comparison of TIED and DFT calculations. The PES spectra all seem to contain weak diffuse signals, more clearly in the cases of FeAu_{16}^- and CoAu_{16}^- following the X band (Fig. 4.13a, b), which may come from weakly populated isomers consistent with the TIED data. The first VDE for $M\text{Au}_{16}^-$ is given in Table 4.4.

It is informative to compare the current PES data with those of CuAu_{16}^- and ZnAu_{16}^-.[181,190] Both Cu and Zn have a closed 3*d* shell and the doped clusters possess endohedral structures with little distortion to the parent golden cage. Cu@Au_{16}^- is a closed-shell 18-electron system, in which the Cu 4*s* electron is transferred to the gold cage and it can be viewed as $\text{Cu}^+@\text{Au}_{16}^{2-}$.[181] The low binding energy range of its PES spectrum between 4-5 eV consists of a characteristic three-peak feature due to the t_2 and e valence molecular orbitals in the T_d cluster.[178] Zn@Au_{16}^- is a 19-electron system, in which the two 4*s* electrons of Zn are transferred to the golden cage. The extra electron in

the anion enters a new electron shell, resulting in a low binding energy feature much separated from the three-peak feature derived from the t_2 and e orbitals. The PES spectra of $FeAu_{16}^-$ and $CoAu_{16}^-$ are reminiscent of the $Zn@Au_{16}^-$ spectrum. In particular, the low binding energy peak (X) and the ensuring energy gap are very similar to what was observed in the spectrum of $Zn@Au_{16}^-$, suggesting that the two 4*s* electrons of Fe ($3d^6 4s^2$) and Co ($3d^7 4s^2$) are also transferred to the golden cage and the extra electron in the anion enters in a new electron shell on the golden cage. The more complex spectral features between 4-5 eV suggest lifting of the degeneracy, and thus structural distortions to the parent cage, as well as possible contributions from the open 3*d* shell. The more complex PES spectrum of $NiAu_{16}^-$ suggests a much more significant distortion to the parent gold cage. In particular, the missing low binding energy peak (Fig. 4.13c) implies that the extra electron in the $NiAu_{16}^-$ anion enters a 3*d* orbital of the Ni dopant rather than a new shell on the gold cage, most likely due to the fact that in Ni the $3d^8 4s^2$ and $3d^9 4s^1$ configurations are nearly degenerate. All the above PES observations are consistent with the structural information derived from the TIED data.

The simulated PES spectra for $M@Au_{16}^-$ (Fig. 4.14) support the above interpretations and allow a better understanding of the experimental data. For $FeAu_{16}^-$, among several low-lying isomers, the simulated spectrum of the C_2 structure (Fig. 4.14a) agrees best with the experimental spectrum. Specifically, the weak peak observed at ~3.7 eV (Fig. 4.13a) in the gap region is well reproduced in the simulated spectrum by an Fe 3*d*-derived band (Fig. 4.14a). The first detachment band (X) is indeed due to an Au 6*s*/*p* type orbital (also see inset of Fig. 4.14a), similar to the case of $Zn@Au_{16}^-$. For $CoAu_{16}^-$, several low-lying isomers give similar simulated spectra, but the C_2 structure (Fig. 4.14b)

gives the best overall fit to the experimental PES data. Similar to $Fe@Au_{16}^-$ and $Zn@Au_{16}^-$, the first PES feature in $CoAu_{16}^-$ is also due to an Au 6*s*/*p* derived orbital (see inset of Fig. 4.14b). For $NiAu_{16}^-$, only the C_1 structure gives a simulated spectrum (Fig. 4.14c), which agrees well with the experiment, validating the TIED structural assignment. Importantly, the first detachment feature from $NiAu_{16}^-$ indeed comes from a Ni 3*d* derived orbital, as shown in the inset of Fig. 4.14c. The calculated first VDE is also in good agreement with the experimental data, as compared in Table 4.4. Overall, the comparison of the simulated and experimental PES results lends considerable further support to the structures obtained for the three transition-metal-doped golden cages. The transition metal dopants are clearly endohedral in nature, albeit the parent golden cage is significantly distorted, in particular, in the case of Ni.

Our previous studies show that the dopant-Au interactions are critical in determining the structures of the doped golden cages. Cu and Zn, which have closed 3*d* shells, primarily donate their 4*s* electrons to the cage, forming charge-transfer complexes with very little distortions to the cage.[181,190] Dopants, such as Si or W, have strong interactions with Au and they distort the golden cages and form other new types of structures.[187-188,193] The open 3*d* configurations for Fe, Co, and Ni suggest that they may have more significant interactions with Au, leading to the observed structural distortions in the doped $M@Au_{16}^-$ clusters. Indeed, the decomposed density-of-states spectra in Fig. 4.14 show that the 3*d* orbitals of the dopant atoms have considerable hybridization with the host golden cage. This is particularly pronounced for $Ni@Au_{16}^-$, consistent with its much distorted C_1 structure, in which the Ni atom appears to move to one side of the cage and interacts with fewer Au atoms (Fig. 4.12).

Interestingly, although there is considerable interaction between the transition metal atoms and the host gold cage, the 3*d* states of the dopant atoms remain largely localized and the atomic-like magnetism is maintained in the doped clusters. We found that $Fe@Au_{16}^-$ (spin multiplicity **M** = 6) and $Co@Au_{16}^-$ (**M** = 5) have high spins, while $Ni@Au_{16}^-$ has a lower spin (**M** = 2), consistent with the stronger Ni-cage interactions. Mulliken atomic spin density analyses show that the spin densities are mainly located on the central dopant atom for all three doped clusters. The bonding in the doped cluster anions can be viewed as an Au_{16}^{3-} interacting with a Fe^{2+}/Co^{2+} core or Au_{16}^{2-} interacting with a Ni^+ core. The neutral $M@Au_{16}$ clusters can all be described as $M^{2+}@Au_{16}^{2-}$ (*M* = Fe, Co, Ni), where the two 4*s* electrons are transferred to the cage and the dopant possesses d^6, d^7 and d^8 valence configurations, respectively, exactly like that in the atoms. Thus, the current work shows that the Au_{16} hollow cage provides a much more flexible host to protect the spins of the dopant atom. We anticipate that many other transition metal atoms may be doped into the golden cage and maintain their local magnetic moments, forming a new class of endohedral golden cage clusters with varying magnetic properties.

4.6. Conclusion

The structural, electronic and magnetic properties of a series of single-atom-doped gold cage clusters have been characterized by joint experimental and theoretical studies. In conclusion, the nature of dopant-Au interactions is the key factor in determining the structures of the doped golden cages: Metal elements with completed *d* shells, like Cu, Ag, Zn and In can be doped inside the Au_{16}^- cage with little structural

distortions to its T_d symmetry. The interactions in such doped clusters are primarily charge transfer from the dopant atom to the gold cage. The transferred electrons from the dopant were shown to successively occupy the higher shell molecular orbitals of the golden cage, enabling a powerful way to systematically tune the electronic and chemical properties of the endohedral gold clusters while maintaining their geometric structures. We have shown that both 3d (Cu, Zn) and 4d (Ag, In) elements can be doped inside the golden cage despite their different atomic radii, in contrast to the recent theoretical predictions;[189] Though Si was first predicted to form endohedral structure with the gold cage,[178] our results show that group-14 atoms Si, Ge and Sn form strong covalent bonding with gold, which results in exohedral structures for the doped clusters MAu_{16}^- (M = Si, Ge, Sn) that is significantly distorted from the initial symmetry. In particular, a dangling Au motif is observed in the low-lying isomers of $SiAu_{16}^-$ which confirms the Au/H analogy found earlier in small Si-Au mixed clusters.[127,161] Finally, transition metal atoms with open *d* shell, like Fe, Co, Ni,[212] or W[188] can also be doped into the Au_{16}^- cage, but with considerable structural distortions due to the interactions of the open *d* electrons with the gold cage. The transition-metal-atom-doped golden cages can also be described as charge transfer complexes, in which the atomic-like magnetic moment of the dopant atom is maintained. Doping offers a powerful way to fine tune the electronic and magnetic properties of clusters. We anticipate that many other transition metal atoms may be doped into the golden cage, forming a new class of endohedral golden cage clusters with tailored chemical and physical properties.

CHAPTER FIVE

$C_XB_Y^-$: IN SEARCH OF HYPERCOORDINATE PLANAR CARBON IN CARBON-BORON CLUSTERS

5.1. Introduction

In organic chemistry, one of most established stereochemical concepts is that, due to its strong sp^3 hybridization, saturated carbon tends to bond with four ligands in a tetrahedral environment, as first recognized independently by J. H van't Hoff[213] and J. A. LeBel[214] in 1874. This concept of tetracoordinate tetrahedral carbon has served the community of organic chemists for more than one century, until in 1970 Hoffmann and co-workers first proposed the idea of tetracoordinate *planar* carbon.[215-216] Briefly, Hoffmann started with a theoretical planar methane molecule (CH_4), which is of course highly unstable, and proposed that by choosing appropriate ligand groups to replace the H atom, carbon could be potentially stabilized in the tetracoordinate planar geometry.[215] Following Hoffmann's pioneering work, extensive experimental and theoretical efforts have been made to search for so-called anti-van't Hoff/anti-LeBel molecules.[217-239] Two approaches to achieving this goal have been employed. The electronic approach involves selecting substituents that will electronically stabilize a planar disposition of the carbon bonds over the normal tetrahedral arrangement.[217-227] The alternative approach is based on using mechanical forces exerted by the surrounding ligands bound to the carbon atom.[228-236] Notably, the first experimental realization of pentaatomic planar tetracoordinate carbon was accomplished in 1999 in the form of Al_4C^- cluster anion[11] and

later in a series of similar clusters,[12,240-241] which confirmed earlier theoretical predictions.[220-221]

These experimental advances have stimulated a renewed interest in designing new tetracoordinate[242-249] and even hypercoordinate[250-262] planar carbon molecules. In particular, a series of carbon-boron clusters containing a hypercoordinate planar carbon with boron ligands proposed by Schleyer *et al.*[250-253,263] have attracted significant attention.[264-265] The three smallest carbon-boron clusters containing a hexa-, hepta-, and octa-coordinated planar carbon that have been proposed are the D_{6h} CB_6^{2-},[250] D_{7h} CB_7^-,[251] and C_{2v} (effectively D_{8h}) CB_8,[251] respectively. The stabilities of these clusters were rationalized in terms of aromaticities.[251-252] The planar CB_6^{2-} cluster with a hexacoordinate planar carbon has been touted as a "divining molecule" highlighted on the cover of a recent issue of *Chem. & Eng. News*.[264] Although none of these species is expected to be the global minimum on the potential energy surfaces, it has been suggested that they might be viable experimentally. However, despite the extensive theoretical interest, no experimental work has been tried for these proposed novel molecules. The reason is likely that both boron and carbon are very easily clustering, and the mass of 5 carbon atoms roughly overlaps that of 6 boron atoms. So to achieve a clean mass selection could be challenging.

Recently, during our laser vaporization experiments, we serendipitously observed a series of CB_x^- clusters, initially as impurities in the pure boron cluster beams (as will be described in section 5.2), which offers us the opportunity to experimentally probe those novel binary species. In this chapter, we present our joint PES and *ab intio* studies on a series of carbon-boron clusters (CB_7^-, CB_6^-, $C_2B_5^-$, CB_8^-) that associated with the

proposed hypercoordinate carbon. In contrast to the previous theoretical predictions, our results show that none of these clusters have a planar structure containing a hypercoordinate carbon. Molecular orbital and chemical bonding analyses have been carried out to understand the detailed chemical bonding and why carbon avoids hypercoordination in the wheel type boron-carbon mixed clusters. Rational strategies towards the design of hypercoordinate planar carbon molecules and planar chemical species with other hypercoordinated atoms are also proposed at the end.

5.2. CB_7^- Cluster

We start with the CB_7^- cluster which appeared to be the most abundant binary species in the mass spectrum, as will be discussed below. The B_8^{2-} cluster dianion has been previously shown to possess a D_{7h} planar wheel structure with a heptacoordinate boron.[16,266-267] The CB_7^- species is isoelectronic to B_8^{2-}, and the proposed D_{7h} CB_7^- with heptacoordinate carbon[251] can be viewed as replacing the center B^- ion in B_8^{2-} by a C atom. In the section, we present a serendipitous experimental observation of CB_7^-. It is investigated by photoelectron spectroscopy (PES) and *ab initio* calculations, which show that the observed species is a C_{2v} CB_7^-, in which the C atom replaces a B^- ion at the rim, instead of at the center, of the D_{7h} B_8^{2-} molecular wheel.[268] The D_{7h} structure with heptacoordinate carbon is very high in energy and extremely unfavorable.

The experiment was as usual performed using a laser vaporization cluster source. We have recently modified our cluster source by adding a 10 cm long, 3 mm diameter stainless steel tubing to enhance cluster cooling.[269] We were using boron clusters, which

we have investigated previously extensively,[16,266-267,270-275] to test the new cluster source conditions. A ^{10}B-enriched (98%) disk target containing a small amount of Au (to enhance the compressibility) was used as the laser vaporization target. The inner surface of the tubing was not purposely cleaned prior to the experiment. Under certain conditions, when the vaporization laser was not perfectly aligned, we noted that in addition to the pure boron clusters we were also able to produce clusters containing one or two carbon atoms, as shown in Figure 5.1. The carbon impurity most likely originated from impingement of the slightly misaligned vaporization laser beam on the inner surface of the stainless steel tubing. The trace amount of carbon contamination was ideal to produce the boron clusters doped with only one or two carbon atoms and the beam condition was stable and reproducible. Subsequently we also prepared a ^{10}B/C mixed target containing ~5% C and produced $C_yB_x^-$ clusters similar to that shown in Figure 5.1 but with slightly more abundance of clusters with two and three C atoms.

As seen in Figure 5.1, The CB_7^- cluster is particularly intense as an impurity species, with abundance as strong as the nearby pure B_x^- clusters, suggesting it is highly stale. Its photoelectron spectra at two detachment laser wavelengths are shown in Figure 5.2. The 193 nm spectrum reveals five well-separated transition bands (X, A-D) and the B band exhibits a short vibrational progression with a frequency of 1050 ± 60 cm^{-1}. The 355 nm spectrum shows a much better resolved X band, which seems to also display a short vibraitonal progression. However, the broad line width suggests that more than one low frequency modes may also be involved in the X band. The onset of the X band yields an adiabatic detachment energy or electron affinity for CB_7 as 2.99 ± 0.03 eV. The vertical detachment energies (VDE's) of the five bands are given in Table 5.1.

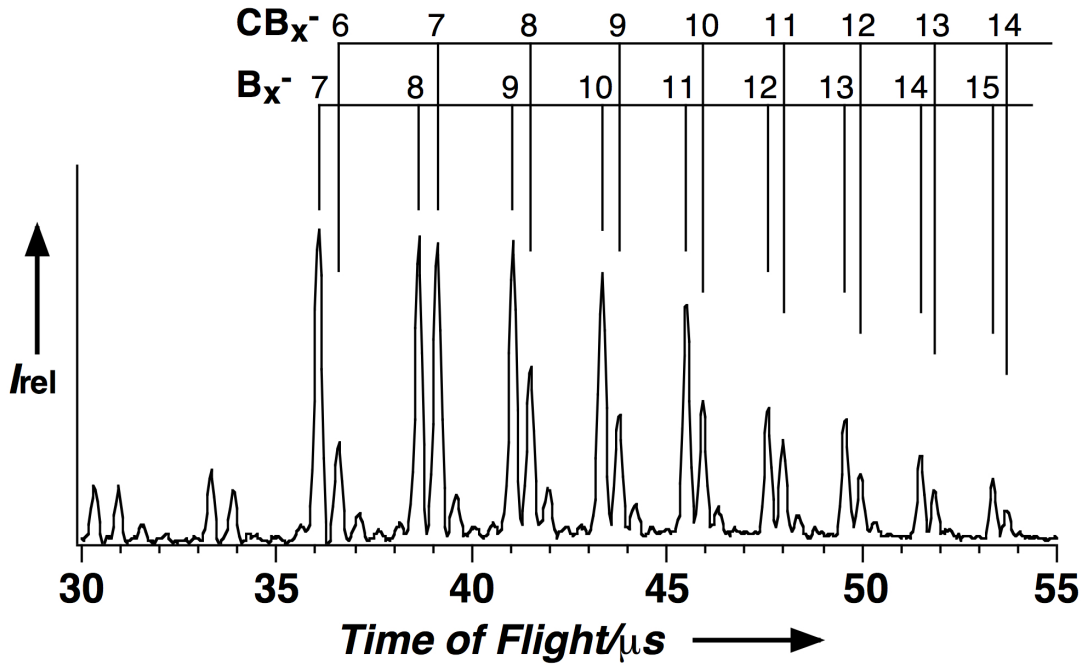

Figure 5.1 Mass spectrum of B_x^- and $C_yB_x^-$ clusters from a ^{10}B-enriched boron target. The B_x^- and CB_x^- series are marked. Weaker mass signals for the $C_2B_x^-$ and $C_3B_x^-$ series can also be seen.

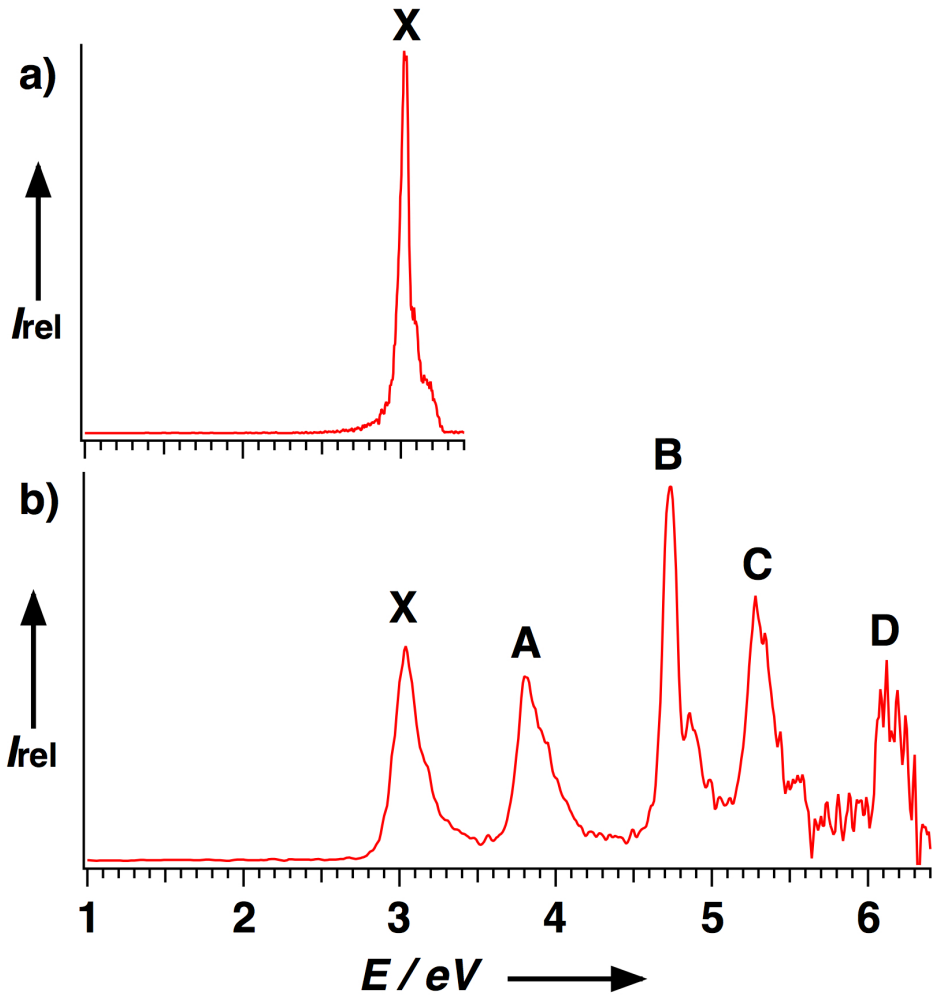

Figure 5.2 Photoelectron spectra of CB_7^- at a) 355 nm (3.496 eV) and b) 193 nm (6.424 eV).

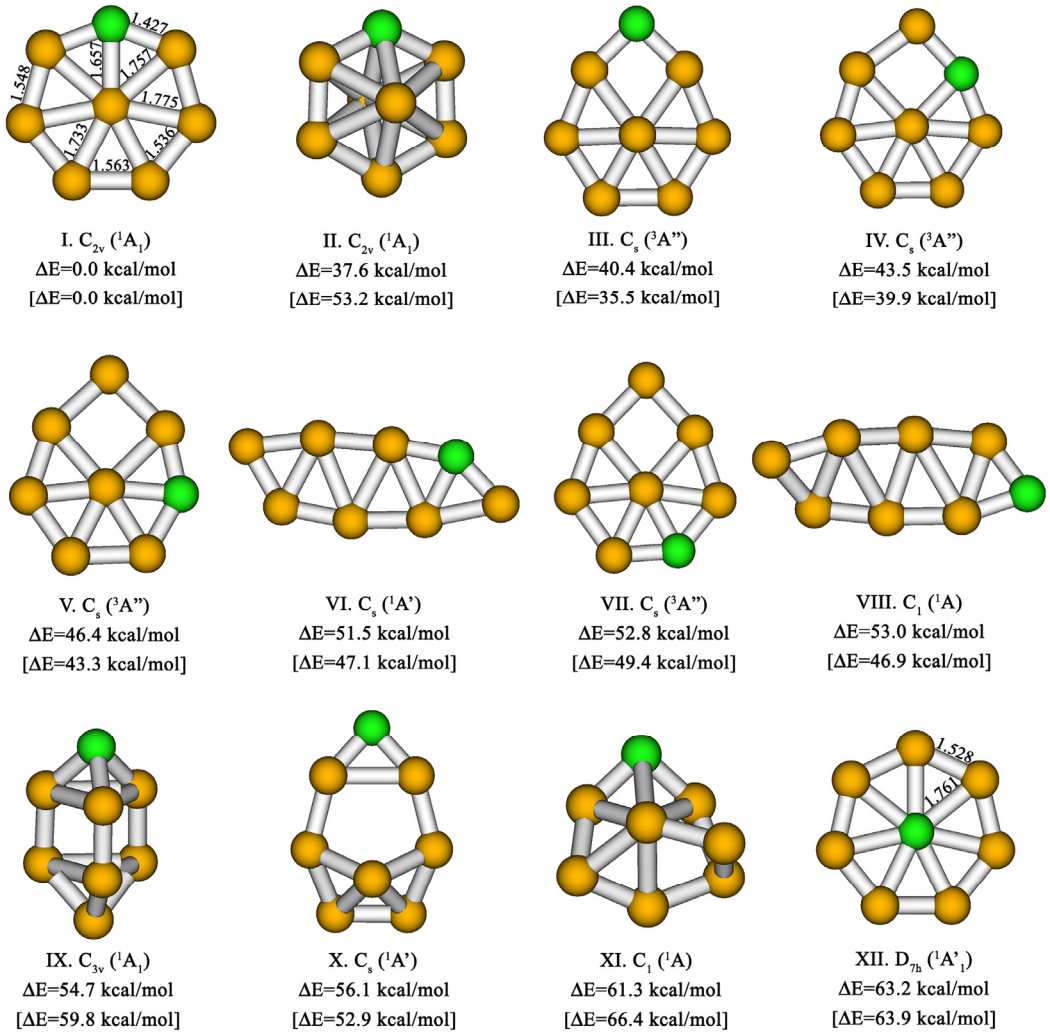

Figure 5.3 Optimized structures (B3LYP/6-311+G*) and relative energies (CCST(D)/6-311+G(2df)//B3LYP/6-311+G*) of CB_7^-. The relative energies in the brackets are at B3LYP/6-311+G* level.

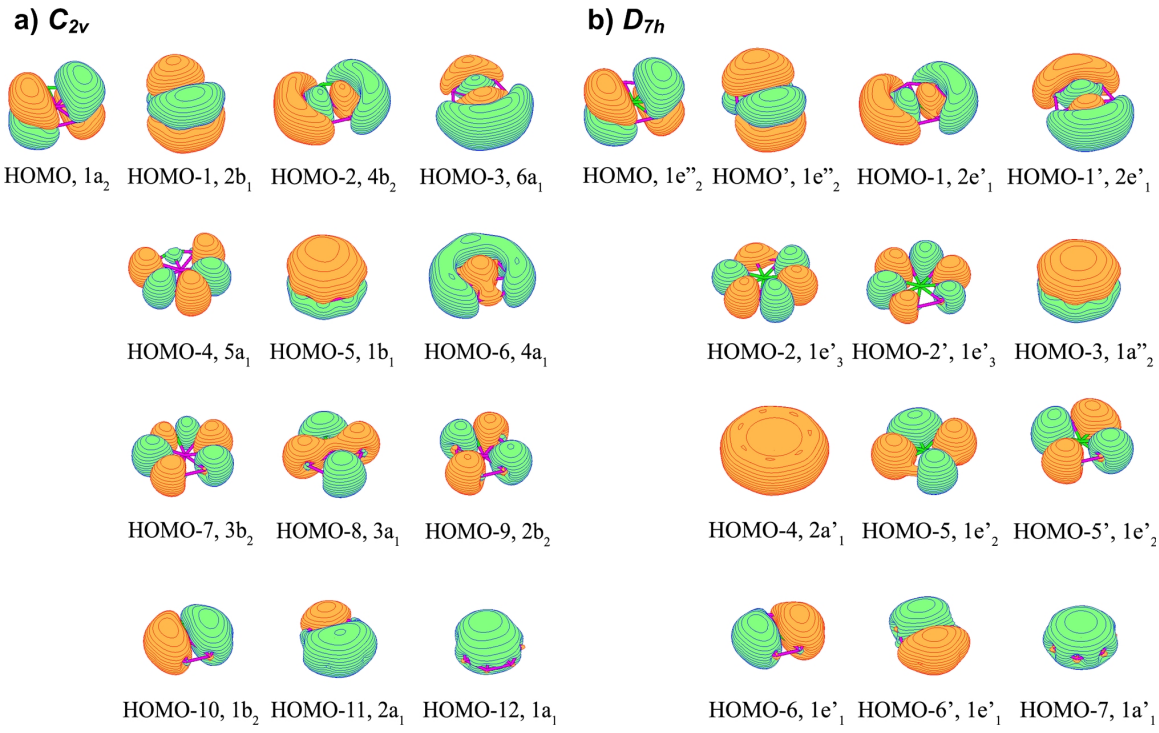

Figure 5.4 Comparison of the valence molecular orbitals of the (a) global minimum C_{2v} and (b) the high-lying D_{7h} isomer of CB_7^-.

Table 5.1 Comparison of the experimental VDEs of CB_7^- to the calculated values for the global minimum C_{2v} structure and the high-lying D_{7h} isomer. All energies are in eV.

Feature	VDE (exp.) [a]	Final State and Electronic Configuration	VDE (theo.) TD-B3LYP	VDE (theo.) OVGF [b]	VDE (theo.) ΔCCSD(T)[c]
		CB_7^- (C_{2v}, $^1A_1$)			
X [d]	3.03 (2)	$^2A_2$, $4a_1^2 1b_1^2 5a_1^2 6a_1^2 4b_2^2 2b_1^2 1a_2^1$	2.90	2.94 (0.89)	3.04
A	3.80 (3)	$^2B_1$, $4a_1^2 1b_1^2 5a_1^2 6a_1^2 4b_2^2 2b_1^1 1a_2^2$	3.79	3.81 (0.88)	3.86
B [e]	4.73 (3)	$^2B_2$, $4a_1^2 1b_1^2 5a_1^2 6a_1^2 4b_2^1 2b_1^2 1a_2^2$	4.66	4.80 (0.89)	4.78
C	5.28 (3)	$^2A_1$, $4a_1^2 1b_1^2 5a_1^2 6a_1^1 4b_2^2 2b_1^2 1a_2^2$	5.17	5.24 (0.88)	5.35
D	6.2 (1)	$^2A_1$, $4a_1^2 1b_1^2 5a_1^1 6a_1^2 4b_2^2 2b_1^2 1a_2^2$	6.10	6.29 (0.87)	
		CB_7^- (D_{7h}, $^1A_1$)			
		$^2E_2$", $2a_1'^2 1a_2"^2 1e_3'^4 2e_1'^4 1e_2"^3$	2.86	2.86 (0.89)	2.98
		$^2E_1'$, $2a_1'^2 1a_2"^2 1e_3'^4 2e_1'^3 1e_2"^4$	5.40	5.29 (0.89)	5.51
		$^2E_3'$, $2a_1'^2 1a_2"^2 1e_3'^3 2e_1'^4 1e_2"^4$	6.18	6.34 (0.87)	
		$^2A_2$", $2a_1'^2 1a_2"^1 1e_3'^4 2e_1'^4 1e_2"^3$	7.04	6.77 (0.65)	

[a] Numbers in parentheses represent the uncertainty in the last digit.
[b] VDEs were calculated at ROVGF/6-311+G(2df)//RCCSD(T)/6-311+G* level of theory. Values in parentheses represent the pole strength of the OVGF calculation.
[c] VDEs were calculated at UCCSD(T)/6-311+G(2df)//RCCSD(T)/6-311+G* level of theory.
[d] The adiabatic detachment energy of the X band or the electron affinity of CB_7 is 2.99 ± 0.03 eV.
[e] The vibrational frequency observed for this band is 1050 ± 60 cm^{-1}.

Our collaborators performed the global minimum search of CB_7^- using a gradient embedded genetic algorithm (GEGA) program.[276-277] A hybrid method known in the literature as B3LYP with the small split-valence basis sets (3-21G) is used for energy, gradient and force calculations. We reoptimized geometries and calculated frequencies for the lowest 12 isomers at the B3LYP/6-311+G* level of theory. The geometries of the C_{2v}, $^1A_1$ and D_{7h}, $^1A'_1$ isomers of CB_7^- are also recalculated using a coupled-cluster method with single, double, and noniterative triple excitations (CCSD(T)) based on the RHF formalism with the polarized split-valence basis sets (6-311+G*). Total energies of the twelve local minimum structures were also recalculated at the CCSD(T)/6-311+G(2df)//B3LYP/6-311+G* level of theory. The CB_7^- vertical electron detachment energies (VDE's) were calculated using the R(U)CCSD(T)/6-311+G(2df), the outer valence Green Function method (ROVGF/6-311+G(2df)) at the RCCSD(T)/6-311+G* geometries, and the time-dependent DFT method (TD B3LYP/6-311+G(2df)) at the B3LYP/6-311+G* geometries. Core electrons were frozen in treating the electron correlation at the RCCSD(T) and ROVGF levels of theory. The B3LYP, R(U)CCSD(T), ROVGF ab initio calculations were performed using the Gaussian 03 program.[278] Molecular orbital visualization has been done using the MOLDEN3.4 program.[279]

In our theoretical calculations, we first tested the two planar wheel structures of CB_7^- with the C substituting a central (D_{7h}) or a rim B atom (C_{2v}) in the B_8^{2-} molecular wheel. We found that the C_{2v} structure is overwhelmingly favored and is more stable than the D_{7h} structure with heptacoordinate carbon by 63.9 kcal/mol at the B3LYP/6-311+G* level and 63.1 kcal/mol at the CCSD(T)/6-311+G(2df)//CCSD(T)/6-311+G* level. We further searched the potential energy surface for other low-lying structures using the

GEGA method and the top twelve low-lying isomers are shown in Figure 5.3. The C_{2v} wheel structure **I** was found to be the global minimum and the closest-lying isomer (**II**, C_s) is 37.6 kcal/mol (CCSD(T)/6-311+G(2df)//B3LYP/6-311+G*) higher in energy.

The VDE's from the C_{2v} global minimum and the D_{7h} isomer calculated using three theoretical methods are consistent with each other (Table 5.1). We found that the calculated VDE's for the first five detachment channels from the C_{2v} global minimum are in excellent agreement with the experimental PES data, whereas those from the D_{7h} isomer totally disagree with the experiment. The excellent agreement between experiment and theory confirmed unequivocally the C_{2v} molecular wheel global minimum for CB_7^-.

To understand the difference in stability and chemical bonding in the two different molecular-wheel structures of CB_7^-, we analyzed their valence molecular orbitals, as shown in Figure 5.4. The MOs of the D_{7h} CB_7^- (Figure 5.4b) are identical to those of the B_8^{2-} molecular wheel.[16,266-267] It is doubly aromatic with 6 totally delocalized π electrons (HOMO $1e''_2$ and HOMO-3 $1a''_2$) and 6 totally delocalized σ electrons (HOMO-1 $2e'_1$ and HOMO-4 $2a'_1$), as well as 7 MOs (HOMO-2 $1e'_3$, HOMO-5 $1e'_2$, HOMO-6 $1e'_1$, and HOMO-7 $1a'_1$) which can be localized into seven two-center two-electron (2c-2e) B-B peripheral bonds. The MOs of the C_{2v} global minimum (Figure 5.4a) are rather similar to those of the D_{7h} isomer; it is also π aromatic with 6 totally delocalized π electrons (HOMO $1a_2$, HOMO-1 $2b_1$, and HOMO-5 $1b_1$). There are also 7 MOs (HOMO-4 $5a_1$, HOMO-7 $3b_2$, HOMO-8 $3a_1$, HOMO-9 $2b_2$, HOMO-10 $1b_2$, HOMO-11 $2a_1$, and HOMO-12 $1a_1$), which could be localized into five 2c-2e peripheral B-B and two 2c-2e C-B peripheral bonds, similar to those in the D_{7h} isomer. The only

major difference from the MOs of the D_{7h} isomer is shown by the HOMO-6 $4a_1$ orbital of the C_{2v}, in which the peripheral electron delocalization is broken between the two boron atoms located on the opposite side to the carbon atom; the corresponding HOMO-4 $2a'_1$ orbital in the D_{7h} isomer is a completely delocalized σ bonding orbital. For the C_{2v} isomer, an enhancement is also evident in the area between those two boron atoms in the HOMO-3 $6a_1$ (Figure 5.3).

Hence, the σ-aromaticity in the C_{2v} CB_7^- is less pronounced, though we think that this structure is still σ-aromatic from the HOMO-2 $4b_2$, HOMO-3 $6a_1$, and HOMO-6 $4a_1$. In the D_{7h} isomer the bonding between the central carbon atom and the peripheral boron ring is completely delocalized (doubly σ- and π- aromaticity), while in the C_{2v} global minimum structure, the carbon atom is involved in the two 2c-2e B-C peripheral bonds, in addition to the participation in the delocalized σ- and π-bonding. Carbon is known to form strong 2c-2e σ-bonds because of its high valence charge that makes the peripheral position of carbon atom significantly more preferable than the central position. On the other hand, boron is known to participate in delocalized σ-bonding because of its relatively low valence charge, which makes the doubly aromatic C_{2v} structure (I) the most stable. So in contrast to previous theoretical predictions,[251] the current experimental and theoretical study shows that the heptacoordinate carbon in the C-B system is extremely unfavorable.

The low symmetry structure (C_{2v}) of CB_7^- leads to an electric dipole moment of 1.4 Debye (at the B3LYP/6-311+G* level), which makes it possible to electrically manipulate CB_7^- for rotary motions if it can be incorporated into a sandwich-like nanostructure, similar to that experimentally observed in metallacarboranes.[280]

5.3. CB_6^-, CB_6^{2-}, and $C_2B_5^-$ Clusters

In this section, we ponder the global minimum structure of the CB_6^{2-} cluster, which has been touted as a "divining molecule" highlighted on the cover of *Chem. & Eng. News*.[264] Our laser vaporization source can not produce doubly charged anions, since multiply charged species are highly unstable in the gas phase due to the intra-molecular Coulomb repulsion.[281-283] So in the PES experiment, we investigated the corresponding singly charged cluster CB_6^-, as well as $C_2B_5^-$ cluster which is isoelectronic to the dianion CB_6^{2-}. The theoretical calculations were performed for both CB_6^-, $C_2B_5^-$ and CB_6^{2-}. Our joint experimental and theoretical results again show that carbon avoids the hypercoordination in all these three species.[284]

The CB_6^- and $C_2B_5^-$ clusters were produced using a ^{10}B/C mixed target containing about 5% C. The photoelectron spectra were taken at three different photon energies, 355nm, 266 nm and 193 nm, and are presented in Figure 5.5. The spectra of both species are rather broad and complicated, showing many transition bands with apparent overlaps. Even in our highest resolution spectra, the 355 nm, the resolved X band for each cluster is much broader than the intrinsic resolution of the machine, indicating either large geometry changes between the anions and the neutrals, and/or presence of multiple isomers. The observed vertical detachment energies (VDE) for the main PES bands are given in Table 5.2, where they are compared to the theoretical data.

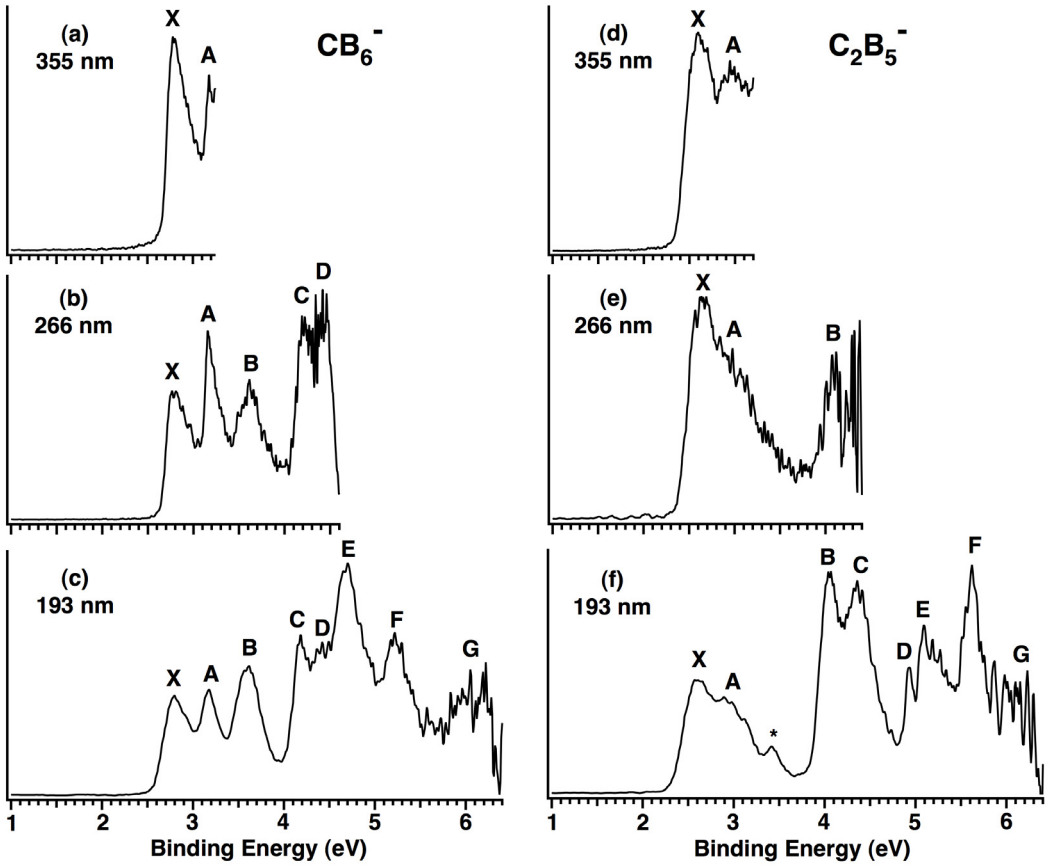

Figure 5.5 Photoelectron spectra of CB_6^- (left) and $C_2B_5^-$ (right) at 355 nm (3.496 eV), 266 nm (4.661 eV), and 193 nm (6.424 eV).

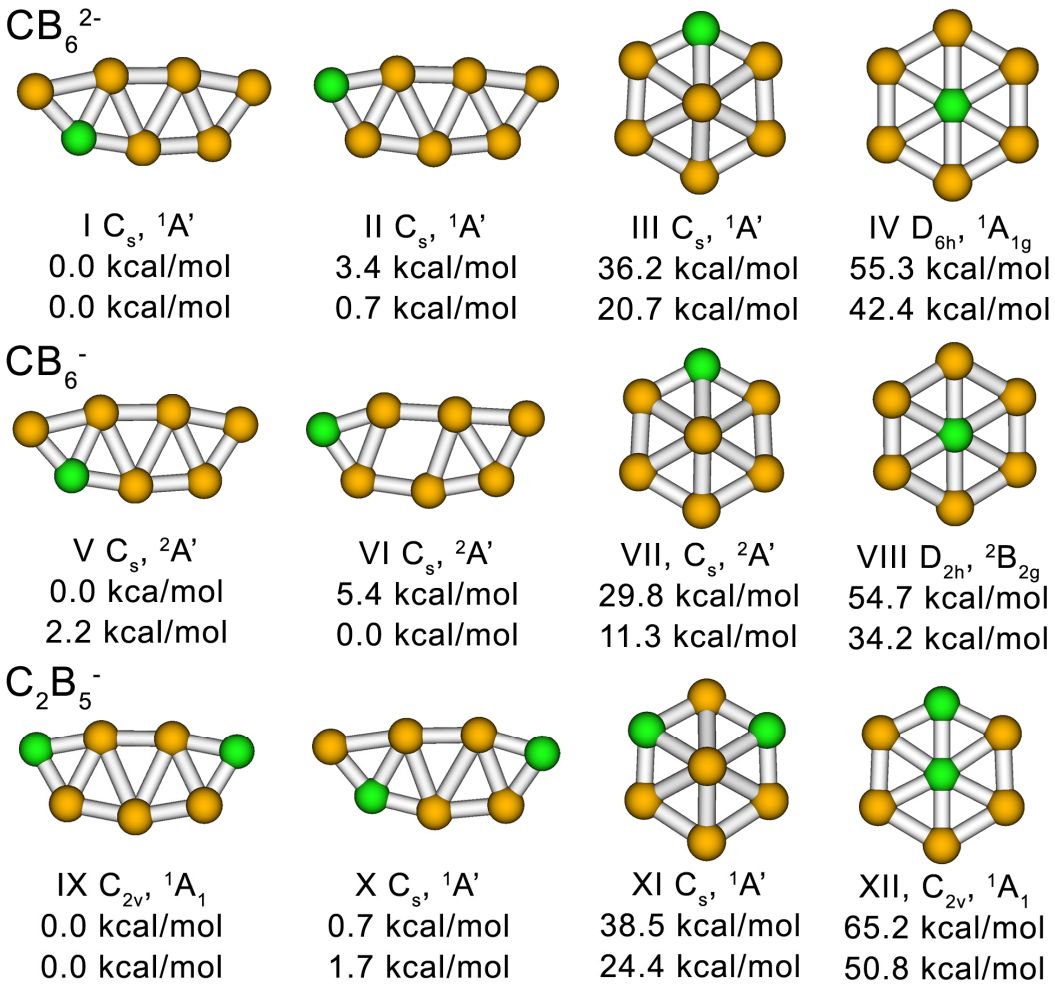

Figure 5.6 Calculated structures and relative energies for CB_6^{2-}, CB_6^-, and $C_2B_5^-$. The upper and lower values are from CCSD(T)/6-311+G(2df)//B3LYP/6-311+G* and B3LYP/6-311+G*), respectively.

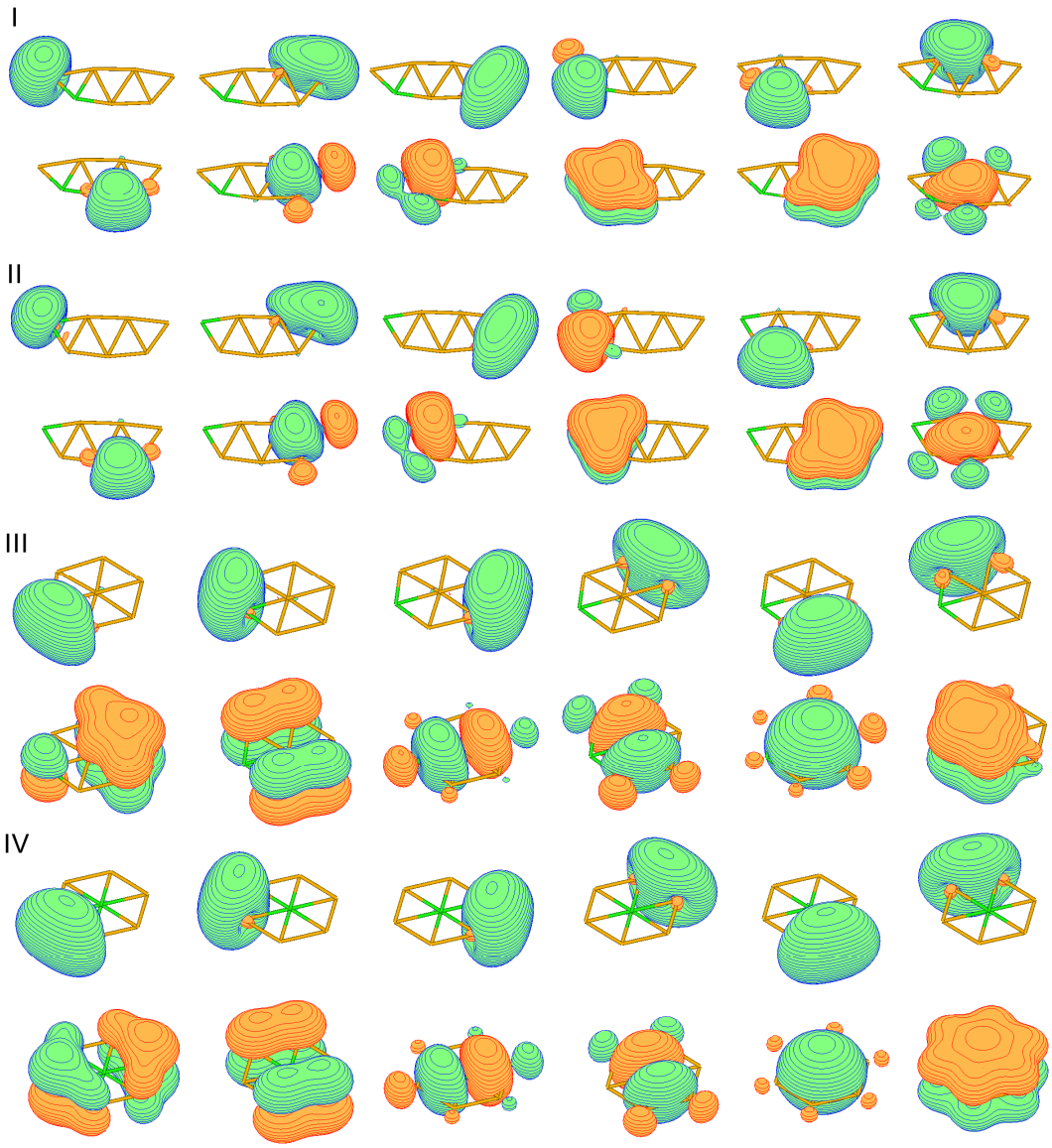

Table 5.7 Orbitals calculated according to the Adaptive Natural Density Partitioning (AdNDP) method of structures of CB_6^{2-} (number of structures are given according to Figure 5.6).

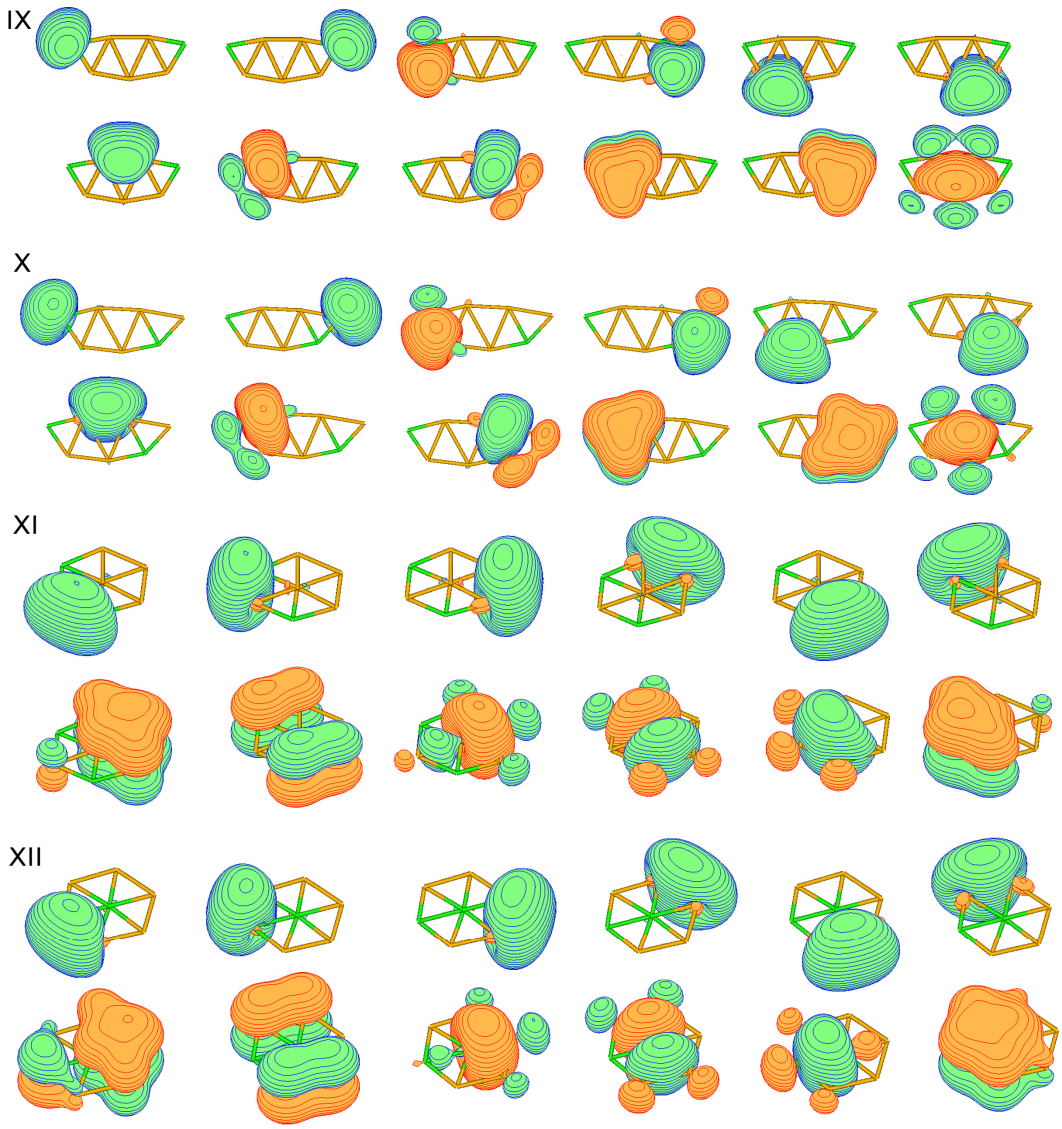

Table 5.8 Orbitals calculated according to the Adaptive Natural Density Partitioning (AdNDP) method of structures of $C_2B_5^-$ (number of structures are given according to Figure 5.6).

Table 5.2 Comparison of experimental and theoretical VDEs (eV) for CB_6^- and $C_2B_5^-$.

	feature	VDE (exp.) [a]	final State and Electronic Configuration	VDE (theo.)		
				TD-B3LYP	OVGF [b]	ΔCCSD(T)[c]
CB_6^-, **V**	X tail	~ 2.9	$^1A'$, $1a''^2 7a'^2 8a'^2 2a''^2 9a'^2 10a'^0$	3.20	3.19 (0.88)	2.95
	B	3.62 (3)	$^3A'$, $1a''^2 7a'^2 8a'^2 2a''^2 9a'^1 10a'^1$	3.65	3.56 (0.88)	3.68
	C	4.21 (3)	$^3A''$, $1a''^2 7a'^2 8a'^2 2a''^1 9a'^2 10a'^1$	4.14	4.11 (0.88)	4.22
	D	~ 4.5	$^1A''$, $1a''^2 7a'^2 8a'^2 2a''^1 9a'^2 10a'^1$	4.55		
	E	4.71 (5)	$^3A'$, $1a''^2 7a'^2 8a'^1 2a''^2 9a'^2 10a'^1$	4.81	4.88 (0.86)	
CB_6^-, **VI**	X[d]	2.78 (3)	$^1A'$, $1a''^2 7a'^2 8a'^2 2a''^2 9a'^2 10a'^0$	3.14	3.58 (0.88)	2.75
	A	3.17 (2)	$^3A'$, $1a''^2 7a'^2 8a'^2 2a''^2 9a'^1 10a'^1$	3.12	2.86 (0.88)	3.14
	C	4.21 (3)	$^3A''$, $1a''^2 7a'^2 8a'^2 2a''^1 9a'^2 10a'^1$	4.13	4.07 (0.88)	4.19
	D	~ 4.5	$^1A''$, $1a''^2 7a'^2 8a'^2 2a''^1 9a'^2 10a'^1$	4.52		
	E	4.71 (5)	$^3A'$, $1a''^2 7a'^2 8a'^1 2a''^2 9a'^2 10a'^1$	4.74	4.78 (0.86)	
$C_2B_5^-$, **IX**	A	2.95 (6)	$^2A_1$, $1b_1^2 4a_1^2 5a_1^2 1a_2^2 4b_2^2 6a_1^1$	3.00	3.08 (0.88)	3.13
	C	4.36 (4)	$^2B_2$, $1b_1^2 4a_1^2 5a_1^2 1a_2^2 4b_2^1 6a_1^2$	4.42	4.73 (0.84)	4.49
	D	4.93 (3)	$^2A_2$, $1b_1^2 4a_1^2 5a_1^2 1a_2^1 4b_2^2 6a_1^2$	4.79	4.90 (0.88)	4.97
$C_2B_5^-$, **X**	X[d]	2.61(5)	$^2A'$, $7a'^2 8a'^2 2a''^2 9a'^2 10a'^1$	2.54	2.74 (0.86)	2.69
	B	4.06 (3)	$^2A'$, $7a'^2 8a'^2 2a''^2 9a'^1 10a'^2$	4.13	4.47 (0.83)	

[a]. Numbers in parentheses represent the uncertainty in the last digit.
[b]. VDEs were calculated at OVGF/6-311+G(2df)//CCSD(T)/6-311+G* level of theory. Values in parentheses represent the pole strength of the OVGF calculation.
[c]. VDEs were calculated at CCSD(T)/6-311+G(2df)//CCSD(T)/6-311+G* level of theory.
[d]. ADEs were estimated from the X band to be 2.71 ± 0.02 eV (CB_6^-) and 2.40 ± 0.05 eV ($C_2B_5^-$). Calculated ADE are 2.65 eV (CB_6^-, V), 2.63 eV (CB_6^-, VI), 2.82 eV ($C_2B_5^-$, IX), and 2.39 eV ($C_2B_5^-$, X) at CCSD(T)/6-311+G(2df)//CCSD(T)/6-311+G*.

Computationally, according to our GEGA search,[276-277] the structure **I** (C_s) is the global minimum for CB_6^{2-} (Figure 5.6). Though the isolated CB_6^{2-} dianion is not electronically stable as Exner pointed out,[250] we used compact (6-311+G*) basis to model this unit in the electronically stable $NaCB_6^-$ or Na_2CB_6 form. This modeling is adequate for the description of the part of the potential energy surface within the Coulomb barrier. The previously discussed[250] structure **IV** (D_{6h}) with a hexacoordinate C is 34.4 kcal/mol higher in energy (herein and after, the relative energies are given at CCSD(T)/6-311+G(2df)//B3LYP/6-311+G*) than the global minimum. Similarly, for CB_6^- and $C_2B_5^-$, the structures with a hexacoordinate C, **VIII** (D_{2h}) and **XII** (C_{2v}), are also significantly higher in energy than the corresponding global minimum structures (Figure 5.6).

For all three clusters, we found a low-lying isomer very close to the global minimum. In the cases of CB_6^- and $C_2B_5^-$, both of the low-lying isomers may be present in the experiment, giving rise to the complicated PES patterns. Indeed, comparison of the theoretical VDEs with the experimental data (Table 5.2) clearly shows that the two lowest isomers are almost equally populated for both CB_6^- and $C_2B_5^-$. For CB_6^-, the first VDEs for the two lowest isomers **V** (2.95 eV) and **VI** (2.75 eV) calculated at the CCSD(T) level are close to each other, and both should contribute to the observed ground-state band X, (Figure 5.5a-c). The first VDE of isomer **VI** is slightly lower, corresponding to the main X band, whereas that of isomer **V** corresponds to the higher binding energy tail of the X band. The second calculated VDEs for isomers **V** (3.68 eV) and **VI** (3.14 eV) are very different, corresponding to the observed PES bands B and A, respectively, and providing the most critical spectral signatures for the presence of both isomers. Spectral features beyond 4 eV can all be assigned to the two isomers.

For $C_2B_5^-$, the first four observed PES bands (Figure 5.5d-f) can be unambiguously assigned to the first two detachment channels of each of the two lowest isomers, as shown in Table 5.2. Higher PES bands can also be assigned to the higher binding energy detachment channels from the two isomers (the peak labeled * is likely due to a vibrational feature of the A band or contribution from a third low-lying isomer). All the observed PES bands are relatively broad without vibrational resolution, consistent with the low symmetries of the two isomers of each cluster and suggesting that these structures are relatively floppy. Overall the agreement between the observed PES features and the theoretical data is quite satisfying, providing considerable credence for the obtained lowest structures for CB_6^- (**V** and **VI**) and $C_2B_5^-$ (**IX** and **X**). Clearly, the isomers with a hexacoordinate C (**VIII** for CB_6^- and **XII** for $C_2B_5^-$) are too high in energy. Though the isomers **IV** and **XII** are true local minima and maybe kinetically stable, we were only able to observe the global minimum and low-lying isomers.

To understand why the structures with a hexacoordinate C for CB_6^{2-}, CB_6^- and $C_2B_5^-$ are higher in energy than the global minima, we analyzed their chemical bonding using the recently developed Adaptive Natural Density Partitioning (AdNDP) method,[285] which is an extension of the Natural Bond Orbital (NBO) analysis. This approach leads to partitioning of the charge density into elements with the highest possible degree of localization of electron pairs: *n* center – two electron (*n*c-2e) bonds. If some part of the density cannot be localized in this manner, it is represented using completely delocalized objects, similar to the canonical MOs, naturally incorporating the idea of completely delocalized (globally aromatic) bonding. Thus, AdNDP achieves seamless description of different types of chemical bonds. If we encounter a molecule or a cluster in which

AdNDP analysis reveals that σ- or π- electrons cannot be localized into lone pairs or 2c-2e bonds, we consider this species from the aromaticity/antiaromaticity point of view. If delocalization occurs over the whole chemical species and the corresponding bonds satisfy the 4n+2 rule we consider such species to be globally aromatic.

According to our AdNDP analyses (see Figures 5.7 and 5.8 for details), the hexagonal structures of CB_6^{2-} and $C_2B_5^-$ are doubly (σ- and π-) aromatic systems (6 delocalized σ-electrons and 6 delocalized σ-electrons) with six peripheral two-center two-electron (2c-2e) B-B or B-C bonds. This bonding picture explains why the hexagonal isomers (**IV** and **XII**) with a central C atom are higher in energy than the hexagonal structures (**III** and **XI**) with the C atoms located on the periphery. The central C atoms in the hexagonal isomers **IV** and **XII** are involved in delocalized bonding only, while in the isomers **III** and **XI** the C atoms are involved in 2c-2e peripheral bonding in addition to the delocalized bonding. The higher electronegativity of C compared to B makes it prefer to form 2c-2e bonds more than boron does, which clearly disfavors the hexacoordinate C isomers of CB_6^{2-} and $C_2B_5^-$.

The lowest energy structures **I** and **II** for CB_6^{2-} and **IX** and **X** for $C_2B_5^-$ originate from hepta-cyclic structures. These four structures are all σ-aromatic (6 delocalized σ-electrons) and π-antiaromatic (4 π-electrons) and have seven peripheral 2c-2e B-B/ B-C bonds. There are no "internal" 2c-2e B-B or B-C bonds; in Figure 5.6 the internal lines connecting atoms do not represent 2c-2e B-B or B-C bonds. In order to prove that these low symmetry structures are indeed related to seven-member rings we performed additional calculations for the neutral CB_6 cluster. We started from the geometry of the CB_6^{2-} global minimum structure **I** and removed two electrons from its HOMO.

Subsequent geometry optimization led to an almost perfect heptagonal ring for CB_6 (C_{2v}, $^1A_1$), which is doubly aromatic (2 σ-electrons and 6 π-electrons) with seven 2c-2e peripheral B-B and B-C bonds. Hence, the stable low-lying structures **I** and **II** for CB_6^{2-} and **IX** and **X** for $C_2B_5^-$ are derived from distortions of the hepta-cyclic structures due to π antiaromaticity. In any case, our current work shows that the CB_6^-, CB_6^{2-}, and $C_2B_5^-$ clusters all have low-symmetry structures, and they are clearly not the viable candidates for synthesis of hexacoordinate carbon species.

5.4. CB_8^- and CB_8 Clusters

In the final part of this chapter, we investigate the anion CB_8^- and the neutral CB_8 clusters. Similar to the case of CB_7^- as discussed in section 5.2,[268] the CB_8 cluster is isoelectronic to the B_9^- anion cluster which we have shown previously to have a D_{8h} wheel structure.[16,266] The theoretically proposed D_{8h} structure of CB_8 with octacoordinate carbon[251] can be viewed as substituting the central B^- ion in B_9^- with a C atom, and represents the highest coordination number yet proposed for the central C atom in a planar arrangement. However, here we show through our joint photoelectron spectroscopy and *ab initio* studies that the experimentally observed species is a C_s CB_8^- cluster, and the corresponding neutral species CB_8 has a C_{2v} wheel structure in which the C atom replaces a B atom from the edge rather than at the center of the D_{8h} B_9^- cluster, thus hypercoordinate carbon does not exist in the CB_8 cluster.[286]

The photoelectron spectrum of CB_8^- taken at 193 nm is shown in Figure 5.9. We can see that the spectrum is rather broad and complicated, suggesting either large geometry changes between the anion and the neutral or a cluster with low symmetry.

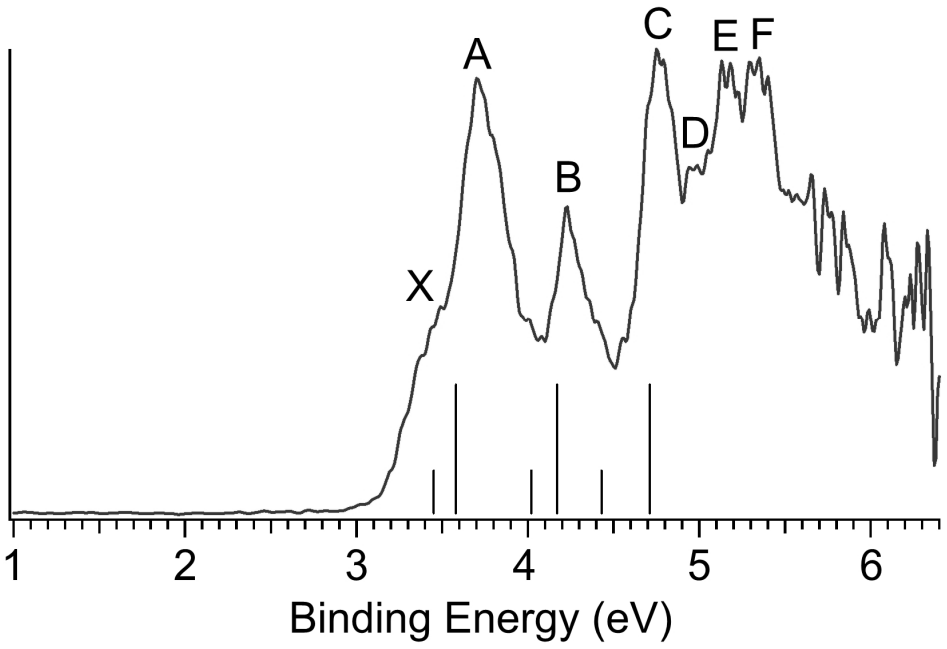

Figure 5.9 Photoelectron spectrum of CB_8^- at 193 nm. The vertical bars represent the calculated VDEs (at TD-B3LYP level) for the lowest anion structure. The short bars represent the detachment transitions to singlet neutral states while the longer ones represent transitions to triplet final states.

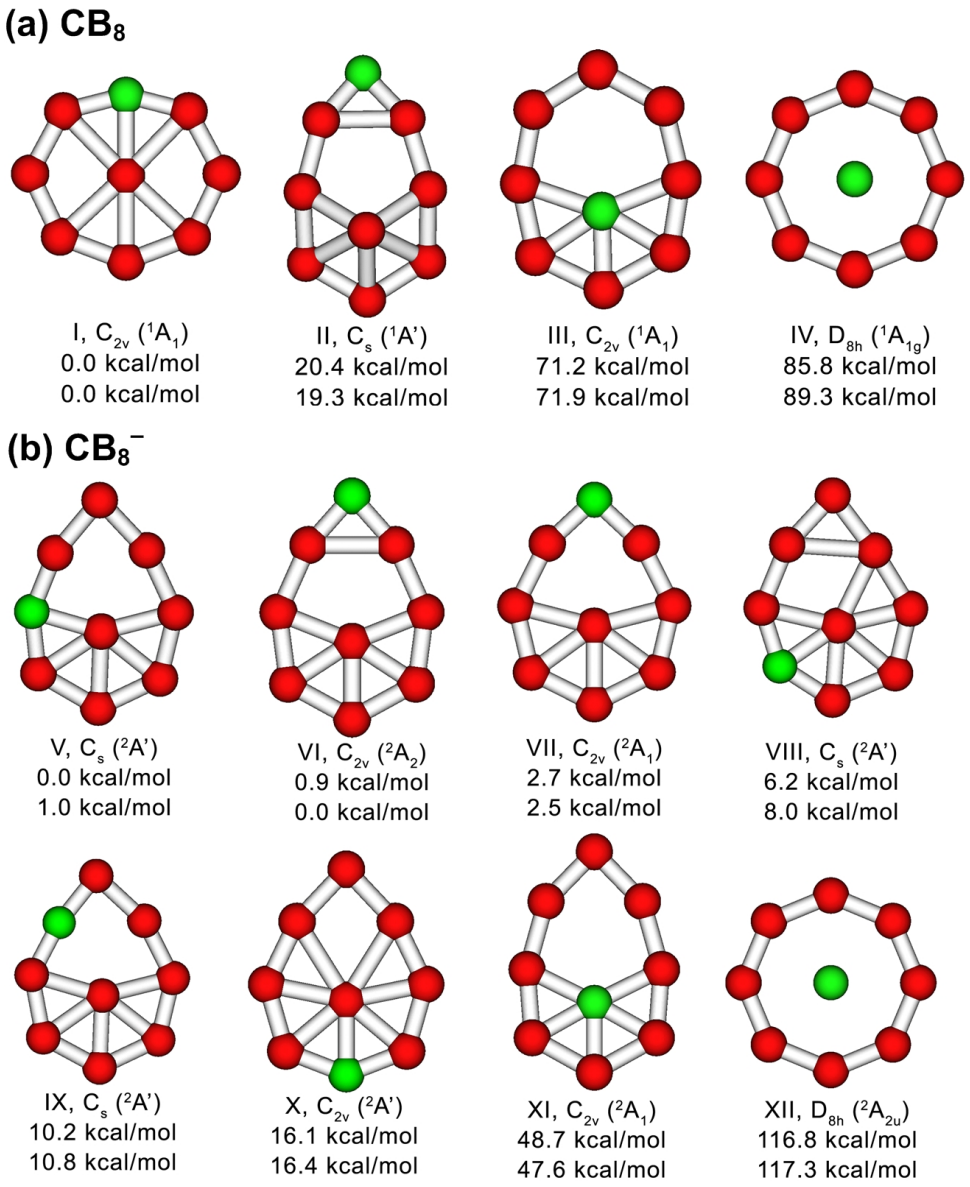

Figure 5.10 Selected structures optimized for (a) CB_8 and (b) CB_8^-. Upper and lower numbers are relative energies calculated at the CCSD(T)/6-311+G(2df)//B3LYP/6-311+G*+ZPE//B3LYP/6-311+G* and B3LYP/6-311+G*+ZPE//B3LYP/6-311+G* levels of theory, respectively.

Table 5.3 Comparison of the experimental vertical detachment energies (VDE) of CB_8^- to the calculated values for the global minimum C_S structure. All energies are in eV.

Feature	VDE (exp.) [a]	Final State and Electronic Configuration	VDE (theo.)		
			TD-B3LYP [b]	OVGF [c]	DCCSD(T) [d]
X [e]	~ 3.45	$^1A'$, $9a'^2 10a'^2 11a'^2 2a''^2 3a''^2 12a'^0$	3.45	3.69 (0.89)	3.41
A	3.70 (5)	$^3A''$, $9a'^2 10a'^2 11a'^2 2a''^2 3a''^1 12a'^1$	3.58	3.57 (0.89)	3.72
A tail	~ 4.0	$^1A''$, $9a'^2 10a'^2 11a'^2 2a''^2 3a''^1 12a'^1$	4.02	[f]	[f]
B	4.23 (4)	$^3A''$, $9a'^2 10a'^2 11a'^2 2a''^1 3a''^2 12a'^1$	4.17	4.27 (0.88)	[f]
B tail	~ 4.5	$^1A''$, $9a'^2 10a'^2 11a'^2 2a''^1 3a''^2 12a'^1$	4.43	[f]	[f]
C	4.75 (5)	$^3A'$, $9a'^2 10a'^2 11a'^1 2a''^2 3a''^2 12a'^1$	4.71	4.93 (0.88)	4.80
D	~ 5	$^3A'$, $9a'^2 10a'^1 11a'^2 2a''^2 3a''^2 12a'^1$	5.06	5.17 (0.87)	[f]
E	5.16 (5)	$^1A'$, $9a'^2 10a'^2 11a'^1 2a''^2 3a''^2 12a'^1$	5.48	[f]	[f]
F	5.35 (5)	$^3A'$, $9a'^1 10a'^2 11a'^2 2a''^2 3a''^2 12a'^1$	5.66	5.80 (0.86)	[f]

[a] Numbers in the parentheses represent uncertainties in the last digit.
[b] The first VDE was calculated at the B3LYP/6-311+G(2df)//B3LYP/6-311+G* level of theory as the lowest transition from the doublet state of the anion into the final lowest singlet state of the neutral. Then the vertical excitation energies of the neutral species (at the TD-B3LYP level) were added to the first VDE to obtain the second and higher VDEs.
[c] UOVGF/6-311+G(2df)//B3LYP/6-311+G*. Pole strength is given in parenthesis.
[d] UCCSD(T)/6-311+G(2df)//B3LYP/6-311+G*.
[e] The adiabatic detachment energy (ADE) was estimated to be 3.2±0.1 eV.
[f] This VDE cannot be calculated at this level of theory.

Numerous spectral features are apparently resolved and are labeled in Figure 5.9. The experimental vertical detachment energies (VDEs) of the resolved PES bands are given in Table 5.3 and compared with theoretical values to be discussed below. The calculated VDEs (at TD-B3LYP level) of the first few detachment channels for the lowest energy structure V (Figure 5.10) are plotted as vertical bars in the spectrum shown in Figure 5.9 for comparison.

As usual, our theoretical collaborators performed searches for the global minimum structure of CB_8 and CB_8^- using the GEGA program,[277] and found that isomer I (Figure 5.10a) and isomer V (Figure 5.10b) is the global minimum for CB_8 and CB_8^-, respectively, consistent with a recent theoretical study.[287] For the neutral CB_8, isomer I is overwhelmingly stable, and the closest isomer II was found to be 20.4 kcal/mol higher in energy. We found that the high symmetry structure IV with the putative octa-coordinate carbon is a second-order saddle point consistent with previous calculations by Minkin *et al*.[254] Optimization following the imaginary frequencies led to isomer III, which is significantly higher (71.2 kcal/mol) than the global minimum. For the anion CB_8^-, there are two close-lying isomers VI and VII, whereas other isomers (VIII-XI) are found to be significantly higher in energy. Again, the high symmetry structure XII with an octa-coordinate carbon is unstable with five imaginary frequencies and it was found to be 116.8 kcal/mol higher than the global minimum structure.

The calculated VDEs for the global minimum structure (V) of CB_8^- are presented in Table 5.3, along with the tentative assignments to the experiment. As shown in Table 5.3, the B3LYP VDEs are more complete and the calculated values are overall in good agreement with the experimental data. The CCSD(T) VDEs for the X, A, and C channels

are indeed in quantitative agreement with the experimental values. VDEs calculated for the close-lying isomers VI and VII do not agree well with the experimental data (not shown). Due to the broad nature of the experimental spectrum, we could not completely rule out the presence of isomers VI and VII. However, their contributions to the observed spectrum, if any, were expected to be small. The large geometry change between the anion and the neutral (Figure 5.10) is consistent with the broad PES spectrum observed.

Our collaborators performed AdNDP analysis[285] to understand the chemical bondings in the CB_8 and CB_8^- clusters. Again, we discuss the bonding in terms of aromaticity/antiaromaticity. According to our AdNDP analysis, the D_{8h} structure (IV) of CB_8 is a doubly (σ– and π–) aromatic system (6 delocalized σ–electrons and 6 delocalized π–electrons) with eight peripheral 2c-2e B-B bonds (Figure 5.11a). Its bonding pattern is identical to that of the B_9^-.[16,266] However, unlike B_9^-, the D_{8h} CB_8 is not even a minimum on the potential energy surface, because the carbon atom is too small to make a perfect fit into the B_8 ring. Therefore, it is important to take into account the geometric factors in designing highly coordinated planar molecules. The bonding pattern in isomer III (Figure 5.11c) formed out of the unstable structure IV is somewhat different from the bonding pattern of the high-symmetry structure IV (Figure 5.11a). Although their eight peripheral 2c-2e B-B bonds (Figure 5.11a-1 and 5.11c-1) are very similar, their delocalized σ– and π–bonds are different. The π–bonds in structure IV (Figure 5.11a-5-7) are delocalized over the whole cluster, while in isomer III they become one 3c-2e (Figure 5.11c-5) and two 4c-2e π–bonds (Figure 5.11c-6 and 7). Despite these changes, the partially localized π bonds in isomer III are simply linear combinations of the completely delocalized π–bonds in structure IV. This was confirmed

by calculating a slightly distorted structure IV* (Figure 5.11b), in which the central carbon atom was shifted by 0.004 Å from the central position. Neither the total energy nor the orbital energies of IV* changes significantly from that of IV, but the shape of the π–bonds (Figure 5.11b-5-7) in this distorted structure now looks exactly like that in isomer III (Figure 5.11c-5-7). Hence, isomer III can be still viewed as a π–aromatic system. However, isomer III is no longer a σ–aromatic system, even though it has three partially delocalized σ–bonds. We found that the σ–bonding pattern in the slightly distorted structure IV* (Figure 5.11b-2-4) is different from that in isomer III (Figure 5.11c-2-4). The slightly distorted structure IV* is still σ–aromatic, even though the σ–bonds are now partially localized, analogous to the π–bonds discussed above. However, upon further distortion towards isomer III one of the "aromatic" σ–bond (Figure 5.11b-4) is transformed into a new σ–bond (Figure 5.11c-4). The three σ–bonds in III (Figure 5.11c-2-4) are now localized on the bottom part of the cluster, while the three upper peripheral atoms do not participate in the delocalized σ–bonding. Therefore, isomer III is no longer σ–aromatic.

However, note that neither III nor IV is the lowest-energy structure of CB_8, but the structure I. The reason why isomer I is significantly more stable than structure III and IV can be understood in a similar way as that for CB_6^{2-}.[284] That is, the central C atom in structures III and IV of CB_8 is involved in delocalized bonding with the peripheral atoms only, while in isomer I the C atom is also involved in 2c-2e peripheral bonding with two neighboring boron atoms, in addition to the delocalized bonding. Because of its higher electronegativity, carbon prefers to form 2c-2e bonding much more than boron does, thus carbon clearly favors the rim site in the wheel structures. The bonding pattern of structure

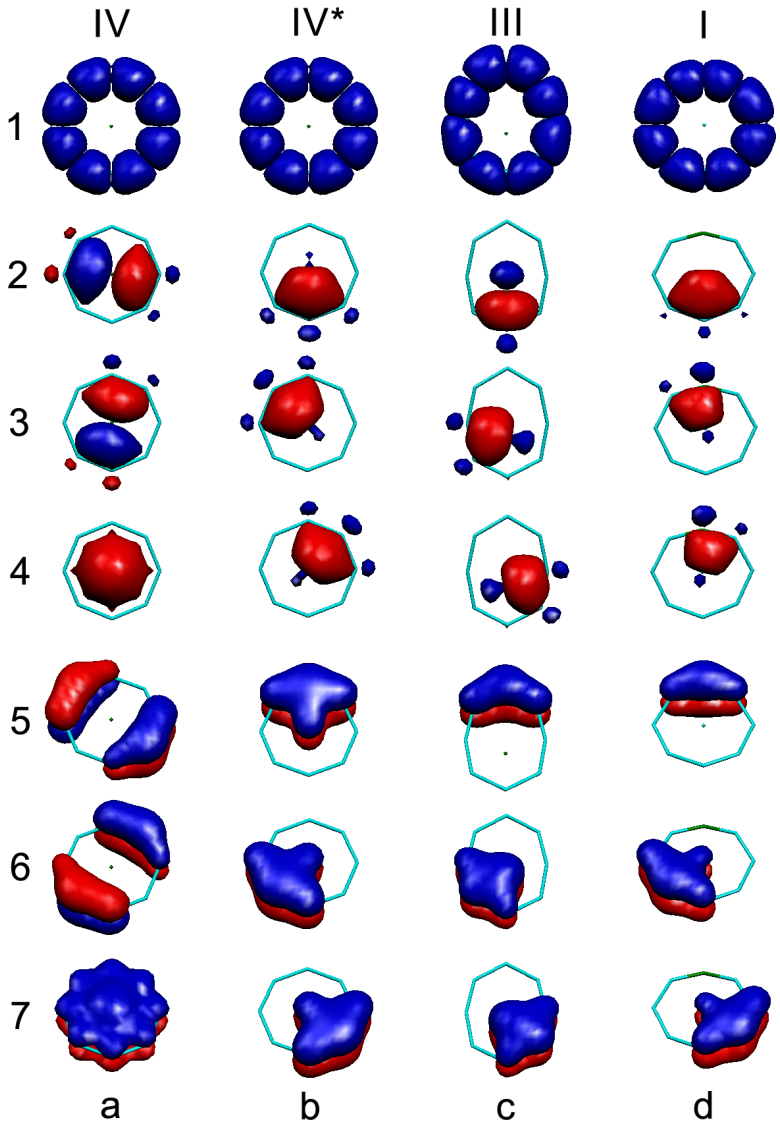

Figure 5.11 The eight 2c-2e B-B or B-C σ-bonds superimposed over the CB_8 structures (first row), the three delocalized σ-bonds (second to fourth rows), and the three delocalized π-bonds (fifth to seventh rows), recovered by the AdNDP analysis (see text for details).

I (Figure 5.11d) is almost identical to the bonding pattern of the slightly distorted structure IV* (Figure 5.11b) and thus, isomer I is also doubly (σ– and π–) aromatic.

Finally, our study implies that, when designing hypercoordinate planar carbon molecules or planar chemical species with other hypercoordinated atoms, one needs to consider both the atomic size and electronegativity of the central atom. To be stable, the designed wheel structure has to be a minimum (geometric fit, i.e., structural factor) and also the system has to be doubly aromatic (electronic factor). Our previous studies on pure boron clusters[16,266] revealed that in planar boron clusters there is always a peripheral ring of 2c-2e B-B σ-bonds with additional delocalized bonding between peripheral atoms or peripheral atoms and atoms located inside of the ring. The presence of these peripheral rings (e.g. in B_8^{2-} and B_9^-) gives us an opportunity to design planar molecules with hypercoordinate central atoms. According to our analysis above, in order to obtain planar boron clusters with a hypercoordinate central atom, atoms which are more electropositive than boron should be considered to be placed at the center. Indeed, two recent theoretical papers, respectively, suggested that Al atom[288] and Fe atom[289] can be placed into a B_9 ring to result in a highly symmetric D_{9h} planar wheel structure with a nine-coordinate Al or Fe atom. Both Al and Fe atoms have the right size to be enclosed by the B_9 ring, and our AdNDP bonding analysis reveals that both systems are doubly aromatic, consistent with our proposal discussed above. We further applied the AdNDP chemical bonding model to the CAl_4^- cluster, which is the experimentally confirmed tetracoordinate planar carbon species.[11] It is found that there is no 2c-2e peripheral Al-Al σ-bond in CAl_4^{2-}. Instead, there is a lone pair at each aluminum atom. Therefore, in order to design a chemical species with a central hypercoordinate carbon atom, one should consider

electropositive ligands, which would have lone pair electrons instead of forming 2c-2e peripheral bonds.

5.5. Conclusion

In conclusion, we characterized a series of carbon-boron mixed clusters, CB_7^- ,CB_6^-, $C_2B_5^-$, CB_6^{2-}, and CB_8^- which have been suggested previously to be novel molecules containing hypercoordinate planar carbon, using photoelectron spectroscopy experiments and *ab initio* calculations. We found that all these species adopt low symmetry planar structures, and carbon atom avoids the hypercoordination in the wheel type structures. Chemical bonding analysis performed by the AdNDP method revealed that the atom in the central position in the wheel type structures is involved in delocalized bonding only, while atoms at the periphery are involved in both delocalized bonding and 2c-2e peripheral σ-bonding. The carbon atom, being more electronegative than the boron atom, favors peripheral positions, where it can participate in 2c-2e σ-bonding. Thus, in contrast to the previous theoretical predictions, our current work shows that the boron ring wheel-type structures are not viable candidates for designing planar molecules with a hypercoordinate central carbon atom.

BIBLIOGRAPHY

(1) *Clusters of Atoms and Molecules, Vol. I*; Ed. by Haberland, H., (Springer, Berlin), 1994.

(2) *Encyclopedia of Chemical Physics and Physical Chemistry*; Moore, J. H.; Spencer, N. D., Eds.; IOP Publishing Inc.: Philadelphia, 2001.

(3) Deheer, W. A. *Rev. Mod. Phys.* **1993**, *65*, 611.

(4) Brack, M. *Rev. Mod. Phys.* **1993**, *65*, 677.

(5) Busani, R.; Folkers, M.; Cheshnovsky, O. *Phys. Rev. Lett.* **1998**, *81*, 3836.

(6) Li, J.; Li, X.; Zhai, H. J.; Wang, L. S. *Science* **2003**, *299*, 864.

(7) Kroto, H. W.; Heath, J. R.; Obrien, S. C.; Curl, R. F.; Smalley, R. E. *Nature* **1985**, *318*, 162.

(8) Curl, R. F. *Rev. Mod. Phys.* **1997**, *69*, 691.

(9) Kroto, H. *Rev. Mod. Phys.* **1997**, *69*, 703.

(10) Smalley, R. E. *Rev. Mod. Phys.* **1997**, *69*, 723.

(11) Li, X.; Wang, L. S.; Boldyrev, A. I.; Simons, J. *J. Am. Chem. Soc.* **1999**, *121*, 6033.

(12) Wang, L. S.; Boldyrev, A. I.; Li, X.; Simons, J. *J. Am. Chem. Soc.* **2000**, *122*, 7681.

(13) Furche, F.; Ahlrichs, R.; Weis, P.; Jacob, C.; Gilb, S.; Bierweiler, T.; Kappes, M. M. *J. Chem. Phys.* **2002**, *117*, 6982.

(14) Hakkinen, H.; Moseler, M.; Landman, U. *Phys. Rev. Lett.* **2002**, *89,* 033401.

(15) Hakkinen, H.; Yoon, B.; Landman, U.; Li, X.; Zhai, H. J.; Wang, L. S. *J. Phys. Chem. A* **2003**, *107*, 6168.

(16) Alexandrova, A. N.; Boldyrev, A. I.; Zhai, H.-J.; Wang, L.-S. *Coord. Chem. Rev.* **2006**, *250*, 2811.

(17) Bergeron, D. E.; Castleman, A. W., Jr.; Morisato, T.; Khanna, S. N. *Science* **2004**, *304*, 84.

(18) Cui, L. F.; Huang, X.; Wang, L. M.; Zubarev, D. Y.; Boldyrev, A. I.; Li, J.; Wang, L. S. *J. Am. Chem. Soc.* **2006**, *128*, 8390.

(19) Li, X.; Kuznetsov, A. E.; Zhang, H.-F.; Boldyrev, A. I.; Wang, L.-S. *Science* **2001**, *291*, 859.

(20) Haruta, M. *Catal. Today* **1997**, *36*, 153.

(21) Henry, C. R. *Surf. Sci. Rep.* **1998**, *31*, 231.

(22) Ertl, G.; Freund, H. J. *Phys. Today* **1999**, *52*, 32.

(23) Chretien, S.; Buratto, S. K.; Metiu, H. *Cur. Opi. Sol. Sta. Mat. Sci.* **2007**, *11*, 62.

(24) Vajda, S.; Pellin, M. J.; Greeley, J. P.; Marshall, C. L.; Curtiss, L. A.; Ballentine, G. A.; Elam, J. W.; Catillon-Mucherie, S.; Redfern, P. C.; Mehmood, F.; Zapol, P. *Nat. Mater.* **2009**, *8*, 213.

(25) Lee, S.; Molina, L. M.; Lopez, M. J.; Alonso, J. A.; Hammer, B.; Lee, B.; Seifert, S.; Winans, R. E.; Elam, J. W.; Pellin, M. J.; Vajda, S. *Angew. Chem. Int. Ed.* **2009**, *48*, 1467.

(26) Kratschmer, W.; Lamb, L. D.; Fostiropoulos, K.; Huffman, D. R. *Nature* **1990**, *347*, 354.

(27) Claridge, S. A.; Castleman, A. W.; Khanna, S. N.; Murray, C. B.; Sen, A.; Weiss, P. S. *Acs Nano* **2009**, *3*, 244.

(28) Zhang, H. F.; Stender, M.; Zhang, R.; Wang, C. M.; Li, J.; Wang, L. S. *J. Chem. Phys. B* **2004**, *108*, 12259.

(29) Sun, Z. M.; Xiao, H.; Li, J.; Wang, L. S. *J. Am. Chem. Soc.* **2007**, *129*, 9560.

(30) Sattler, K.; Mühlbach, J.; Recknagel, E. *Phys. Rev. Lett.* **1980**, *45*, 821.

(31) Martin, T. P.; Schaber, H. *J. Chem. Phys.* **1985**, *83*, 855.

(32) Martin, T. P.; Bergmann, T.; Göhlich, H.; Lange, T. *Chem. Phys. Lett.* **1990**, *172*, 209.

(33) Larsen, R. A.; Neoh, S. K.; Herschbach, D. R. *Rev. Sci. Instrum.* **1974**, *45*, 1511.

(34) Dietz, T. G.; Duncan, M. A.; Powers, D. E.; Smalley, R. E. *J. Chem. Phys.* **1981**, *74*, 6511.

(35) Cha, C.-Y.; Gantefor, G.; Eberhardt, W. *Rev. Sci. Instrum.* **1992**, *63*, 5661.

(36) Haberland, H.; Mall, M.; Moseler, M.; Qiang, Y.; Reiners, T.; Thurner, Y. *J. Vac. Sci. Tech. A* **1994**, *12*, 2925.

(37) Fenn, J.; Mann, M.; Meng, C.; Wong, S.; Whitehouse, C. *Science* **1989**, *246*, 64.

(38) Spence, T. G.; Trotter, B. T.; Burns, T. D.; Posey, L. A. *J. Phys. Chem. A* **1998**, *102*, 6101.

(39) Ding, C.-F.; Wang, X.-B.; Wang, L.-S. *J. Phys. Chem. A* **1998**, *102*, 8633.

(40) Bouwen, W.; Vanhoutte, F.; Despa, F.; Bouckaert, S.; Neukermans, S.; Kuhn, L. T.; Weidele, H.; Lievens, P.; Silverans, R. E. *Chem. Phys. Lett.* **1999**, *314*, 227.

(41) Lian, L.; Su, C.-X.; Armentrout, P. B. *J. Chem. Phys.* **1992**, *97*, 4084.

(42) Knight, W. D.; Clemenger, K.; de Heer, W. A.; Saunders, W. A.; Chou, M. Y.; Cohen, M. L. *Phys. Rev. Lett.* **1984**, *52*, 2141.

(43) Schmidt, M.; Kusche, R.; Kronmüller, W.; von Issendorff, B.; Haberland, H. *Phys. Rev. Lett.* **1997**, *79*, 99.

(44) Neal, C. M.; Starace, A. K.; Jarrold, M. F. *J. Am. Soc. Mass. Spectr.* **2007**, *18*, 74.

(45) Cox, D. M.; Trevor, D. J.; Whetten, R. L.; Rohlfing, E. A.; Kaldor, A. *Phys. Rev. B* **1985**, *32*, 7290.

(46) Bucher, J. P.; Douglass, D. C.; Bloomfield, L. A. *Phys. Rev. Lett.* **1991**, *66*, 3052.

(47) Billas, I. M. L.; Chatelain, A.; Deheer, W. A. *Science* **1994**, *265*, 1682.

(48) Li, S.; Fuller, J. F.; Wang, X.; Sohnlein, B. R.; Bhowmik, P.; Yang, D.-S. *J. Chem. Phys.* **2004**, *121*, 7692.

(49) Stolow, A.; Bragg, A. E.; Neumark, D. M. *Chem. Rev.* **2004**, *104*, 1719.

(50) *Advances in Metal and Semiconductor Clusters*; Ed. by Duncan, M. A., (JAI Press Inc.), 1993-1998; Vol. 1-4.

(51) Hu, Z. D.; Shen, B.; Lombardi, J. R.; Lindsay, D. M. *J. Chem. Phys.* **1992**, *96*, 8757.

(52) von Helden, G.; van Heijnsbergen, D.; Meijer, G. *J. Phys. Chem. A* **2003**, *107*, 1671.

(53) Leopold, D. G.; Ho, J.; Lineberger, W. C. *J. Chem. Phys.* **1987**, *86*, 1715.

(54) *Transport Properties of Ions in Gases*; Ed. by Mason, E. A. and McDaniel, E. W. (Wiley: New York), 1988.

(55) Kemper, P. R.; Bowers, M. T. *J. Phys. Chem.* **2002**, *95*, 5134.

(56) Jarrold, M. F.; Bower, J. E. *J. Chem. Phys.* **1992**, *96*, 9180.

(57) Hunter, J.; Fye, J.; Jarrold, M. F. *Science* **1993**, *260*, 784.

(58) Weis, P.; Gilb, S.; Gerhardt, P.; Kappes, M. M. *Int'l. J. Mass. Spec.* **2002**, *216*, 59.

(59) Gilb, S.; Weis, P.; Furche, F.; Ahlrichs, R.; Kappes, M. M. *J. Chem. Phys.* **2002**, *116*, 4094.

(60) Paul, W. *Rev. Mod. Phys.* **1990**, *62*, 531.

(61) Maier-Borst, M.; Cameron, D. B.; Rokni, M.; Parks, J. H. *Phys. Rev. A* **1999**, *59*, R3162.

(62) Xing, X. P.; Danell, R. M.; Garzon, I. L.; Michaelian, K.; Blom, M. N.; Burns, M. M.; Parks, J. H. *Phys. Rev. B* **2005**, *72,* 081405.

(63) Xing, X. P.; Yoon, B.; Landman, U.; Parks, J. H. *Phys. Rev. B* **2006**, *74, 165423*.

(64) Oger, E.; Kelting, R.; Weis, P.; Lechtken, A.; Schooss, D.; Crawford, N. R. M.; Ahlrichs, R.; Kappes, M. M. *J Chem Phys* **2009**, *130*, 124305.

(65) Lechtken, A.; Neiss, C.; Kappes, M. M.; Schooss, D. *Phys. Chem. Chem. Phys.* **2009**, *11*, 4344.

(66) Blom, M. N.; Schooss, D.; Stairs, J.; Kappes, M. M. *J. Chem. Phys.* **2006**, *124*.

(67) Gough, T. E.; Mengel, M.; Rowntree, P. A.; Scoles, G. *J. Chem. Phys.* **1985**, *83*, 4958.

(68) Fielicke, A.; Kirilyuk, A.; Ratsch, C.; Behler, J.; Scheffler, M.; von Helden, G.; Meijer, G. *Phys. Rev. Lett.* **2004**, *93*, 023401.

(69) Gruene, P.; Rayner, D. M.; Redlich, B.; van der Meer, A. F. G.; Lyon, J. T.; Meijer, G.; Fielicke, A. *Science* **2008**, *321*, 674.

(70) Roscioli, J. R.; Hammer, N. I.; Johnson, M. A. *J. Phys. Chem. A* **2006**, *110*, 7517.

(71) Relph, R. A.; Bopp, J. C.; Roscioli, J. R.; Johnson, M. A. *J. Chem. Phys.* **2009**, *131*, 114305.

(72) Hu, Z.; Shen, B.; Lombardi, J. R.; Lindsay, D. M. *J. Chem. Phys.* **1992**, *96*, 8757.

(73) Chertihin, G. V.; Andrews, L. *J. Chem. Phys.* **1997**, *106*, 3457.

(74) Nordling, C.; Sokolowski, E.; Siegbahn, K. *Phys. Rev.* **1957**, *105*, 1676.

(75) Turner, D. W.; Jobory, M. I. A. *J. Chem. Phys.* **1962**, *37*, 3007.

(76) Cheshnovsky, O.; Yang, S. H.; Pettiette, C. L.; Craycraft, M. J.; Smalley, R. E. *Rev. Sci. Instrum.* **1987**, *58*, 2131.

(77) Gantefor, G.; Meiwesbroer, K. H.; Lutz, H. O. *Phys. Rev. A* **1988**, *37*, 2716.

(78) Markovich, G.; Giniger, R.; Levin, M.; Cheshnovsky, O. *J. Chem. Phys.* **1991**, *95*, 9416.

(79) Lippa, T. P.; Xu, S.-J.; Lyapustina, S. A.; Nilles, J. M.; Bowen, K. H. *J. Chem. Phys.* **1998**, *109*, 10727.

(80) Metz, R. B.; Kitsopoulos, T.; Weaver, A.; Neumark, D. M. *J. Chem. Phys.* **1988**, *88*, 1463.

(81) Wang, L. S.; Cheng, H. S.; Fan, J. W. *J. Chem. Phys.* **1995**, *102*, 9480.

(82) Nakajima, A.; Taguwa, T.; Hoshino, K.; Sugioka, T.; Naganuma, T.; Ono, F.; Watanabe, K.; Nakao, K.; Konishi, Y.; Kishi, R.; Kaya, K. *Chem. Phys. Lett.* **1993**, *214*, 22.

(83) Wrigge, G.; Hoffmann, M. A.; von Issendorff, B.; Haberland, H. *Eur. Phys. J. D* **2003**, *24*, 23.

(84) Gantefor, G.; Eberhardt, W. *Phys. Rev. Lett.* **1996**, *76*, 4975.

(85) Kitsopoulos, T. N.; Waller, I. M.; Loeser, J. G.; Neumark, D. M. *Chem. Phys. Lett.* **1989**, *159*, 300.

(86) Bartels, C.; Hock, C.; Huwer, J.; Kuhnen, R.; Schwobel, J.; von Issendorff, B. *Science* **2009**, *323*, 1323.

(87) *Photoelectron Spectroscopy*; Ed. by Eland, J. H. D (Butterworths: London), 1984.

(88) *Atomic and Molecular Beam Methods*; Scoles, G., Ed.; (Oxford: OUP), 1988; Vol. 1 & 2.

(89) Akola, J.; Manninen, M.; Häkkinen, H.; Landman, U.; Li, X.; Wang, L.-S. *Phys. Rev. B* **1999**, *60*, R11297.

(90) Wiley, W. C.; McLaren, I. H. *Rev. Sci. Instrum.* **1955**, *26*, 1150.

(91) Heer, W. A. d.; Milani, P. *Rev. Sci. Instrum.* **1991**, *62*, 670.

(92) Bergmann, T.; Martin, T. P.; Schaber, H. *Rev. Sci. Instrum.* **1989**, *60*, 792.

(93) Kruit, P.; Read, F. H. *J. Phys. E: Sci. Instrum.* **1983**, *16*, 313.

(94) *Atomic Energy Levels*; Moore, C. E., Ed.; (US GPO: Washington D. C.), 1971; Vol. II.

(95) *Gold: Progress in Chemistry, Biochemistry and Technology*; Schmidbaur, H., Ed.; Wiley: Chichester, 1999.

(96) *Chem. Soc. Rev.* **2008**, *37,* Issue 9.

(97) *Catalysis by Gold*; Bond, G. C.; Louis, C.; Thompson, D. T., Eds.; Imperial College Press: London, 2007.

(98) Ho, J.; Ervin, K. M.; Lineberger, W. C. *J. Chem. Phys.* **1990**, *93*, 6987.

(99) Bishea, G. A.; Morse, M. D. *J. Chem. Phys.* **1991**, *95*, 8779.

(100) Gantefor, G. F.; Cox, D. M.; Kaldor, A. *J. Chem. Phys.* **1992**, *96*, 4102.

(101) Taylor, K. J.; Pettiettehall, C. L.; Cheshnovsky, O.; Smalley, R. E. *J. Chem. Phys.* **1992**, *96*, 3319.

(102) Collings, B. A.; Athanassenas, K.; Lacombe, D.; Rayner, D. M.; Hackett, P. A. *J. Chem. Phys.* **1994**, *101*, 3506.

(103) Häkkinen, H.; Moseler, M.; Kostko, O.; Morgner, N.; Hoffmann, M. A.; v. Issendorff, B. *Phys. Rev. Lett.* **2004**, *93*, 093401.

(104) Ji, M.; Gu, X.; Li, X.; Gong, X. G.; Li, J.; Wang, L. S. *Angew. Chem. Int. Ed.* **2005**, *44*, 7119.

(105) Bulusu, S.; Li, X.; Wang, L. S.; Zeng, X. C. *Proc. Natl. Acad. Sci. U. S. A* **2006**, *103*, 8326.

(106) Xing, X.; Yoon, B.; Landman, U.; Parks, J. H. *Phys. Rev. B* **2006**, *74*, 165423.

(107) Gu, X.; Bulusu, S.; Li, X.; Zeng, X. C.; Li, J.; Gong, X. G.; Wang, L. S. *Journal of Physical Chemistry C* **2007**, *111*, 8228.

(108) Lechtken, A.; Schooss, D.; Stairs, J. R.; Blom, M. N.; Furche, F.; Morgner, N.; Kostko, O.; von Issendorff, B.; Kappes, M. M. *Angew. Chem. Int. Ed.* **2007**, *46*, 2944.

(109) Pyykko, P. *Chem. Rev.* **1988**, *88*, 563.

(110) Garzón, I. L.; Michaelian, K.; Beltrán, M. R.; Posada-Amarillas, A.; Ordejón, P.; Artacho, E.; Sánchez-Portal, D.; Soler, J. M. *Phys. Rev. Lett.* **1998**, *81*, 1600.

(111) Häkkinen, H.; Landman, U. *Phys. Rev. B* **2000**, *62*, R2287.

(112) Wesendrup, R.; Hunt, T.; Schwerdtfeger, P. *J. Chem. Phys.* **2000**, *112*, 9356.

(113) Wang, J.; Wang, G.; Zhao, J. *Phys. Rev. B* **2002**, *66*, 035418.

(114) Johansson, M. P.; Sundholm, D.; Vaara, J. *Angew. Chem. Int. Ed.* **2004**, *43*, 2678.

(115) Olson, R. M.; Varganov, S.; Gordon, M. S.; Metiu, H.; Chretien, S.; Piecuch, P.; Kowalski, K.; Kucharski, S. A.; Musial, M. *J. Am. Chem. Soc.* **2005**, *127*, 1049.

(116) Walker, A. V. *J. Chem. Phys.* **2005**, *122,* 094310.

(117) Bulusu, S.; Zeng, X. C. *J. Chem. Phys.* **2006**, *125,* 154303.

(118) Koskinen, P.; Hakkinen, H.; Huber, B.; von Issendorff, B.; Moseler, M. *Phys. Rev. Lett.* **2007**, *98,* 015701.

(119) Olson, R. M.; Gordon, M. S. *J. Chem. Phys.* **2007**, *126,* 214310.

(120) Johansson, M. P.; Lechtken, A.; Schooss, D.; Kappes, M. M.; Furche, F. *Phys. Rev. A* **2008**, *77*, 053202.

(121) Huang, W.; Wang, L. S. *Phys. Rev. Lett.* **2009**, *102,* 153401.

(122) Huang, W.; Bulusu, S.; Pal, R.; Zeng, X. C.; Wang, L. S. *Acs Nano* **2009**, *3*, 1225.

(123) Bulusu, S.; Li, X.; Wang, L. S.; Zeng, X. C. *Journal of Physical Chemistry C* **2007**, *111*, 4190.

(124) Yoon, B.; Koskinen, P.; Huber, B.; Kostko, O.; von Issendorff, B.; Hakkinen, H.; Moseler, M.; Landman, U. *Chemphyschem* **2007**, *8*, 157.

(125) Pyykkö, P.; Runeberg, N. *Angew. Chem. Intl. Ed.* **2002**, *41*, 2174.

(126) Li, X.; Kiran, B.; Li, J.; Zhai, H.-J.; Wang, L.-S. *Angew. Chem. Intl. Ed.* **2002**, *41*, 4786.

(127) Kiran, B.; Li, X.; Zhai, H. J.; Cui, L. F.; Wang, L. S. *Angew. Chem. Int. Ed.* **2004**, *43*, 2125.

(128) Neukermans, S.; Janssens, E.; Tanaka, H.; Silverans, R. E.; Lievens, P. *Phys. Rev. Lett.* **2003**, *90,* 033401.

(129) Janssens, E.; Neukermans, S.; Lievens, P. *Cur. Opi. Sol. Sta. Mat. Sci.* **2004**, *8*, 185.

(130) Janssens, E.; Tanaka, H.; Neukermans, S.; Silverans, R. E.; Lievens, P. *Phys. Rev. B* **2004**, *69,* 085402.

(131) Bonacic-Koutecky, V.; Burda, J.; Mitric, R.; Ge, M. F.; Zampella, G.; Fantucci, P. *J. Chem. Phys.* **2002**, *117*, 3120.

(132) Weis, P.; Bierweiler, T.; Gilb, S.; Kappes, M. M. *Chem. Phys. Lett.* **2002**, *355*, 355.

(133) Fernandez, E. M.; Soler, J. M.; Garzon, I. L.; Balbas, L. C. *Phys. Rev. B* **2004**, *70,* 165403.

(134) Bishea, G. A.; Arrington, C. A.; Behm, J. M.; Morse, M. D. *J. Chem. Phys.* **1991**, *95*, 8765.

(135) Weis, P.; Welz, O.; Vollmer, E.; Kappes, M. M. *J. Chem. Phys.* **2004**, *120*, 677.

(136) Negishi, Y.; Nakamura, Y.; Nakajima, A.; Kaya, K. *J. Chem. Phys.* **2001**, *115*, 3657.

(137) Koyasu, K.; Naono, Y.; Akutsu, M.; Mitsui, M.; Nakajima, A. *Chem. Phys. Lett.* **2006**, *422*, 62.

(138) Bauschlicher, C. W.; Langhoff, S. R.; Partridge, H. *J. Chem. Phys.* **1989**, *91*, 2412.

(139) Kello, V.; Sadlej, A. J. *J. Chem. Phys.* **1995**, *103*, 2991.

(140) Zorriasatein, S.; Joshi, K.; Kanhere, D. G. *J. Chem. Phys.* **2008**, *128,* 184314.

(141) Lee, H. M.; Ge, M. F.; Sahu, B. R.; Tarakeshwar, P.; Kim, K. S. *J. Chem. Phys. B* **2003**, *107*, 9994.

(142) Zhao, G. F.; Zeng, Z. *J. Chem. Phys.* **2006**, *125,* 014303.

(143) Lopez, M. J.; Marcos, P. A.; Alonso, J. A. *J. Chem. Phys.* **1996**, *104*, 1056.

(144) Darby, S.; Mortimer-Jones, T. V.; Johnston, R. L.; Roberts, C. *J. Chem. Phys.* **2002**, *116*, 1536.

(145) Rapallo, A.; Rossi, G.; Ferrando, R.; Fortunelli, A.; Curley, B. C.; Lloyd, L. D.; Tarbuck, G. M.; Ohnston, R. L. J. *J. Chem. Phys.* **2005**, *122,* 194308.

(146) Wang, L.-M.; Pal, R.; Huang, W.; Zeng, X. C.; Wang, L.-S., to be submitted.

(147) Huang, W.; Wang, L. S. *Phys. Chem. Chem. Phys.* **2009**, *11*, 2663.

(148) Wales, D. J.; Scheraga, H. A. *Science* **1999**, *285*, 1368.

(149) Delley, B. *J. Chem. Phys.* **1990**, *92*, 508.

(150) Perdew, J. P.; Burke, K.; Ernzerhof, M. *Phys. Rev. Lett.* **1996**, *77*, 3865.

(151) Ross, R. B.; Powers, J. M.; Atashroo, T.; Ermler, W. C.; LaJohn, L. A.; Christiansen, P. A. *J. Chem. Phys.* **1990**, *93*, 6654.

(152) Bylaska, E. J., et al.; Pacific Northwest National Laboratory: Richland, Washington 99352-0999, USA, 2009.

(153) Hakkinen, H. *Chem. Soc. Rev.* **2008**, *37*, 1847.

(154) Janssens, E.; Tanaka, H.; Neukermans, S.; Silverans, R. E.; Lievens, P. *New Journal of Physics* **2003**, *5, 46*.

(155) Ferrighi, L.; Hammer, B.; Madsen, G. K. H. *J. Am. Chem. Soc.* **2009**, *131*, 10605.

(156) Mantina, M.; Valero, R.; Truhlar, D. G. *J. Chem. Phys.* **2009**, *131,* 064706.

(157) Pyykkö, P.; Zhao, Y. *Chem. Phys. Lett.* **1991**, *177*, 103.

(158) Abe, M.; Nakajima, T.; Hirao, K. *J. Chem. Phys.* **2002**, *117*, 7960.

(159) Majumder, C.; Kandalam, A. K.; Jena, P. *Phys. Rev. B* **2006**, *74,* 205437.

(160) Kiran, B.; Li, X.; Zhai, H.-J.; Wang, L.-S. *J. Chem. Phys.* **2006**, *125*, 133204.

(161) Li, X.; Kiran, B.; Wang, L. S. *J. Phys. Chem. A* **2005**, *109*, 4366.

(162) Pal, R.; Bulusu, S.; Zeng, X. C. *J. Comput. Methods Sci. Eng.* **2007**, *7*, 185.

(163) Majumder, C. *Phys. Rev. B* **2007**, *75,* 235409.

(164) Pal, R.; Wang, L. M.; Huang, W.; Wang, L. S.; Zeng, X. C. *J. Am. Chem. Soc.* **2009**, *131*, 3396.

(165) *Gaussian 03, Revision C.02*; Frisch, M. J., et al., Ed.; Gaussian, Inc. : Wallingford, CT, 2004.

(166) *ADF 2008.01, SCM Theoretical Chemistry*; Vrije University: Amsterdam, The Netherlands (http://www.scm.com).

(167) Corbett, J. D. *Angew. Chem. Intl. Ed.* **2000**, *39*, 670.

(168) Bai, J.; Virovets, A. V.; Scheer, M. *Science* **2003**, *300*, 781.

(169) Gu, X.; Ji, M.; Wei, S. H.; Gong, X. G. *Phys. Rev. B* **2004**, *70,* 205401.

(170) Gao, Y.; Zeng, X. C. *J. Am. Chem. Soc.* **2005**, *127*, 3698.

(171) Wang, J. L.; Jellinek, J.; Zhao, J.; Chen, Z. F.; King, R. B.; Schleyer, P. V. *J. Phys. Chem. A* **2005**, *109*, 9265.

(172) Karttunen, A. J.; Linnolahti, M.; Pakkanen, T. A.; Pyykko, P. *Chem. Commun.* **2008**, 465.

(173) Heath, J. R.; O'Brien, S. C.; Zhang, Q.; Liu, Y.; Curl, R. F.; Tittel, F. K.; Smalley, R. E. *J. Am. Chem. Soc.* **2002**, *107*, 7779.

(174) Alvarez, M. M.; Gillan, E. G.; Holczer, K.; Kaner, R. B.; Min, K. S.; Whetten, R. L. *J. Phys. Chem.* **2002**, *95*, 10561.

(175) Yannoni, C. S.; Hoinkis, M.; de Vries, M. S.; Bethune, D. S.; Salem, J. R.; Crowder, M. S.; Johnson, R. D. *Science* **1992**, *256*, 1191.

(176) Curl, R. F.; Smalley, R. E. *Science* **1988**, *242*, 1017.

(177) Zhai, H. J.; Li, J.; Wang, L. S. *J. Chem. Phys.* **2004**, *121*, 8369.

(178) Walter, M.; Hakkinen, H. *Phys. Chem. Chem. Phys.* **2006**, *8*, 5407.

(179) Gao, Y.; Bulusu, S.; Zeng, X. C. *Chemphyschem* **2006**, *7*, 2275.

(180) Guo, T.; Smalley, R. E.; Scuseria, G. E. *J. Chem. Phys.* **1993**, *99*, 352.

(181) Wang, L. M.; Bulusu, S.; Zhai, H. J.; Zeng, X. C.; Wang, L. S. *Angew. Chem. Int. Ed.* **2007**, *46*, 2915.

(182) Schwerdtfeger, P.; Dolg, M. *Phys. Rev. A* **1991**, *43*, 1644.

(183) Schwerdtfeger, P. *Angew. Chem. Intl. Ed.* **2003**, *42*, 1892.

(184) Hakkinen, H.; Abbet, W.; Sanchez, A.; Heiz, U.; Landman, U. *Angew. Chem. Int. Ed.* **2003**, *42*, 1297.

(185) Li, X.; Kiran, B.; Cui, L. F.; Wang, L. S. *Phys. Rev. Lett.* **2005**, *95,* 235401.

(186) Pyykko, P. *Nat Nano* **2007**, *2*, 273.

(187) Sun, Q.; Wang, Q.; Chen, G.; Jena, P. *J. Chem. Phys.* **2007**, *127*, 214706.

(188) Sun, Q.; Wang, Q.; Jena, P.; Kawazoe, Y. *Acs Nano* **2008**, *2*, 341.

(189) Fa, W.; Dong, J. M. *J. Chem. Phys.* **2008**, *128*.

(190) Wang, L.-M.; Pal, R.; Huang, W.; Zeng, X. C.; Wang, L.-S. *J. Chem. Phys.* **2009**, *130*, 051101.

(191) Kim, Y. D.; Fischer, M.; Gantefor, G. *Chem. Phys. Lett.* **2003**, *377*, 170.

(192) Salisbury, B. E.; Wallace, W. T.; Whetten, R. L. *Chem. Phys.* **2000**, *262*, 131.

(193) Wang, L. M.; Bulusu, S.; Huang, W.; Pal, R.; Wang, L. S.; Zeng, X. C. *J. Am. Chem. Soc.* **2007**, *129*, 15136.

(194) Riegel, D.; Büermann, L.; Gross, K. D.; Luszik-Bhadra, M.; Mishra, S. N. *Phys. Rev. Lett.* **1989**, *62*, 316.

(195) Kowallik, R.; Bertschat, H. H.; Biedermann, K.; Haas, H.; Müller, W.; Spellmeyer, B.; Zeitz, W. D. *Phys. Rev. Lett.* **1989**, *63*, 434.

(196) Anderson, P. W. *Phys. Rev.* **1961**, *124*, 41.

(197) Blaha, P.; Callaway, J. *Phys. Rev. B* **1986**, *33*, 1706.

(198) Vvedensky, D. D.; Eberhart, M. E.; McHenry, M. E. *Phys. Rev. B* **1987**, *35*, 2061.

(199) Guenzburger, D.; Ellis, D. E. *Phys. Rev. Lett.* **1991**, *67*, 3832.

(200) Billas, I. M. L.; Chatelain, A.; de Heer, W. A. *Science* **1994**, *265*, 1682.

(201) Apsel, S. E.; Emmert, J. W.; Deng, J.; Bloomfield, L. A. *Phys. Rev. Lett.* **1996**, *76*, 1441.

(202) Pastor, G. M.; Hirsch, R.; Mühlschlegel, B. *Phys. Rev. Lett.* **1994**, *72*, 3879.

(203) Knickelbein, M. B. *Phys. Rev. Lett.* **2001**, *86*, 5255.

(204) Moseler, M.; Häkkinen, H.; Landman, U. *Phys. Rev. Lett.* **2002**, *89*, 176103.

(205) Liu, F.; Khanna, S. N.; Jena, P. *Phys. Rev. B* **1991**, *43*, 8179.

(206) Janssens, E.; Neukermans, S.; Nguyen, H. M. T.; Nguyen, M. T.; Lievens, P. *Phys. Rev. Lett.* **2005**, *94,* 113401.

(207) Sun, Q.; Gong, X. G.; Zheng, Q. Q.; Sun, D. Y.; Wang, G. H. *Phys. Rev. B* **1996**, *54*, 10896.

(208) Pramann, A.; Nakajima, A.; Kaya, K. *J. Chem. Phys.* **2001**, *115*, 5404.

(209) Khanna, S. N.; Rao, B. K.; Jena, P. *Phys. Rev. Lett.* **2002**, *89*, 016803.

(210) Zheng, W.; Nilles, J. M.; Radisic, D.; Kit H. Bowen, J. *J. Chem. Phys.* **2005**, *122*, 071101.

(211) Schooss, D.; Blom, M. N.; Parks, J. H.; von Issendorff, B.; Haberland, H.; Kappes, M. M. *Nano Letters* **2005**, *5*, 1972.

(212) Wang, L. M.; Bai, J.; Lechtken, A.; Huang, W.; Schooss, D.; Kappes, M. M.; Zeng, X. C.; Wang, L. S. *Phys. Rev. B* **2009**, *79*.

(213) van't Hoff, J. H. *Arch. Neerl. Sci. Exactes, Nat.* **1874**, 445.

(214) LeBel, J. A. *Bull. Soc. Chim. Fr.* **1874**, *22*, 337.

(215) Hoffmann, R.; Alder, R. W.; Wilcox, C. F. *J. Am. Chem. Soc.* **1970**, *92*, 4992.

(216) Hoffmann, R. *Pure. Appl. Chem.* **1971**, *28*, 181.

(217) Collins, J. B.; Dill, J. D.; Jemmis, E. D.; Apeloig, Y.; Schleyer, P. V.; Seeger, R.; Pople, J. A. *J. Am. Chem. Soc.* **1976**, *98*, 5419.

(218) Krogh-Jespersen, K.; Cremer, D.; Poppinger, D.; Pople, J. A.; Schleyer, P. v. R.; Chandrasekhar, J. *J. Am. Chem. Soc.* **2002**, *101*, 4843.

(219) Chandrasekhar, J.; Wurthwein, E. U.; Schleyer, P. V. *Tetrahedron* **1981**, *37*, 921.

(220) Schleyer, P. V.; Boldyrev, A. I. *J. Chem. Soc. Chem. Commun.* **1991**, 1536.

(221) Boldyrev, A. I.; Simons, J. *J. Am. Chem. Soc.* **1998**, *120*, 7967.

(222) Laidig, W. D.; Schaefer, H. F. *J. Am. Chem. Soc.* **2002**, *100*, 5972.

(223) Bohm, M. C.; Gleiter, R.; Schang, P. *Tetrahedron Letters* **1979**, 2575.

(224) Erker, G.; Albrecht, M.; Kruger, C.; Werner, S. *J. Am. Chem. Soc.* **1992**, *114*, 8531.

(225) Erker, G.; Albrecht, M.; Kruger, C.; Werner, S.; Binger, P.; Langhauser, F. *Organometallics* **1992**, *11*, 3517.

(226) Erker, G.; Albrecht, M.; Werner, S.; Nolte, M.; Kruger, C. *Chemische Berichte-Recueil* **1992**, *125*, 1953.

(227) Erker, G.; Petrenz, R.; Kruger, C.; Lutz, F.; Weiss, A.; Werner, S. *Organometallics* **1992**, *11*, 1646.

(228) Gleiter, R.; Hylakryspin, I.; Niu, S. Q.; Erker, G. *Angew. Chem. Int. Ed.* **1993**, *32*, 754.

(229) Poumbga, C. N.; Benard, M.; Hylakryspin, I. *J. Am. Chem. Soc.* **1994**, *116*, 8259.

(230) Rottger, D.; Erker, G.; Frohlich, R.; Grehl, M.; Silverio, S. J.; Hylakryspin, I.; Gleiter, R. *J. Am. Chem. Soc.* **1995**, *117*, 10503.

(231) Glukhovtsev, M. N.; Pross, A.; Radom, L. *J. Am. Chem. Soc.* **2002**, *116*, 5961.

(232) Wiberg, K. B.; Odonnell, M. J. *J. Am. Chem. Soc.* **1979**, *101*, 6660.

(233) Würthwein, E.-U.; Chandrasekhar, J.; Jenmis, E. D.; von Ragué Schleyer, P. *Tetrahedron Letters* **1981**, *22*, 843.

(234) Schori, H.; Patil, B. B.; Keese, R. *Tetrahedron* **1981**, *37*, 4457.

(235) Dodziuk, H. *J. Mol. Struct.* **1990**, *239*, 167.

(236) McGrath, M. P.; Radom, L. *J. Am. Chem. Soc.* **1993**, *115*, 3320.

(237) Keese, R. *Chem. Rev.* **2006**, *106*, 4787.

(238) Merino, G.; Mendez-Rojas, M. A.; Vela, A.; Heine, T. *J.Comput. Chem.* **2007**, *28*, 362.

(239) Sateesh, B.; Reddy, A. S.; Sastry, G. N. *J.Comput. Chem.* **2007**, *28*, 335.

(240) Li, X.; Zhang, H. F.; Wang, L. S.; Geske, G. D.; Boldyrev, A. I. *Angew. Chem. Int. Ed.* **2000**, *39*, 3630.

(241) Li, X.; Zhai, H. J.; Wang, L. S. *Chem. Phys. Lett.* **2002**, *357*, 415.

(242) Geske, G. D.; Boldyrev, A. I. *Inorg. Chem.* **2002**, *41*, 2795.

(243) Li, S. D.; Ren, G. M.; Miao, C. Q.; Jin, Z. H. *Angew. Chem. Int. Ed.* **2004**, *43*, 1371.

(244) Yang, L. M.; Ding, Y. H.; Sun, C. C. *J. Am. Chem. Soc.* **2007**, *129*, 658.

(245) Starodub, V. A.; Ziolkovskii, D. V. *J. Struct. Chem.* **2006**, *47*, 8.

(246) Yang, L. M.; Ding, Y. H.; Sun, C. C. *J. Am. Chem. Soc.* **2007**, *129*, 1900.

(247) Merino, G.; Mendez-Rojas, M. A.; Beltraan, H. I.; Corminboeuf, C.; Heine, T.; Vela, A. *J. Am. Chem. Soc.* **2004**, *126*, 16160.

(248) Perez, N.; Heine, T.; Barthel, R.; Seifert, G.; Vela, A.; Mendez-Rojas, M. A.; Merino, G. *Org. Lett.* **2005**, *7*, 1509.

(249) Su, M. D. *Inorg. Chem.* **2005**, *44*, 4829.

(250) Exner, K.; Schleyer, P. V. *Science* **2000**, *290*, 1937.

(251) Wang, Z.-X.; Schleyer, P. v. R. *Science* **2001**, *292*, 2465.

(252) Erhardt, S.; Frenking, G.; Chen, Z.; Schleyer, P. v. R. *Angew. Chem. Intl. Ed.* **2005**, *44*, 1078.

(253) Ito, K.; Chen, Z.; Corminboeuf, C.; Wannere, C. S.; Zhang, X. H.; Li, Q. S.; Schleyer, P. v. R. *J. Am. Chem. Soc.* **2007**, *129*, 1510.

(254) Minyaev, R. M.; Gribanova, T. N.; Starikov, A. G.; Minkin, V. I. *Mendeleev Communications* **2001**, 213.

(255) Minyaev, R. M.; Gribanova, T. N.; Starikov, A. G.; Minkin, V. I. *Doklady Chemistry* **2002**, *382*, 41.

(256) Minkin, V. I.; Minyaev, R. M. *Mendeleev Communications* **2004**, 43.

(257) Havenith, R. W. A.; Fowler, P. W.; Steiner, E. *Chem. Eur. J.* **2002**, *8*, 1068.

(258) Li, S. D.; Miao, C. Q.; Guo, J. C.; Ren, G. M. *J. Am. Chem. Soc.* **2004**, *126*, 16227.

(259) Li, S. D.; Miao, C. Q.; Ren, G. M. *Eur. J. Inorg. Chem.* **2004**, 2232.

(260) Li, S. D.; Guo, J. C.; Miao, C. Q.; Ren, G. M. *J. Phys. Chem. A* **2005**, *109*, 4133.

(261) Li, S. D.; Miao, C. Q. *J. Phys. Chem. A* **2005**, *109*, 7594.

(262) Li, S. D.; Miao, C. Q.; Ren, G. M.; Guo, J. C. *Eur. J. Inorg. Chem.* **2006**, 2567.

(263) Islas, R.; Heine, T.; Ito, K.; Schleyer, P. V. R.; Merino, G. *J. Am. Chem. Soc.* **2007**, *129*, 14767.

(264) Kemsley, J. *Chem. Eng. News* **2007**, *85*, 17.

(265) Li, S. D.; Miao, C. Q.; Guo, J. C. *J. Phys. Chem. A* **2007**, *111*, 12069.

(266) Zhai, H.-J.; Alexandrova, A. N.; Birch, K. A.; Boldyrev, A. I.; Wang, L.-S. *Angew. Chem. Intl. Ed.* **2003**, *42*, 6004.

(267) Alexandrova, A. N.; Zhai, H.-J.; Wang, L.-S.; Boldyrev, A. I. *Inorg. Chem.* **2004**, *43*, 3552.

(268) Wang, L. M.; Huang, W.; Averkiev, B. B.; Boldyrev, A. I.; Wang, L. S. *Angew. Chem. Int. Ed.* **2007**, *46*, 4550.

(269) Wang, L.-M.; Huang, W.; Wang, L.-S.; Averkiev, B. B.; Boldyrev, A. I. *J. Chem. Phys.* **2009**, *130*, 134303.

(270) Zhai, H. J.; Kiran, B.; Li, J.; Wang, L. S. *Nat. Mater.* **2003**, *2*, 827.

(271) Zhai, H.-J.; Wang, L.-S.; Alexandrova, A. N.; Boldyrev, A. I.; Zakrzewski, V. G. *J. Phys. Chem. A* **2003**, *107*, 9319.

(272) Zhai, H.-J.; Wang, L.-S.; Alexandrova, A. N.; Boldyrev, A. I. *J. Chem. Phys.* **2002**, *117*, 7917.

(273) Alexandrova, A. N.; Boldyrev, A. I.; Zhai, H.-J.; Wang, L.-S.; Steiner, E.; Fowler, P. W. *J. Phys. Chem. A* **2003**, *107*, 1359.

(274) Alexandrova, A. N.; Boldyrev, A. I.; Zhai, H.-J.; Wang, L.-S. *J. Phys. Chem. A* **2004**, *108*, 3509.

(275) Alexandrova, A. N.; Boldyrev, A. I.; Zhai, H.-J.; Wang, L.-S. *J. Chem. Phys.* **2005**, *122*, 054313.

(276) Alexandrova, A. N.; Boldyrev, A. I.; Fu, Y.-J.; Yang, X.; Wang, X.-B.; Wang, L.-S. *J. Chem. Phys.* **2004**, *121*, 5709.

(277) Alexandrova, A. N.; Boldyrev, A. I. *J. Chem. Theory Comput.* **2005**, *1*, 566.

(278) Frisch, M. J., et al.; Gaussian, Inc.: Wallingford CT, 2004.

(279) Schaftenaar, G.; CAOS/CAMM: The Netherlands, 1998.

(280) Hawthorne, M. F.; Zink, J. I.; Skelton, J. M.; Bayer, M. J.; Liu, C.; Livshits, E.; Baer, R.; Neuhauser, D. *Science* **2004**, *303*, 1849.

(281) Wang, X.-B.; Ding, C.-F.; Wang, L.-S. *Phys. Rev. Lett.* **1998**, *81*, 3351.

(282) Compton, R. N.; Tuinman, A. A.; Klots, C. E.; Pederson, M. R.; Patton, D. C. *Phys. Rev. Lett.* **1997**, *78*, 4367.

(283) Boltalina, O. V.; Hvelplund, P.; Larsen, M. C.; Larsson, M. O. *Phys. Rev. Lett.* **1998**, *80*, 5101.

(284) Averkiev, B. B.; Zubarev, D. Y.; Wang, L. M.; Huang, W.; Wang, L. S.; Boldyrev, A. I. *J. Am. Chem. Soc.* **2008**, *130*, 9248.

(285) Zubarev, D. Y.; Boldyrev, A. I. *Phys. Chem. Chem. Phys.* **2008**, *10*, 5207.

(286) Averkiev, B. B.; Wang, L. M.; Huang, W.; Wang, L. S.; Boldyrev, A. I. *Phys. Chem. Chem. Phys.* **2009**, *11*, 9840.

(287) Pei, Y.; Zeng, X. C. *J. Am. Chem. Soc.* **2008**, *130*, 2580.

(288) Averkiev, B. B.; Boldyrev, A. I. *Russian Journal of General Chemistry* **2008**, *78*, 769.

(289) Ito, K.; Pu, Z.; Li, Q.-S.; Schleyer, P. v. R. *Inorg. Chem.* **2008**, *47*, 10906.